



Chem Soc Rev

Thin Film Photoelectrodes for Solar Water Splitting

Journal:	<i>Chemical Society Reviews</i>
Manuscript ID	CS-REV-11-2018-000868.R1
Article Type:	Review Article
Date Submitted by the Author:	18-Dec-2018
Complete List of Authors:	He, Yumin; Boston College, Chemistry department Hamann, Thomas; Michigan State University, Chemistry Wang, Dunwei; Boston College, Chemistry

SCHOLARONE™
Manuscripts



Journal Name

ARTICLE

Thin Film Photoelectrodes for Solar Water Splitting

Yumin He,^a Thomas Hamann ^{*b} and Dunwei Wang ^{*a}Received 00th January 20xx,
Accepted 00th January 20xx

DOI: 10.1039/x0xx00000x

www.rsc.org/

Photoelectrochemical (PEC) water splitting has been intensively studied in the past decades as a promising method for large-scale solar energy storage. Among the various issues that limit the progress of this field, the lack of photoelectrode materials with suitable properties in all aspects of light absorption, charge separation and transport, and charge transfer is a key challenge, which has attracted tremendous research attention. A large variety of compositions, in different forms, have been tested. This review aims to summarize efforts in this area, with a focus on materials-related considerations. Issues discussed by this review include synthesis, optoelectronic properties, charge behaviors and catalysis. In the recognition that thin-film materials are representative model systems for the study of these issues, we elected to focus on this form, so as to provide a concise and coherent account on the different strategies that have been proposed and tested. Because practical implementation is of paramount importance to the eventual realization of using solar fuel for solar energy storage, we pay particular attention to strategies proposed to address the stability and catalytic issues, which are two key factors limiting the implementation of efficient photoelectrode materials. To keep the overall discussion focused, all discussions were presented within the context of water splitting reactions. How the thin-film systems may be applied for fundamental studies of the water splitting chemical mechanisms is discussed, as well as on how to use the model system to test device engineering design strategies.

1 Definition of thin-film photoelectrodes and scope of this Review

As has been extensively reviewed by other authors elsewhere and in this *Special Issue*, the dilemma between efficiencies and costs is a critical challenge that has prevented solar fuels from being developed into a practical technology for large-scale solar energy harvesting and storage. That is, highly efficient or low-cost solar fuel synthesis has been demonstrated separately but not together. At the heart of the dilemma are issues connected to materials which can be used to harvest solar energy and carry out the desired chemical reactions. Such an understanding has underpinned the significant research efforts in materials innovations for solar fuel synthesis. Indeed, a wide spectrum of materials in terms of compositions, morphologies and structures, among other factors, has been proposed and tested, with varying degrees of successes in solving the cost-efficiency dilemma. In this *Review*, we focus on thin-film materials. More specifically, we concentrate on materials whose thicknesses are below a few microns, mostly in the tens of nanometres range. Materials of such characteristic dimensions are unique for a number of reasons. First, they represent a form factor that can be readily studied for materials' fundamental properties, especially charge behaviours such as excitation, separation, transport and transfer. For instance, most thin films can be

readily fashioned into an electrode for the assessment of the electrochemical and photoelectrochemical behaviours, which report on the charge properties of the materials. While better performance may be measured on other morphologies (*vide infra*), particularly those with nanometre scale features, thin films are often much simpler to study for insights that can guide future efforts aimed at optimizing structures for further improvements. In other words, thin film materials represent a good model platform for fundamental understanding of solar fuel materials.

Second, a rich knowledge base on thin film materials has been generated by decades of intense research on semiconductors. A great deal has been learned about how to synthesize them; a battery of experimental techniques has been developed to readily study them; strategies on how to combine different layers of components with complementary functionalities into a single material have been proposed and proven highly effective. The last point is especially valuable for the purpose of solar fuel synthesis because it is widely recognized that a single composition is unlikely to meet all the needs, including light absorption, charge separation, catalysis and passivation. The best hope to realize these functionalities is to construct an integrated system that includes multiple components, each optimized for one or more specific purposes. For example, semiconductors with suitable bandgaps and electronic properties may be used to maximize light absorption and charge separation; heterogeneous and/or molecular catalysts can be introduced on top of the semiconducting light absorber for fast and highly specific charge transfer; additional protection may be necessary for durability. While such a strategy may be

^a Department of Chemistry, Merkert Chemistry Center, Boston College, 2609 Beacon St., Chestnut Hill, Massachusetts 02467, United States.

^b Department of Chemistry, Michigan State University, East Lansing, Michigan 48824, United States.

implemented in a variety of forms, thin films have proven the most straightforward thanks to the rich knowledge base on their syntheses. More important, what is learned on thin film materials may be readily transferred for the construction of more complex structures for optimum performance such as various nanostructures.

Our main goal of writing this *Review* is to summarize and examine existing strategies developed for materials innovations to meet the challenge of efficient *and* inexpensive solar fuel synthesis. To best serve this purpose, we limit our discussions to semiconductors as the unit for light absorption and charge separation. It is noted that other mechanisms have also been exploited for this purpose, including plasmonic effect and anisotropic charge behaviours in two-dimensional (2D) materials. Interested readers are directed to reviews on these materials such as those cited here.¹⁻³ We note that many of the considerations presented here to further develop these semiconductor materials are shared by materials governed by

the article, we present various implementations of thin film materials for solar fuel synthesis.

2 Thin film synthesis

A variety of synthetic methods have been developed to produce thin films. Generally, they may be categorized into three major groups based on the nature of the reactions utilized, namely physical vapor deposition, chemical deposition and electrochemical deposition (Figure 1). The principles of each method are presented below with selected examples. It is noted that in a complex thin film, which may include multiple layers, each layer may be prepared by a different method. Such a consideration is particularly relevant for the topic discussed here as successful solar fuel reactions often dictate the combination of materials with distinctly different, yet complementary, properties (Fig. 1). The flexibility of using different methods to synthesize different components holds

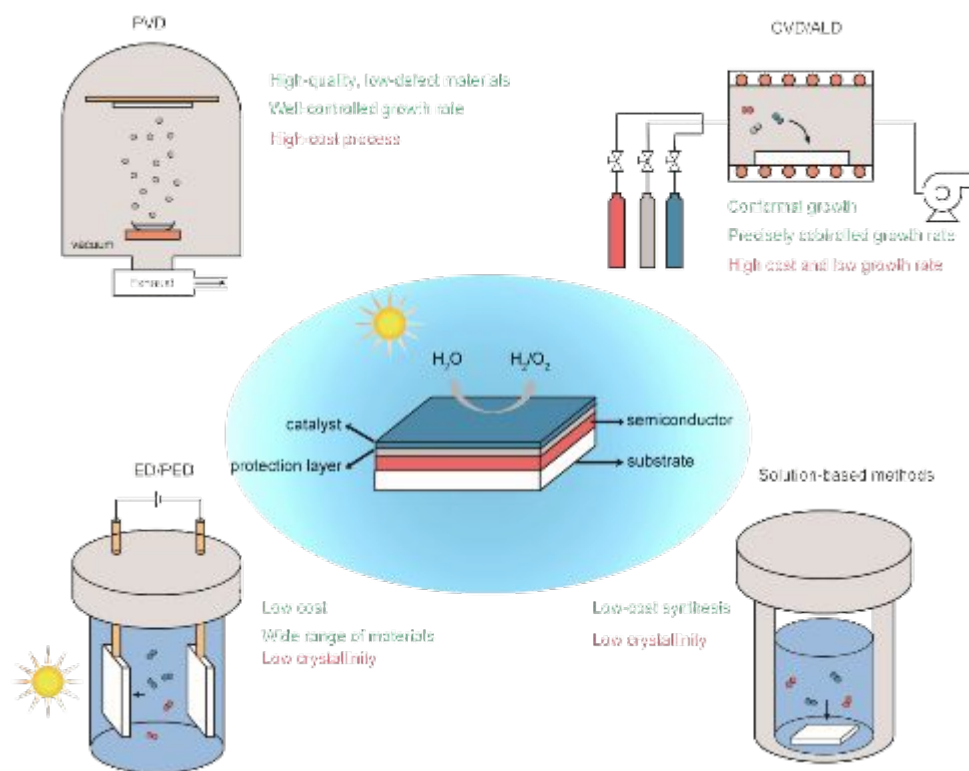


Figure 1 Schematics showing the common deposition methods for thin-film materials. The advantages and disadvantages of each method are shown in green and red texts, respectively.

other mechanisms. Similarly, although we indeed include discussions on protection, readers interested in comprehensive reviews on that topic are directed elsewhere, e.g., by Hu *et al.*⁴ and Bae *et al.*⁵. Instead, this article places an emphasis on materials-related issues in connection to the processes of charge excitation, transport and transfer. The writing is organized as follows. We start by a general introduction of the synthetic methods of thin films and move on to discussions of thin films based on their composition within the context of solar fuel synthesis. Corrosion protection strategies are next discussed, followed by thin film catalyst layers. At the end of

great promise for realizing the desired functionalities.

2.1 Physical vapor deposition (PVD)

Physical vapor deposition refers to synthesis methods which vaporize target materials with physical means for subsequent deposition on the receiving substrates. A key distinguishing feature of PVD is the lack of chemical reactions. The methods to introduce target materials include plasma (sputtering, molecular beam epitaxy), electron beam (e-beam evaporation, molecular beam epitaxy), heat (thermal evaporation, molecular beam epitaxy) and laser (pulse laser deposition). In comparison with other thin film growth techniques, PVD features

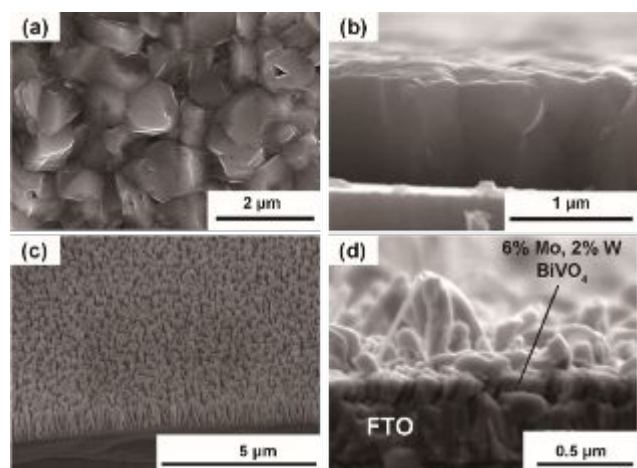


Figure 2 SEM images for representative materials synthesized by PVD methods. (a) Front view and (b) side view of $\text{Cu}(\text{Ga}, \text{In})\text{Se}_2$ films grown on Mo-coated glass substrates by MBE. (c) InGaN/GaN nanowires grown on Si substrates by MBE. (d) Mo, W-doped BiVO_4 thin films grown on FTO-coated glass substrates by e-beam evaporation. (a) and (b) reproduced from ref. 7 with permission from the Royal Society of Chemistry. (c) reprinted with permission from ref. 9. Copyright 2015 American Chemical Society. (d) reproduced from Ref. 42 with permission from the PCCP Owner Societies.

advantages such as versatile, reproducible and relatively easy to implement. The resulting materials are often of the highest quality in terms of purity and quality. For these reasons, PVD has been widely used to synthesize nearly every type of semiconductors reported to date. Just within the context of solar fuel synthesis, a large number of examples exist, where high performance photoelectrodes were prepared by PVD. For instance, $\text{Cu}(\text{InGa})\text{Se}_2$ photocathode was obtained by the co-evaporation of In, Ga, Cu and Se targets onto Mo-coated glass substrates.⁶ Materials with similar compositions have also been achieved by molecular beam epitaxy (MBE), with the substrate temperature first increased to 300 °C and then fixed at 550 °C (Figure 2a and 2b).⁷ Ta_3N_5 has been reported to be synthesized by sputtering TaO_x thin-films onto Ta metal substrates, followed by a facile nitridation process.⁸ InGaN nanowires have been reported to grow on Si substrates using In/Ga metal and N_2 plasma at 600 °C using MBE (Figure 2c).⁹ In addition to photoactive materials as noted above, PVD has been used for the deposition of protective layers and/or catalysts. For example, TiO_2 protection layer can be deposited on Si surface by sputtering Ti target in a reactive oxygen atmosphere.¹⁰ To minimize surface oxidation of Si during the process, a thin layer of Ti (5 nm) was first sputtered to protect the surface. Metal layers ($\text{AuGe}/\text{Ni}/\text{Au}$ and Pt) was e-beam evaporated on the surface of GaAs photocathode to protect it from

photocorrosion.¹¹ Of these examples, the most broadly implemented may be Pt deposition via sputtering as an effective catalyst to improve the hydrogen evolution reaction (HER) performance of photocathodes.¹² The limitation of PVD is mainly the high cost due to high-vacuum chamber assemblies, which introduce extra fabrication cost compared with solution-based methods.

2.2 Chemical deposition

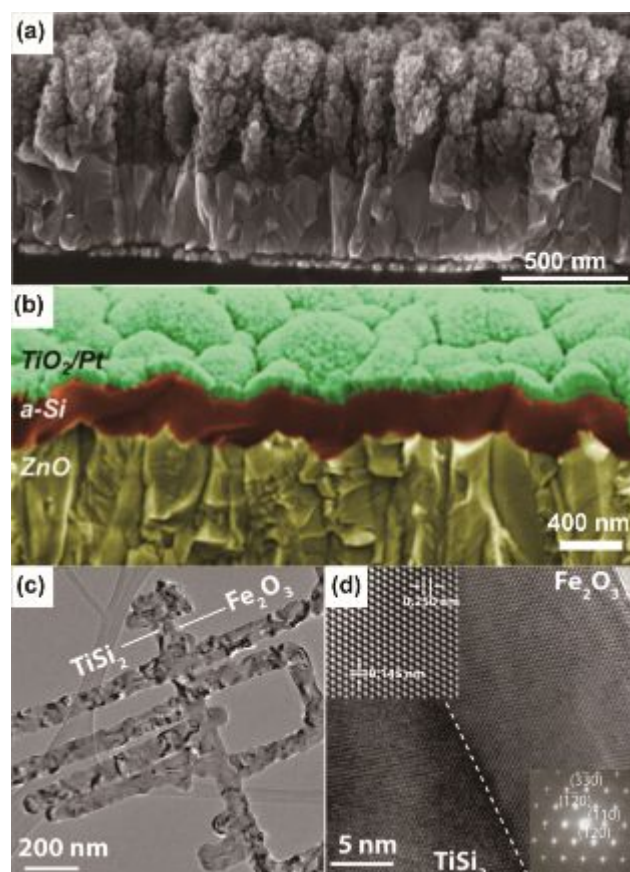


Figure 3 SEM and TEM images for representative materials synthesized by chemical depositions. (a) side view SEM image of cauliflower-like hematite on the FTO glass. (b) side view SEM image of a-Si. (c) and (d) TEM images of hematite thin film on TiSi_2 nanonets. (a) reprinted with permission from ref. 13. Copyright 2006 American Chemical Society. (b) reprinted with permission from ref. 16. Copyright 2013 American Chemical Society. (c) and (d) reprinted with permission from ref. 17. Copyright 2011 American Chemical Society.

The most obvious difference between chemical deposition and PVD is the involvement of chemical precursors and/or chemical reactions during the deposition. Depending on the media within which the deposition is carried out, chemical deposition may be divided into subcategories. When the deposition is mainly performed via vapor-phase processes, we have chemical vapor deposition (CVD) or atomic layer deposition (ALD). For the ease of precursor delivery, volatile materials such as organometallic compounds are most often used as the precursors. The key difference between CVD and ALD lies in that the latter typically features self-limiting surface chemical reactions. CVD has been widely employed to synthesize thin film semiconductors, including metal oxides. For example, Kay

et al. reported the synthesis of cauliflower-type hematite (α - Fe_2O_3) thin films from $\text{Fe}(\text{CO})_5$ and tetraethoxysilane (TEOS) on a FTO-coated glass substrate at 415°C (Figure 3a).¹³ GaAs-based photoelectrodes have been synthesized by the metal-organic CVD (MOCVD) method at 800°C , using trimethyl gallium, trimethyl aluminium and arsine (AsH_3) as the precursors for Ga, Al and As, respectively.^{11, 14, 15} Amorphous silicon (a-Si) was deposited via a plasma-enhanced CVD (PECVD) method, in which silane (SiH_4) was used as the precursor for silicon, and phosphine (PH_3) and trimethyl boron ($\text{B}(\text{CH}_3)_3$) were used for n- and p-type doping, respectively (Figure 3b).¹⁶ Different from CVD, the self-limiting surface reaction nature of ALD gives rise to the ability to precisely control the growth thickness by a layer-by-layer deposition process. Consequently, it has been widely used to deposit thin-film semiconductors, protective layers and catalysts. For example, thin-film hematite has been deposited on high-aspect ratio substrates such as TiSi_2 nanonets and Si nanowires with $\text{Fe}(\text{O}^i\text{Bu})_6$ and H_2O as the Fe and O precursors, respectively (Figure 3c).^{17, 18} ALD-grown TiO_2 has been explored as an effective protection layer on both photoanode and photocathode materials. It was found that the crystallinity of TiO_2 is sensitive to many factors, including the type of precursors used. When titanium isopropoxide ($\text{Ti}(\text{i-PrO})_4$) was used as the precursor, crystalline TiO_2 was deposited at 275°C onto Cu_2O , which served as a protection layer.¹⁹ When tetrakis(dimethylamido)-titanium (TDMAT) was used as the precursor, amorphous TiO_2 was deposited at 150°C onto BiVO_4 that also served as a protection layer.²⁰ ALD was also be used to deposit thin films of catalysts. For example, NiO has been deposited on the surface of BiVO_4 at 260°C using bis(2,2,6,6-tetramethylheptane-3,5-dionato)nickel(II) ($\text{Ni}(\text{thd})_2$) and H_2O as the precursors.²¹ Interestingly, the as-grown NiO is also a p-type semiconductor. In addition to serving as an oxygen evolution reaction (OER) catalyst, it was discovered to further improve the performance of the system by forming a p-n junction with BiVO_4 .

An advantage offered by CVD and ALD is the control over the purity of the target materials, thanks to the gas-phase nature of the precursor delivery. The low pressures at which the deposition is carried out also ensure reasonably long mean free path of the precursor species in the reactor, suggesting that most film growth is not diffusion limited. This feature, however, makes the implementation relatively difficult, increasing the processing cost. Such a challenge may be addressed by relaxing the requirements for vacuum and carrying out the deposition either directly in a solution or in ambient air. The most popularly encountered examples include chemical bath deposition (CBD) and electrochemical deposition. Due to the broad implementations of electrochemical deposition, we will introduce this method as a subcategory next. In this subsection, our attention is focused on CBD and a number of other thin film deposition techniques that involve solutions, including spin-coating and spray pyrolysis.

Various metal oxides, such as hematite, WO_3 and BiVO_4 , have been successfully synthesized by solution methods. For instance, nanostructured hematite thin films were synthesized by immersing a FTO glass into the mixture of FeCl_3 and NaNO_3

at 100°C , followed by post-annealing in air (Figure 4a).²² WO_3 thin films were prepared by first mixing the tungsten precursor

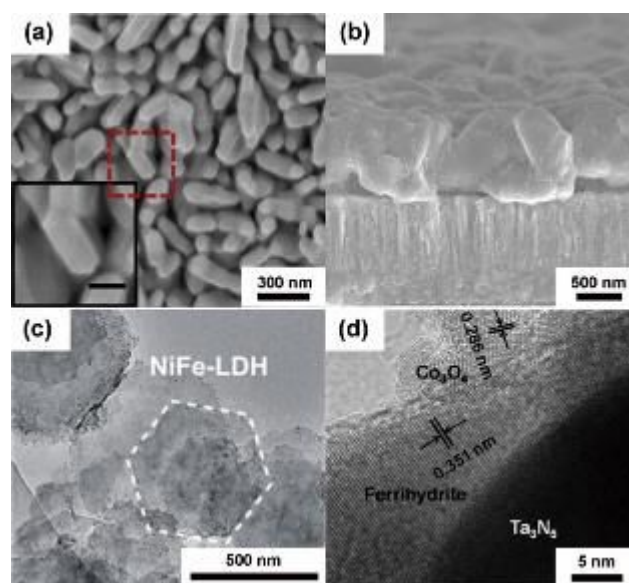


Figure 4 (a) SEM image showing the morphology of hematite grown by CBD. The scale bar of the insert is 100 nm. (b) Cross-sectional SEM image of $\text{Cu}_2\text{ZnSnS}_4$ films grown on Mo-coated glass substrate by spin coating. (c) TEM image showing NiFe-LDH nanoplatelets synthesized by hydrothermal methods. (d) TEM image showing Ta_3N_5 photoanode coated by thin films of ferrihydrite and Co_3O_4 nanoparticles synthesized via hydrothermal methods. (a) reproduced from ref. 22 with permission from Springer Nature. (b) reprinted with permission from ref. 24. Copyright 2016 American Chemical Society. (c) reprinted with permission from ref. 26. Copyright 2015 American Chemical Society. (d) reproduced from ref. 25 with permission from John Wiley & Sons.

with H_2O_2 , 2-propanol and poly(ethylene glycol) and then drop-casting the solution onto a FTO glass substrate, followed by post-annealing in air to convert the film to WO_3 .²³ Non-oxide semiconductors have been synthesized by solution-based methods, as well. For example, $\text{Cu}_2\text{ZnSnS}_4$ was obtained by spin coating a homogenous hybrid ink containing thiourea, Sn^{2+} , Cu^{2+} and Zn nanoparticles in 2-methoxyethanol onto molybdenum-covered glass substrates, followed by air drying (at 200°C) and sulfurization processes in H_2S atmosphere at 560°C (Figure 4b).²⁴ Note that a post-growth annealing treatment is involved in all examples listed here either to achieve the desired crystallinity or compositions because the synthesis conditions are often not sufficient for the desired materials in a single step, as limited by the solution nature of the precursors or the reactions or both.

In addition to semiconductors, protective layers and catalysts have been synthesized by solution-based methods. For example, Liu *et al.* reported the synthesis of a ferrihydrite protection layer on the surface of Ta_3N_5 by immersing the substrates into a solution containing $\text{Fe}(\text{NO}_3)_3$ and NaNO_3 at 100°C (Figure 4d).²⁵ Further decoration of Co_3O_4 nanoparticles as OER catalysts was achieved hydrothermally by sealing the substrate with a precursor solution containing $\text{Co}(\text{CH}_3\text{COO})_2$ and NH_4OH in an autoclave at 120°C . Nickel-iron layered double hydroxide (NiFe-LDH) has been deposited on the surface of Ta_3N_5 nanorods as a protection layer via a two-step hydrothermal reaction at 120°C and 150°C , respectively (Figure

4c).²⁶ Thin films (5-10 nm) of Ni:FeOOH were deposited on various semiconductors (e.g., $\text{WO}_3/\text{BiVO}_4$, hematite, TiO_2 and Si) via a hydrothermal method at 100 °C to serve as an efficient water oxidation catalyst.²⁷

2.3 (Photo) Electrochemical deposition

The uniqueness of electrochemical deposition (ED) and photoelectrochemical deposition (PED) method lies in the usage of an external bias and sometimes illumination. On the one hand, it introduced more parameters, such as potential and current, to tune the composition, morphology and the corresponding performance of the deposited materials. On the other hand, the utilization of light to facilitate the deposition in the case photoelectrochemical processes not only reduces energy input for the synthesis, it also improves the interface between the target materials (e.g., catalysts) and the receiving substrates for better charge transfer. Another benefit is the selectivity – catalysts will be deposited only where they are needed (e.g., where the photogenerated holes are for OER reaction). The detailed mechanisms and examples of electrochemically deposited semiconductors and catalysts have been reviewed recently.²⁸ For instance, nickel molybdenum (Ni-Mo) catalyst has been electrodeposited under dark or light illumination on various photocathode materials to serve as efficient HER catalysts. Digdaya *et al.* reported an amorphous SiC photocathode coated with Ni-Mo, which was potentiostatically deposited at -1.0 V vs. Ag/AgCl under standard AM 1.5 illumination from mixed solution of nickel sulfate, boric acid and sodium molybdate.²⁹ Similar deposition was also reported by Pan *et al.* on Cu_2O photocathodes, but with constant current of -1.5 mA/cm² during deposition and nickel sulfamate as the nickel precursor.³⁰ In addition, various OER catalysts (e.g., transition metal (oxy)hydroxide) have been widely used on photoanode materials via ED/PED. For example, Liu *et al.* reported amorphous cobalt-iron hydroxide nanosheet catalysts with efficient OER activities in alkaline environment.³¹ Such catalysts were deposited on BiVO_4 photoanodes at a constant potential of -1.42 V vs. $\text{Hg}/\text{Hg}_2\text{SO}_4$ from the electrolyte containing equivalent amount of $\text{Co}(\text{NO}_3)_2$ and $\text{Fe}(\text{NO}_3)_2$. Kim *et al.* showed that FeOOH and NiOOH deposited on the BiVO_4 photoanode sequentially by PED method improved its turn-on potential (V_{on}) and photocurrent density (J_{ph}) at the same time.³² A wide spectrum of semiconducting materials and catalysts has been successfully prepared by (photo)electrochemical methods, making the technique a facile tool for the synthesis of nearly all photoactive materials for solar fuel applications.

3 Representative thin-film materials for solar fuel synthesis

As one of the most exciting research areas during the past decade, solar fuel synthesis has attracted enormous attention. As such, nearly all photoactive materials have been exploited for the purpose of solar fuel synthesis. Comprehensive reviews on such efforts can be found here.³³⁻³⁵ Without repeating these

prior publications, we mainly discuss thin film materials next. In doing so, our emphasis is placed on the common issues that limit the performance of a given material for solar-to-chemical energy conversion. Representative strategies in addressing these issues on prototypical materials are presented. In this subsection, we use discussions on charge behaviors and stability as a common thread to organize the contents. Additional considerations such as catalysis are presented in the following subsections. We organize the contents in this way because there is rarely a semiconductor that can meet all the common issues. As a result, most of study for photoelectrode materials have focused on solving one or multiple limitations of a certain

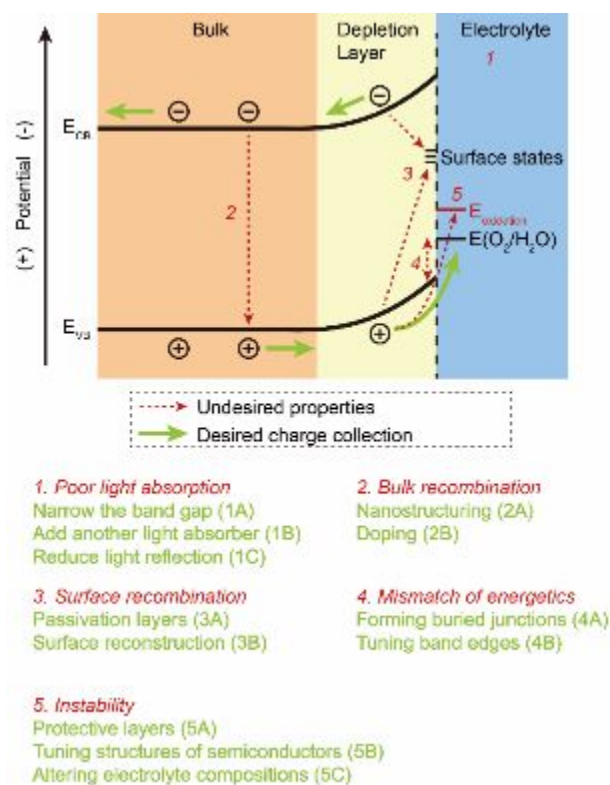


Figure 5 The Schematic shows the charge excitation, separation and transfer process (green arrows) in an n-type semiconductor in contact with aqueous electrolyte. E_{CB} : potential of conduction band minimum; E_{VB} : potential of valence band maximum; E_{oxidant} : potential of self-oxidation for the semiconductor; $E(\text{O}_2/\text{H}_2\text{O})$: potential of water oxidation. The undesired properties including poor light absorption, bulk/surface recombination, mismatch of energetics and instability are indicated by the red arrows, with the corresponded strategies listed below as green texts. The number of each strategy is also used in Table 1.

material with other promising properties. By organizing the content by undesired properties and corresponded solving strategies, we hope readers can clearly know the research efforts on developing thin-film materials for solar fuel synthesis. As shown in Figure 5, solar fuel synthesis on a solid-state material involves several key steps, including charge excitation, separation, transport and transfer. Of them, charge excitation is ensured by the optoelectronic properties of the materials. For semiconductors, the gap in the energy bands acts as a key enabling factor. Similar functionalities may be achieved following other mechanisms such as the plasmonic effect, the quantum confinement effect, or other similar effects on

emerging materials (e.g., 2D materials). An important issue that needs research attention here is the energy of photons that can be absorbed and how they match the solar spectrum. As has been shown by the classical Shockley-Queisser analysis, the optimum absorption edge for a single absorber would be 1.34 eV for solar-to-electricity conversion. For the purpose of solar fuel synthesis, the free energy gain of the target reactions imposes another constraint to the consideration, and the optimum absorption edge would be 1.6 eV if the reaction is water splitting.³⁶ Few materials match this absorption perfectly. A handful examples whose absorption edges are close to this desired value present new challenges such as mismatch of the band edge positions and stability. We will discuss strategies aimed at addressing these issues in 3.4 and 3.5.

The next step in solar fuel synthesis is charge separation and transport. Ideally, the only competing processes of this step would be radiative recombination, the result of which would be photons that may be reabsorbed. In reality, however, recombination by a variety of other mechanisms constitutes the biggest loss in solar-to-electricity conversion. Efforts developed to address this issue arguably represent the biggest portion of materials-related research on solar fuels. We devote the bulk of subsection 3.2 on these efforts.

After the charges emerge to the surface, how they are utilized would be the next issue to be addressed. The desired processes would be facile forward charge transfer for solar fuel synthesis. Competing processes, aside from surface recombination that may be regarded as a solid-state process, include corrosion (parasitic chemical reactions that damage the photoelectrode itself) and side reactions (parasitic reactions that compete with solar fuel formation). Moreover, the energetics at the solid/liquid interface is of critical importance. There are a handful of materials that are highly efficient in absorbing light, separating and transporting charges but feature significant mismatch of the energetics with desired solar fuel synthesis reactions. That is, the charges are simply not energetic enough to carry out the reactions as desired. We will discuss these issues in 3.3.

Table 1 summarizes reported efforts to address the common issues that limit the performance of a given material. The representative materials are organized in an alphabetic order of light absorbers considering that multiple strategies may be applied in one study. The configurations of photoelectrodes, strategies to address the issues (numbered in Figure 5) and testing electrolytes (with pH if possible) are listed. When possible, the performance metrics including the turn-on potentials (V_{on}), photocurrent density (J_{ph}) and stability are also listed. All potentials in Table 1 and main text are versus the reversible hydrogen electrode (RHE) potential if no specific reference electrode is referred to. For J_{ph} in Table 1, positive values are for water oxidation at 1.23 V and negative values are for water reduction at 0 V. For stability, the testing time and the J_{ph} during the test is noted.

3.1 Poor light absorption

3.1.1 Narrow the band gaps or add another light absorber to enhance light absorption

A common issue that limits the performance of materials with good optoelectronic properties (such as high light absorption coefficient, facile charge separation and transport) is the narrow absorption region relative to the overall solar spectrum. Two general strategies have been developed to address this issue, including narrowing the band gap and adding another light absorber. For instance, the utilization of TiO_2 for practical water splitting is limited mainly by its wide band gap (3.2 eV for the anatase phase), even though it exhibits high incident photo-to-electron efficiencies and good chemical stability. The wide band gap means it can only absorb light in the deep UV region. It was hypothesized that the band gap might be narrowed through methods such as self-doping of Ti^{3+} and/or oxygen vacancies by chemical reduction or ion doping.³⁷ To this end,

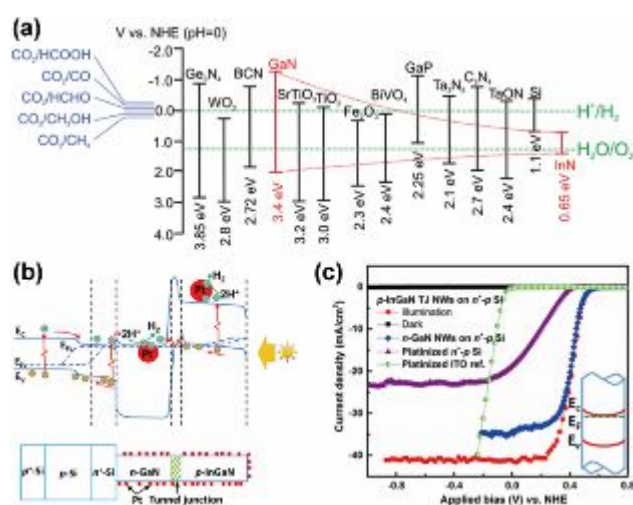


Figure 6 (a) Band edge positions of $In_xGa_{1-x}N$ in comparison with other commonly reported semiconductors. The red dotted line indicated the shift of band edges with x increasing from 0 to 1. The water oxidation and reductions potentials (green dotted lines) and various CO_2 reduction potentials are also presented. (b) The schematic shows the device structure and energy band diagram of integrated $InGaN/GaN/Si$ photocathode. (c) The photocurrent density vs. applied potential curves of $InGaN/GaN/Si$ photocathode shown in (b) in 1 M HBr solution, in comparison with other control samples including GaN/Si , platinized Si and platinized indium-doped tin oxide (ITO) substrate. Light intensity: 1.3 sun of AM 1.5G illumination. (a) reproduced from Ref. 77 with permission from the Royal Society of Chemistry. (b) and (c) reprinted with permission from ref. 61. Copyright 2015 American Chemical Society.

Yang *et al.* reported core-shell nanostructured “black” rutile TiO_2 , which was synthesized by first forming a reduced shell of TiO_{2-x} with TiO_2 nanoparticles and then post annealing in H_2S to dope S into the shell of the nanoparticles.³⁸ Diffuse reflectance spectrum indicated that the band gap of the treated TiO_2 was 1.3 eV narrower than pristine rutile TiO_2 . After assembled into photoelectrodes by spin coating, the S-doped rutile TiO_2 showed 30-fold increase of photocurrent density at 1.23 V and negative shift of turn-on potential by 280 mV compared with pristine rutile TiO_2 in 1 M NaOH electrolyte. It is noted that whether the broadened absorption is actually due to the shift of the band edge positions would require additional research.



Journal Name

ARTICLE

Table 1 Representative semiconductors for solar water splitting to illustrate strategies for common issues of photoelectrodes

Photoelectrode configuration ^a	Electrolyte (pH)	J_{ph} (mA/cm ²) ^b	V_{on} (V) ^c	Stability time (change of J_{ph} , mA/cm ²)	Strategies to solve issues ^d	Ref.
n-BiVO₄ (nanoporous)/FeOOH/NiOOH	1 M KBi with 0.1 M V ₂ O ₅ (9.3)	4.5	0.2	500 h (3.2)	2A, 3A, 5A, 5C	Lee ³⁹
n-BiVO₄ (nanoporous)/FeOOH/NiOOH	0.5 M KH ₂ PO ₄ (7)	4.4	0.2	48 h (2.73)	2A, 3A, 5A	Kim ³²
n-Mo:BiVO₄ (nanoporous, on nanocone substrate)/FeOOH/NiOOH	0.5 M KH ₂ PO ₄ (7)	5.82	0.2	5 h (5.7)	1C, 2A, 2B, 3A, 5A	Qiu ⁴⁰
n-Mo:BiVO₄ (on Ni/Sn)/NiFe-based catalysts	1 M KBi (9)	4.5	0.2	1000 h (2.5 to 2.6)	2B, 3A, 5A, 5B	Kuang ⁴¹
n-Mo, W:BiVO₄ /Pt	0.1 M Na ₂ SO ₄ /0.1 M KPi (6.8)	~1.9	~0.55	1800 s (0.5 to 0.28)	2B, 3A	Berglund ⁴²
n-W:BiVO₄ (nanoporous)/Co-Pi	0.1 M KPi (7.3)	3.6	0.3	1 h (4)	2A, 2B, 3A, 5A	Abdi ⁴³
p-Cu(In,Ga)Se₂ /n-CdS/Mo-Ti/Pt	0.5 M Na ₂ SO ₄ -0.25 M Na ₂ HPO ₄ -0.25 M NaH ₂ PO ₄ (6.8)	-30	0.6	3 h (-24 to -21)	3A, 4A, 5A	Kumagai ⁷
p-Cu₂O nanowires/n-Al:ZnO/n-TiO ₂ /RuO _x	0.5 M Na ₂ SO ₄ (5)	-8	0.48	55 h (-7 to -5)	2A, 3A, 4A, 5A	Luo ⁴⁴
p-Cu₂O nanowires/n-Ga ₂ O ₃ /n-TiO ₂ /RuO _x	0.5 M Na ₂ SO ₄ -0.1 M KPi (5)	-10	~1	120 h (-6.3 to -5.3)	2A, 3A, 4A, 5A	Pan ³⁰
p-Cu₂O (microcrystalline)/n-Ga ₂ O ₃ /n-TiO ₂ /Pt	0.5 M Na ₂ SO ₄ -0.1 M KH ₂ PO ₄ (4.26)	-6.3	1.02	2 h (-3.7 to -3.3)	2A, 3A, 4A, 5A	Li ⁴⁵
p-Cu₂O /n-Al:ZnO/n-TiO ₂ /Pt	1 M Na ₂ SO ₄ (4.9)	-7.8	~0.5	20 min (-5.7 to -4.4)	3A, 4A, 5A	Paracchino ⁴⁶
p-Cu₂O /n-ZnS/n-TiO ₂ /Pt	0.2 M K ₂ HPO ₄ (7)	-2.2	0.72	30 h (-0.5)	3A, 4A, 5A	Dai ⁴⁹
p-Cd:Cu₂ZnSnS₄ /n-CdS/Ti-Mo/Pt	1 M K ₂ HPO ₄ /KH ₂ PO ₄ (7)	-17	~0.6	1 h (-11 to -9)	2B, 3A, 4A, 5A	Tay ⁴⁷
n-Fe₂O₃ /NiFeO _x	1 M NaOH (13.6)	1.3	0.4	10 h (0.7)	2A, 3A, 3B	Jang ²²
TiSi ₂ nanonets/ n-Fe₂O₃	1 M NaOH (13.6)	1.6	0.9	-	2A	Lin ¹⁷
n-Fe₂O₃ nanorods (H ₂ -treated)	1 M NaOH (13.6)	2.28	0.87	-	2A, 3B	Li ⁴⁸
n-Si:Fe₂O₃ (cauliflower-type)/Al ₂ O ₃ /FeNiO _x	1 M KOH (13.6)	2.75	0.7	8 h (2.75)	2A, 2B, 3A	Morales-Guio ⁴⁹
n-Fe₂O₃ nanorods (H ₂ -treated)/n-TiO ₂ /Co-Pi	1 M KOH (13.6)	6	0.55	100 h (6)	2A, 2B, 3A	Jeon ⁵⁰
n-Pt:Fe₂O₃ /Co-Pi	1 M NaOH (13.6)	4.23	~0.6	-	2A, 2B, 3A	Kim ⁵¹
n-Fe₂O₃ /IrO _x	0.1 M KNO ₃ (1.01)	~0.7	0.6	5 h (0.65 to 0.6)	2A, 3A, 3B, 5A	Li ⁵²
n-Fe₂O₃ /Ir dinuclear heterogeneous catalyst	0.1 M KNO ₃ (6)	1.5	0.55	10 h (1.5)	2A, 3A, 3B, 5A	Zhao ⁵³
n-GaAs/p-InGaP /n-TiO ₂ /Ni	1 M KOH (13.6)	8.5	-0.8	80 h (8.5 to 7.3)	1B, 2B, 3A, 4A, 5A	Verlage ⁵⁴
n-p GaAs /p-type ohmic contact (Au/Pt/Ti/Pt)/IrO _x .nH ₂ O	0.5 M H ₂ SO ₄	~17	~0.56	-	2B, 3A, 4A, 5A	Kang ¹¹
p-n GaAs /n-type ohmic contact (AuGe/Ni/Au)/Pt	0.5 M H ₂ SO ₄	-23.1	1.022	192 h (-25 to -21.3)	2B, 3A, 4A, 5A	Kang ¹¹
p-n GaInAs/p-GaInP /n-GaInP/n-AlInP/n-GaInP/PtRu	3 M H ₂ SO ₄	-13.2	~0.65	10 h (-14 to -12)	1B, 2B, 3A, 4A, 5A	Young ⁵⁵
p-GaInP₂ /TiO ₂ /cobaloxime molecular catalyst/TiO ₂	0.1 M NaOH (13)	-9	~0.74	20 h (-10 to -5)	3A, 5A	Gu ⁵⁶
p-GaInP₂ /TiO ₂ /MoS _x	0.5 M H ₂ SO ₄	-11	0.5	20 h (-11 to -9.2)	3A, 5A	Gu ⁵⁷
n-GaN /Co-Pi	0.5 M KPi (7)	1.5	-0.2	1 h (1.1 to 0.6)	3A, 5A	Kamimura ⁵⁸
n-Si nanowires/ n-TiO₂	1 M KOH (13.6)	0.25	~0	1 h (0.28)	1B, 1C, 2A, 5A	Hwang ⁵⁹
n-Si nanowires/ n-Fe₂O₃	1 M NaOH (13.6)	0.85	0.6	3 h (0.15)	1B, 2A, 5A	Mayer ¹⁸

n-Si needles/ n-Ta₃N₅ /NiFeO _x	0.1 M KOH (13)	2.6	0.6	24 h (1.7 to 0.7)	1B, 2A, 3A, 5A	Narkeviciute ⁶⁰
n⁺p-Si /n-GaN/ p-InGaN /Pt	1 M HBr	-40.6	0.5 vs. NHE ^e	3 h (-20)	1A, 1B, 1C, 3A, 4A, 5A	Fan ⁶¹
p-i-n amorphous Si (a-Si) /n-TiO ₂ /Pt	0.5 M K ₂ HPO ₄ (4)	-11.6	0.93	12 h (-10.7 to -10)	3A, 4A, 4B, 5A	Lin ¹⁶
n-i-p a-Si /CoO _x	1 M KOH (13.6)	9	~0.5	3 h (9 to 7.5)	3A, 4B, 5A	Qin ⁶²
p-i amorphous SiC (a-SiC) /n-TiO ₂ /Ni-Mo	0.5 M K ₂ HPO ₄ (4)	-8.3	0.8	12 h (~-7.3)	3A, 4A, 4B, 5A	Digdaya ⁶³
p-i-n a-SiC /n-TiO ₂ /Ni/Ni-Mo	1 M KOH (13.6)	-14	0.8	1 h (-14 to -5.5)	3A, 4A, 4B, 5A	Digdaya ²⁹
p-i-n Si/p-i a-SiC	0.1 M H ₃ NSO ₃ (3.75)	-5.1	1.2	1 h (-5.1)	2B, 4A	Han ⁶⁴
n-Ta₃N₅ /n-GaN/Co-Pi	0.5 M KPi (13)	8	0.65	10 h (8 to 6)	3A, 5A	Zhong ⁸
Ta:TiO ₂ / n-Ta₃N₅ /Co-Pi	0.5 M K ₂ HPO ₄ (13)	0.77	0.8	-	3A	Hajibabaei ⁶⁵
n-Ba:Ta₃N₅ nanorods/Co-Pi	0.5 M K ₂ HPO ₄ (13)	6.7	0.65	20 min (4.5)	2A, 2B, 3A, 5A	Li ⁶⁶
n-Mg, Zr:Ta₃N₅ /CoO _x -FeO _x	0.1 M Na ₂ SO ₄ (13)	2.3	0.55	10 min (1.65 to 1.1)	2B, 3A, 5A	Seo ⁶⁷
n-Ta₃N₅ /ferrihydrite/Co ₃ O ₄	1 M NaOH (13.6)	5.2	0.6	6 h (5.5 to 5)	3A, 5A	Liu ²⁵
n-Ta₃N₅ /TiO _x /ferrihydrite/Ni(OH) _x /Co-Ir complex	1 M NaOH (13.6)	12.1	0.6	20 min (7 to 6)	3A, 5A	Liu ⁶⁸
n-Ta₃N₅ nanotubes/MgO/Co(OH) _x	1 M NaOH (13.6)	5.5	0.8	30 min (7.1 to 6.2)	2A, 3A, 5A	He ⁶⁹
n-Ta₃N₅ nanotubes/Co(OH) _x /Co-Pi	1 M NaOH (13.6)	6	0.85	5 h (2.1 to 2.4)	2A, 3A, 5A	He ⁷⁰
n-Ta₃N₅ nanorods/NiFe layered double hydroxide/Co(OH) _x /Co-Pi	1 M KOH (13.6)	6.5	~0.7	2 h (6.2 to 4.5)	2A, 3A, 5A	Wang ²⁶
n-S:TiO₂	1 M NaOH (13.6)	4.5	0.14	30 h (12% decay)	1A, 2B	Yang ³⁸
n-TiO₂ nanorods/g-C ₃ N ₄ /Co-Pi	0.1 M Na ₂ SO ₄ (6.8)	1.6	0.3	10 h (1.6)	1B, 2A, 3A	Li ⁷¹
n-WO₃ nanoflakes (H ₂ /O ₃ treated)	0.1 M Na ₂ SO ₄ (6.8)	2.25	0.57	10 h (2 to 2.2)	2A, 3B	Zhang ⁷²
n-WO₃ (mesoporous)/W _{1-x} O _{3-y}	0.5 M Na ₂ SO ₄ (6.8)	2.81	0.5	10 h (2.5 to 2)	3B, 5B	Ma ²³
TiSi ₂ nanonets/ n-WO₃ /Mn-based catalyst	1 M KCl (7)	2.2	0.5	2 h (4% decay)	3A, 5A	Liu ⁷³
n-WO₃ nanoplates	0.1 M H ₂ SO ₄	3.7	0.6	500 s (3.7 to 2.7)	2A, 3B, 5B	Wang ⁷⁴
n-WO₃ /Co-Pi	0.1 M KH ₂ PO ₄ (7)	0.23	0.41	12 h (0.34)	3A, 5A	Seabold ⁷⁵
n-Yb:WO₃	0.05 M Na ₂ SO ₄ (5.4)	0.57	0.7	-	2B	Liew ⁷⁶

^aIn the photoelectrode configuration, the light absorber is highlighted in bold font. The layer of material placed on the right side is closer to the electrolyte.

^bThe positive values are for water oxidation at 1.23 V, and the negative values are for water reduction at 0 V.

^cAll the potentials are versus reversible hydrogen electrode if no specific reference electrode is mentioned.

^dFor the ease of presentation, strategies to solve the common issues are numbered as shown in Figure 5.

^eNHE is short for normal hydrogen electrode.

A better accepted example in tuning the band structures by varying the compositions is found in nitride semiconductors. For instance, GaN features a direct band gap of 3.4 eV, with the conduction band and valence band edges straddling the water splitting potentials. As a photoelectrode, early turn-on potentials and good fill factor have been obtained. Notwithstanding, its practical applications for solar water splitting are limited due to the wide band gap. To further actualize the promises held by this material, researchers have tried to incorporate In during the synthesis, which was shown to reduce the band gap from 3.4 eV (pure GaN) and to 0.65 eV (pure InN) (Figure 6a).⁷⁷ Significantly, the change of the band gap between the two extremes is continuous, depending on the In concentrations in GaN. When used for water splitting applications, a key challenge is the stability of the material. In one example of such efforts, In_{0.21}Ga_{0.79}N films (E_g=2.3 eV) with an average thickness of 1 μm were synthesized on sapphire substrates by MOCVD.⁷⁸ After tested in 1 M HCl at 1.5 V vs. SCE under illumination, In and Ga elements were found in the

electrolyte, confirming the material is being etched during the test. In another example, AlOtaibi *et al.* reported the synthesis of InGaN/GaN core/shell nanowire arrays ($L=400\text{--}500\text{ nm}$) on Si substrate.⁹ With a band gap of 2.38 eV, the integrated photoanode reached 23 mA/cm² current density at 1 V vs. Ag/AgCl in a 1 M HBr electrolyte under AM1.5G illumination. Interestingly, the morphology and composition of the nanowires were confirmed to remain the same even after 24 hours PEC measurements. The superior stability may be explained by the MBE growth itself, which leads to nitrides of N-termination. It has been shown by Kibria *et al.* that such a termination offers better stability than Ga termination, which is expected for MOCVD-grown materials.⁷⁹

Another common application of InGaN is to serve as the photocathode. For example, using Mg as a dopant, Fan *et al.* reported the synthesis of 600 nm p-InGaN with 25% In composition, which was connected with n-GaN nanowires (150 nm) by tunnel junctions on a n⁺p-Si substrate (Figure 6b).⁶¹ After decoration with Pt HER catalysts, the integrated photocathode reached a saturated photocurrent density of -40.6 mA/cm² at 0.26 V vs. NHE in 1 M HBr, almost twice that of platinumized n⁺p-Si substrates (Figure 6c). The improved

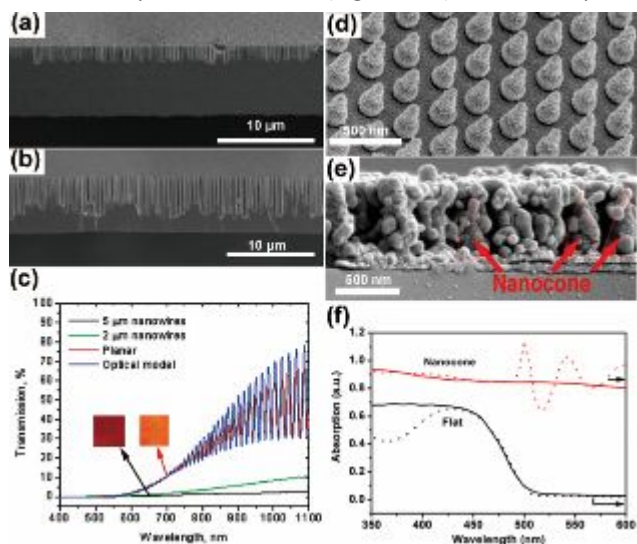


Figure 7 The SEM images of (a) 2.5 μm and (b) 5 μm Si nanowire arrays on 7.5 μm Si windows. (c) Transmission spectra of Si windows before and after etching to form 2.5 μm and 5 μm (as shown in a,b) nanowires. The blue line was from the optical model of the planar Si window. The insets are backlit color images of the membrane before and after etching. (d) and (e) are SEM images of SiO₂/Pt/SnO₂ nanocone arrays and Mo:BiVO₄ on nanocone arrays, respectively. Some exposed nanocones were marked in red in (e). (f) UV-VIS absorption spectra (solid lines) of Mo:BiVO₄ grown on nanocone arrays and FTO glasses. The simulated absorption spectra were shown in dash lines. (a-c) reprinted with permission from ref. 80. Copyright 2010 American Chemical Society. (d-f) from ref. 40. Reprinted with permission from AAAS.

performance was attributed to a combination of the antireflection effect by the nanowires, enhanced carrier extraction and reduced surface recombination. Notably, stable HER over 3 hours was observed at 0.06 V vs. NHE in 1 M HBr. To tune the band structures by changing the compositions of materials using methods such as MBE has been shown as a promising method to enhance light absorption by narrowing

down the band gaps of semiconductors. By controlling the suitable compositions, the light absorption range can be extended from ultraviolet part to near-infrared region, covering the visible light spectrum. However, new issues are introduced by such approaches. For instance, to achieve low-defect and high-quality materials, high-vacuum techniques are usually necessary, greatly raising the cost of the synthesis process. Low-cost alternative synthesis methods, such as solution-based ones, tend to yield materials of inadequate quality that are characterized by low solar-to-chemical-energy efficiencies. How to balance the efficiency and cost will continue to be a key focus for efforts focused on tailoring materials optoelectronic properties by changing their compositions.

Another strategy to broaden the range of light absorption is to complement the wide band gap material with narrow band gap absorbers. A large number of examples have been reported toward this direction. For example, Mayer *et al.* reported a dual-absorber photoanode consisting of Si nanowires (Si NWs) and α-Fe₂O₃.¹⁸ Thin films of α-Fe₂O₃ were deposited by ALD on the surface of high-aspect-ratio Si NWs with conformal coverage. Owing to the larger E_g (2.1 eV) of α-Fe₂O₃ compared with the one of Si (E_g=1.1 eV), incident photons with longer wavelength (600 nm < λ < 1100 nm) were transparent for α-Fe₂O₃ and absorbed by the underlying Si. As a result, the utilization of overall solar spectrum was improved. In addition, the appropriate band alignment between n-Si and α-Fe₂O₃ created an appreciable band-bending depth, providing additional photovoltages and guaranteed electron injection from α-Fe₂O₃ to Si. As expected, the dual-absorber photoanode showed a more cathodic turn-on potential (0.6 V) and a higher photocurrent density in a 1.0 M NaOH electrolyte compared with the performance of planar α-Fe₂O₃ thin film grown on the FTO-coated glass substrate. Similarly, Hwang *et al.* reported a photoanode consisting of n-type Si NWs and thin films (35 nm) of n-TiO₂ on the surface.⁵⁹ The construction of n/n junction between n-Si and n-TiO₂ not only improved the charge separation due to the band bending at the junction, but also introduced a potential barrier at the interface that blocked the holes back to the TiO₂ layer and reduced the loss of holes. In one of these examples, a thin layer of g-C₃N₄ (E_g ~ 2.7 eV) was deposited onto TiO₂ nanorods by chemical bath deposition, leading to a red shift of light absorption in comparison with bare TiO₂.⁷¹ An important consideration in approaches like this is how to manage charge flows. In this particular case, due to the formation of a heterojunction between TiO₂ and C₃N₄, photogenerated electrons in C₃N₄ transfer to the conduction band of TiO₂, and photogenerated holes move from TiO₂ to C₃N₄. As a result, the TiO₂/g-C₃N₄ combination enabled a photocurrent density of 1.15 mA/cm² at 1.23 V in 0.1 M Na₂SO₄ (pH=6.8), 2.6 times of that measured on bare TiO₂. In theory, the strategy of combining materials of complementary light absorption would enable broad light absorption for high performance; in practice, however, how to build a low-defect and intimate interface between different materials remains as a challenge.

3.1.2 Reduce reflection to avoid light absorption losses

As has been shown in research on solar cells, optical loss due to reflection contributes significantly to the low performance of planar semiconductor materials when used for solar energy harvesting applications. Several strategies have been developed to meet this challenge. In the first approach, light absorption was shown to be enhanced by constructing nanostructures on the surface. For example, Garnett *et al.* discovered that by carefully controlling the diameter and density of Si nanowires, the path length of incident solar irradiation was enhanced by up to a factor of 73 when compared with Si thin films of the same thickness, thanks to the strong light trapping effect by the nanowire morphologies (Figure 7a-c).⁸⁰ Maiolo *et al.* reported Si microwires synthesized through a vapor-liquid-solid method with Au as the catalyst.⁸¹ With a length between 10 and 30 μm , these Si wires showed enhanced photocurrent density and photovoltage in a 1,1'-dimethylferrocene (Me_2Fc)⁺⁰ redox system in CH_3OH when compared with planar samples. Dai *et al.* reported Si nanowire (NW) arrays synthesized through a Ag seeds assisted etching process.⁸² In comparison with planar silicon, the Si NWs showed broadband anti-reflection properties with an optical reflectance of $\sim 0\%$, while the planar one reflected 19% of sunlight at the Si-water interface.

In another approach, designing suitable substrates underneath the semiconducting light absorber was also shown to enhance light absorption through recycling incident photons. For instance, Qiu *et al.* reported a mesoporous BiVO_4 deposited on a pre-designed nanocone substrate (Figure 7d-f).⁴⁰ The light absorption was enhanced due to light trapping through multiple light scattering in the nanocone structure. Simulations of the electromagnetic wave distribution at $\lambda=500\text{ nm}$ for Mo:BiVO_4 on the nanocone substrate and a flat FTO-coated glass substrate indicated that the incident light was diffracted and redistributed in the nanocone area, owing to the match of the incident light wavelength and the distance between neighbouring nanocone arrays. The results were also supported by enhanced absorption by BiVO_4 deposited on the nanocone substrate in UV-vis absorption spectrum. Similarly, Shi *et al.* reported the introduction of a distributed Bragg reflector (DBR) layer to improve the performance of a tandem cell device consisting of $\text{BiVO}_4/\text{WO}_3$ photoanode and DSSC.⁸³ The DBR layer was placed on the back side of FTO glass for the $\text{BiVO}_4/\text{WO}_3$ photoanode and served as the conductive counter electrode for the DSSC. The DBR layer consisting of multiple layers of materials with high- and low-refractive indices would reflect short-wavelength photons ($\lambda < 500\text{ nm}$) while transmitting long-wavelength photons, leading to photo recycling by the BiVO_4 photoanode. A η_{STH} of 7.1% was achieved, corresponding to a J_{ph} of 5.75 mA/cm^2 , which was 1.1 mA/cm^2 higher than the one without DBR layers.

The strategies to reduce the light absorption can be widely implemented to different semiconductor materials. For instance, the light trapping effect and anti-reflection properties through nanostructuring have been achieved on various semiconductor platforms including Si, metal oxides and metal nitrides, etc. with carefully controlled dimensions and structures. In addition, it can serve the purpose more than reducing the light reflection, such as enhancing the surface area

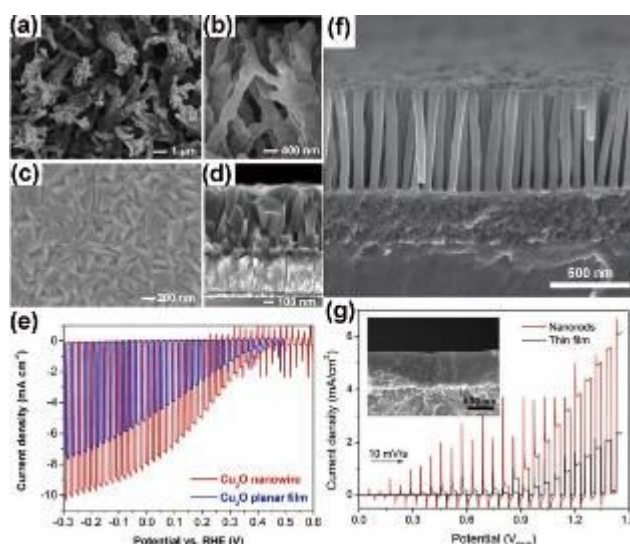


Figure 8 The SEM images of Cu_2O nanowires and planar Cu_2O samples were compared in (a) to (d). (a) Top view and (b) cross-sectional view of Cu_2O nanowires. (c) Top view and (d) cross-sectional view of planar Cu_2O . (e) J-V curves of Cu_2O devices with nanowire or planar morphologies in pH 5 electrolyte under AM 1.5G illumination. (f) Cross-sectional SEM image of Ta_3N_5 nanorods. (g) J-V curves of Ta_3N_5 nanorods and planar thin films with IrO_2 as the catalysts in 0.5 M Na_2SO_4 (pH 13) under AM 1.5G illumination. The inset was the cross-sectional SEM image of planar Ta_3N_5 thin films on the Ta foil. (a-e) reprinted with permission from ref. 44. Copyright 2016 American Chemical Society. (f-g) reproduced from ref. 88 with permission from John Wiley & Sons.

for more catalytic sites and reducing charge recombination (more details in Section 3.2.1). At the same time, some issues may also occur due to enlarged contact area between semiconductors and electrolytes, such as more severe surface charge recombination. Future strategies need to balance between the benefits and drawbacks.

3.2 Bulk recombination

3.2.1 Nanostructuring to match the short diffusion length

In one scenario, the recombination of photo-generated charges would take place due to the mismatched diffusion length of charge carriers with the light penetration depth. For instance, hematite features a light penetration depth of 46 nm at wavelength of 450 nm,⁸⁴ but its hole diffusion length is reported to be 2-4 nm,⁸⁵ meaning that most photogenerated holes would recombine with electrons before they are transferred to the semiconductor-electrolyte interface. To address this issue, nanostructuring has been applied to reduce the distance of charge transfer from bulk to surface while still ensuring sufficient light absorption, resulting in improved charge collection efficiency. One better-known example of this strategy is the cauliflower-type silicon-doped hematite thin film synthesized by atmospheric pressure chemical vapor deposition (APCVD) from $\text{Fe}(\text{CO})_5$ and tetraethoxysilane on FTO-coated glass at 415 $^\circ\text{C}$, reported by Kay *et al.* in 2006.¹³ Its photocurrent density in 1 M NaOH at 1.23 V under AM 1.5 light illumination ($100\text{ mW}/\text{cm}^2$) could reach 2.3 mA/cm^2 , which can be further improved to 2.7 mA/cm^2 with the addition of Co^{2+} catalysts.

Another example was found in electrodeposited Cu_2O , whose electron diffusion length (20 to 100 nm)⁸⁶ is shorter than the light penetration depth (several μm at 2.4 eV)⁸⁷ by a large margin. Increasing the aspect ratios of nanostructured Cu_2O has proven a promising method to address this issue. For example, Luo *et al.* synthesized Cu_2O nanowire arrays via anodization and post annealing treatments.⁴⁴ $\text{Cu}(\text{OH})_2$ nanowire was first formed by anodization; it was then converted to Cu_2O during the post annealing in Ar atmosphere at 600 °C, featuring diameters of 100-300 nm and lengths of 3-5 μm (Figure 8a-d). Additional electrodeposited Cu_2O was introduced to cover the exposed Cu substrate, which was shown to significantly reduce charge recombination due to the contact between the Cu substrate and the protection layer (Al-doped ZnO). With further decoration of TiO_2 and RuO_x (as the HER catalyst), the Cu_2O nanowire photoelectrode achieved -10 mA/cm^2 photocurrent density at -0.3 V and a turn-on potential of 0.48 V in 0.5 M Na_2SO_4 buffered at pH 5 (Figure 8e). By comparison, planar Cu_2O films showed -7.8 mA/cm^2 photocurrent density at the same applied potential, indicating the effectiveness of the nanostructuring strategy.

Along the line of using nanostructures to help solve the mismatch between charge diffusion and optical depth, directly growing thin film light absorbers on nanostructures is yet another idea that has been exploited in the literature. For example, Lin *et al.* reported thin-film hematite (25 nm) grown on TiSi_2 nanonets by atomic layer deposition (ALD) using $\text{Fe}_2(\text{O}^t\text{Bu})_6$ and H_2O as precursors.¹⁷ The TiSi_2 nanonet substrate not only provided a high surface area for better charge collection, but also served as a highly conductive charge collector. As a result, the nanonet-based hematite photoelectrodes achieved 1.6 mA/cm^2 photocurrent density at 1.23 V in 1 M NaOH, which was three times higher than the planar thin film with the same thickness. To this end, Qiu *et al.*'s work of depositing mesoporous BiVO_4 on nanocone substrates may be regarded as similar.⁴⁰ Besides the ability to enhance the light absorption as mentioned previously, the nanocone structure reduced the charge transport distance in the photoelectrode, increasing charge collection efficiencies. Consequently, for the BiVO_4 nanoporous film of the same thickness on nanocone substrate and flat FTO glass substrate, the former showed a much higher photocurrent density (4.18 mA/cm^2) at 1.23 V in pH 7 phosphate buffer than the latter (2.10 mA/cm^2). With the introduction of $\text{Fe}(\text{Ni})\text{OOH}$ OER catalyst, the photocurrent density was further improved to 5.82 mA/cm^2 .

Another way of growing light absorbing nanostructures is to take advantage of templates with preformed nanoscale features. For instance, Ta_3N_5 nanorods were prepared using an anodization method with porous anodic alumina (PAA) as the template in a H_3BO_3 solution under high applied DC voltages (600-650 V), followed by high-temperature annealing in NH_3 .^{26, 66, 88} Using this method, Li *et al.* reported that a 600 nm thick nanorod arrays showed enhanced photocurrent density at 1.23 V in 0.5 M Na_2SO_4 (by 2.2 times at pH 13) with IrO_2 as a catalyst when compared with planar thin films of the same thickness and catalysts (Figure 8g).⁸⁸ The improvement was attributed to the decreased distance for the photo-generated holes to reach

the Ta_3N_5 surface in the nanorod configuration. As far as Ta_3N_5 is concerned, although nanostructures have been shown effective in improving the performance, the hole diffusion distance still remains a debate. On the one hand, Ziani *et al.* reported carrier lifetimes ranging from 3.1 to 8.7 ps in Ta_3N_5 thin films based on transient spectroscopy measurements. These values would corresponded to a diffusion length between 3 and 9 nm.⁸⁹ On the other hand, Respini *et al.* reported a carrier lifetime of 1.6 ms based on time-resolved microwave conductivity measurements, corresponding to a diffusion length of 18,000 nm.⁹⁰ Further studies are necessary to reconcile the apparent discrepancies.

The advantages of nanostructuring have been discussed in Section 3.1.2. It is a versatile strategy for semiconductors suffering from short diffusion lengths. In addition, it may introduce more benefits at the same time, such as enhancing light absorption and increasing catalytic surface areas. However, large surface areas introduced by nanostructuring may also lead to side effects such as more defect states and more severe surface charge recombination.

3.2.2 Doping to enhance charge transport

In the literature, it has been commonly referred to that high carrier concentration would improve charge collection. As will be summarized in this subsection, a number of efforts have been applied to increase charge carrier concentrations through approaches such as doping. However, how these approaches work has been poorly discussed. For instance, for an n-type semiconductor (e.g., metal oxide photoanode), dopants that are introduced to increase electron concentrations would decrease hole concentrations under equilibrium conditions according to the mass law. As such, these approaches may be regarded as decreasing bulk recombination thanks to the decrease of the minority carrier concentrations. A more common way of understanding the effect was often referred to in the literature as increasing the majority carrier concentration to improve the transport of photogenerated electrons (in the case of an n-type photoanode); as such, the utilization of photogenerated holes is improved, as well, due to reduced bulk recombination. These two views are actually consistent, just from different angles. A good example in this sub-category is found in hematite, which usually features relatively low majority carrier concentrations ($<10^{18} \text{ cm}^{-3}$).⁸⁴ Doping has been popularly sought as an effective method to change the situation. An added benefit of doing so is the shift of the equilibrium Fermi levels of electrons (toward the more negative direction), so as to increase the splitting between the Fermi level and the water oxidation potentials and, hence, the degree of band bending for better charge separation.

For instance, Pt^{4+} , in the form of chloroplatinic acid, was added into the FeCl_3 -containing solutions during the synthesis of β - FeOOH thin film on FTO coated glass at 100 °C, followed by a two-step annealing process at 550 °C and 800 °C to form Pt-doped hematite.⁵¹ With an optimized thickness (500 nm) of the hematite thin film and a Pt/Fe ratio of 5%, the photoelectrode exhibited 74% enhancement of photocurrent density at 1.23 V in comparison with the undoped one. The Mott-Schottky analysis showed the donor density increased by one order of

magnitude, supporting the role of Pt^{4+} as a dopant into hematite, which improved its electrical conductivity. Along the same line, Li *et al.* treated hydrothermally synthesized WO_3 nanoflakes with chemical etching and reduction by poly(vinyl pyrrolidone) and ascorbic acid, respectively,⁹¹ resulting in porous WO_3 nanoflakes with increased surface oxygen vacancies (due to the reduction of W^{6+} to W^{5+}). The high oxygen vacancies not only increased the carrier concentrations, but also narrowed the band gap by 0.1 eV. Consequently, the water oxidation performance at 1.23 V in 1 M H_2SO_4 increased from 0.62 mA/cm^2 for pristine WO_3 nanoflakes to 1.10 mA/cm^2 for the etch-reduced WO_3 nanoflakes. In another study, Liew *et al.* reported Yb-doped WO_3 thin films (with thicknesses of 400 to 520 nm) by co-sputtering of WO_3 and Yb, followed by post annealing in air at 550 °C.⁷⁶ EIS analyses indicated a decreased charge transfer resistance and an increased carrier concentration after <0.1 at.% Yb doping, which was attributed to the increased oxygen vacancies due to the substitution of W^{6+} by Yb^{3+} . As a result, the photocurrent densities increased from 0.5 mA/cm^2 for bare WO_3 to 1.3 mA/cm^2 Yb-doped WO_3 at 1.2 V vs Ag/AgCl in 0.05 M Na_2SO_4 (pH=5.4).

Mo^{6+} and W^{6+} have been shown to be the most significant dopant for BiVO_4 , which can substitute V^{5+} to increase the carrier concentrations. For example, Berglund *et al.* reported Mo and W doped BiVO_4 by e-beam evaporation of Bi, V, Mo and W.⁴² Both W and Mo doped BiVO_4 showed higher photocurrent density at 1.23V than bare BiVO_4 , while W/Mo co-doped BiVO_4 showed the highest value in pH 6.8 phosphate buffer solutions. In a different system, Han *et al.* introduced a gradient dopant profile to amorphous SiC to improve charge collection.⁶⁴ A 10 nm p-type amorphous SiC was first deposited via boron doping in a PECVD growth, followed by another 40 nm p-type amorphous SiC with a reduced dopant concentration and 40 nm intrinsic amorphous SiC. Due to the increased thickness of the depletion region between p-type and intrinsic SiC, the drift charge transport was enhanced in comparison to the diffusion-controlled process in intrinsic SiC, leading to an anodic shift of the turn-on potentials (~200 mV). When coupled with a Si photovoltaic module, the photocathode achieved the photocurrent density of -5.1 mA/cm^2 at 0 V in 0.1 M sulfamic acid with pH 3.75 under 1 sun illumination. The last example connects this line of research with those focused on improving photovoltaics through controlling the energetics within the buried junctions.

Doping is a promising strategy to enhance the charge transport. On the one hand, such a method has been well-developed in semiconductor fabrication industries, which provides a rich knowledge base to tap into. On the other hand, various dopant elements have been explored, offering many options to modify semiconductors. However, challenges still remain for the doping strategy, such as how to achieve uniform dopants distribution.

3.3 Surface recombination

Even for pristine semiconductors, their surfaces are rich in electronic states whether in vacuum or in contact with a metal electrode. In addition to the types of states that would be

abundant in bulk (e.g., due to dopants and/or impurities), surfaces feature unique defects such as dangling bonds and structural imperfections, which often introduce electronic states within the bandgap. These states are the origins for severe recombination at or near the surface. Significant research efforts have been devoted to understanding and addressing these recombination processes as they play important roles in defining the properties of the overall device. The situation is significantly more pronounced for photoelectrodes in photoelectrochemical applications because the surfaces are now in contact with a liquid where chemical reactions take place. Besides the usual suspects that would introduce surface states, chemisorbed species that are either reactants, intermediates or products act as centers to promote charge recombination. Below we discuss strategies that have been attempted to study and deal with this issue.

3.3.1 Use electron/hole scavengers to study the extent of surface recombination

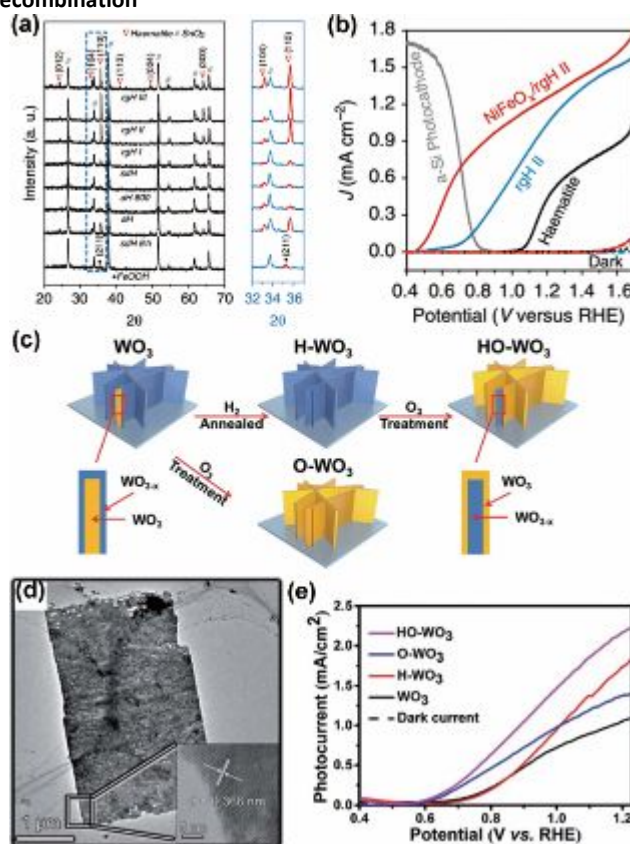


Figure 9 (a) X-ray diffraction patterns of different hematite samples. aH: ALD-grown hematite; aH 800: ALD-grown hematite annealed in at 800 °C in air; sdH: solution-derived hematite; rgH I, rgH II, rgH III: hematite subjected to regrowth treatment for one, two and three times, respectively. (b) J-V curves of various hematite samples in 1 M NaOH electrolyte. NiFeO_x/rgH II: rgH II sample coated with NiFeO_x. The J-V curve of amorphous Si (a-Si) photocathode behind the hematite was also shown. (c) The schematic shows the synthesis and structures of WO_3 nanoflakes, hydrogen-treated WO_3 (H- WO_3), ozone-treated WO_3 (O- WO_3) and hydrogen/ozone-treated WO_3 (HO- WO_3). (d) The HRTEM image of HO- WO_3 sample. (e) The J-V curves of various WO_3 photoelectrodes in 0.1 M Na_2SO_4 under AM 1.5G illumination. (a-b) reproduced from ref. 22 with permission from Springer Nature. (c-e) reproduced from Ref. 91 with permission from the Royal Society of Chemistry.

Among the various techniques to study surface recombination, using electron/hole scavengers has been widely applied as an important strategy. Taking hole scavengers as the example, they are usually reagents that can be more easily oxidized compared with water, which in principle can eliminate the surface charge recombination. To better reflect the effect, the photocurrent density (J_{ph}) can be expressed via a simplified charge transfer process⁹²:

$$J_{ph} = J_{abs} \times \eta_{sep} \times \eta_{inj} \quad (3.1)$$

In the equation, J_{abs} is the photon absorption rate; η_{sep} is the separation efficiency, representing the fraction of holes reaching the electrode/electrolyte interface without recombining with electrons in the bulk; η_{inj} is the charge injection efficiency, representing the fraction of holes for desired oxidation reaction (e.g., water oxidation or scavenger oxidation) without recombining with electrons at the surface. When the hole scavenger is present, η_{inj} should be 100%. With the assumption that the existence of hole scavenger does not affect J_{abs} and η_{sep} , η_{inj} for water oxidation can be derived from the ratio of J_{ph} for water oxidation and hole scavenger oxidation. Furthermore, J_{abs} can be estimated from the light absorption spectrum of photoelectrodes. The measured J_{ph} for hole scavenger oxidation can be used to calculate η_{sep} , helping to understand the extent of bulk recombination.

For instance, Zhong *et al.* used H_2O_2 as the hole scavenger to test $BiVO_4$ photoanodes and compared it with the performance in the same electrolyte but without H_2O_2 .⁹³ The η_{inj} for water oxidation was less than 60% at 1.2 V, which was improved significantly to near 100% after the deposition of Co-Pi. This demonstrated the effectiveness of Co-Pi to enhance the charge injection efficiency for water oxidation and reduce the surface charge recombination. Similarly, Liu *et al.* compared the performance of bare Ta_3N_5 and Ta_3N_5 with Co_3O_4 nanoparticles using H_2O_2 as the hole scavenger.²⁵ The η_{inj} for water oxidation increased from less than 20% to 70% at 1.23 V after the deposition of Co_3O_4 , supporting the enhanced charge injection from photoanodes to water. In addition to studying the effect of passivation layer, the hole scavenger was also used to compare the extent of surface/bulk recombination in photoelectrodes prepared from different synthesis methods. For instance, Dotan *et al.* reported that hematite photoanodes prepared via ultrasonic spray pyrolysis (USP) and APCVD showed different water oxidation performance.⁹² With the help of H_2O_2 as the hole scavenger, higher values of η_{sep} and η_{inj} for water oxidation were obtained for hematite synthesized by APCVD, indicating less bulk and surface recombination as well as better performance.

Using scavengers is a convenient yet powerful tool to understand the charge transfer behaviours in photoelectrodes. However, it also features some limitations. For instance, the η_{inj} derived here only represents the overall charge transfer from photoelectrodes to the electrolyte. It is hard to distinguish whether the change of η_{inj} is due to the change of reaction kinetics or surface charge recombination, especially when some passivation layers and catalysts are present. In addition, it is

critical to choose suitable scavengers in order to obtain reasonable values of η_{inj} . For instance, Gao *et al.* found that the η_{inj} of $CuWO_4$ photoanodes for water oxidation was underestimated when H_2O_2 was used as the hole scavenger.⁹⁴ The reason was the electron injection from the radical intermediate of H_2O_2 oxidation to the conduction band of $CuWO_4$, which made the expected 2-hole process becoming 1-hole process and led to current multiplications. Overall, more details about charge transfer behaviours can be revealed when more characterization tools such as photoelectrochemical impedance spectroscopy, intensity modulated photocurrent spectroscopy and so on are combined. More study about other techniques will be presented in section 5.1.

3.3.2 Passivation layers

The most straightforward strategy may be to deposit a passivation layer on the surface of semiconductor. For instance, thin layer of metal oxides including Al_2O_3 , In_2O_3 and Ga_2O_3 has been deposited on ultrathin hematite (27-30 nm) photoanode via a urea hydrolysis CBD method.⁹⁵ The idea was to replace the hematite|water interface with a hematite|oxide|water one. By doing so, researchers expect to reduce surface recombination unique to the hematite|water interface. The most direct evidence has been the reduction of Fermi level pinning effect due to surface states, which is manifested by the increase of the photovoltage and, hence, a reduction of the turn-on potentials. Among those tested, Ga_2O_3 has proven highly effective, which negatively shifted the turn-on potential by 400 mV. The improvement was attributed to the matching crystal structures between Ga_2O_3 and hematite (<2.5% mismatch), resulting in low strains at the interface.

As will be further discussed later in this Review, the role played by the so-called "passivation layer" can be complex. A simple reduction in the turn-on potentials may be explained by at least three distinct mechanisms, including better catalysis, greater photovoltage or reduced recombination. These three mechanisms themselves are intricately interconnected, as well. For instance, better catalysis generally means faster forward charge transfer and, hence, reduced recombination; greater photovoltage implies better charge separation, which is typically a result of lower recombination. For this portion of discussions, we define these different functionalities as follows. When the surface modification forms a buried junction with the photoelectrode to yield better charge separation, we regard it as mainly improving the photovoltage; when the surface layer chiefly removes surface states to reduce recombination, we consider it a passivation layer; when the surface materials speed up forward electron transfer, we treat it as a catalyst. Within this context, effective catalysts have been widely exploited to improve the performance of photoelectrodes, especially for the sluggish water oxidation reactions. For example, dual-layered $FeOOH/NiOOH$ was deposited on mesoporous $BiVO_4$ surface by photo-assisted electrodeposition in sequence.³² When $BiVO_4$ decorated with dual-layered catalysts was compared with the bare one and the one with only $FeOOH$ or $NiOOH$, in terms of the performance for water oxidation and sulfite oxidation, the one with dual-layered catalysts showed the earliest turn-on potentials and the highest

water oxidation photocurrent densities. The effectiveness of combining FeOOH and NiOOH was attributed to the better interface formed between BiVO₄ and FeOOH to reduce charge recombination, as well as more negative potential drop within the Helmholtz layer at the NiOOH/electrolyte interface (for more negative turn-on potentials) and better water oxidation kinetics. More examples will be discussed in the section 5 and the role of catalysts on semiconductor surfaces will be discussed in greater detail there.

Overall, using passivation layers to reduce surface recombination has been widely applied to improve the performance of photoelectrodes. Such a strategy offers a variety of materials choices to serve as passivation layers, which makes it versatile for different types of study platforms. In addition, the deposition of passivation layer may also shed light on solving other limitations of photoelectrodes. For instance, metal oxides passivation layers can also serve as protective layers to enhance the stability. Catalytic passivation layer, on the other hand, may improve the kinetics of desired reactions. At the same time, however, it also requires deep understanding for the origins of surface recombination in order to choose suitable passivation layer. In addition, the deposition of extra layer on semiconductors may have the chance to introduce unexpected interfacial states, affecting charge transfer behaviours.

3.3.3 Surface reconstruction

Another strategy to deal with surface recombination is to change the crystal structure at the surface. For instance, Jang *et al.* reported a regrowth method to improve the performance of bare hematite.²² By repeating the solution-based synthesis of FeOOH and post-annealing procedures in air, the authors found the photovoltage generated by bare hematite photoelectrode could be increased by 27%. During the regrowth, the surface structures of hematite were dissolved, and the newly grown structures favor the <110> directions, which reduced the short-range structure disorder on the surface (Figure 9a). In another study, NaBH₄ was used as the H₂ source to treat the hydrothermally synthesized hematite at 500 °C.⁴⁸ Such a treatment mainly introduced oxygen vacancies on the surface of hematite, which was supported by the decrease of prepeak intensities in the surface-sensitive soft X-ray O K-edge XAS spectra in combination with the unchanged peak intensities in the bulk-sensitive hard X-ray Fe K-edge XAS spectra. The authors argued that the optimized oxygen vacancy content on the surface improved the conductivity of hematite and reduced the hole-electron recombination. As a result, the photocurrent density at 1.23 V increased from 0.88 mA/cm² for pristine hematite to 2.28 mA/cm² for the H₂-treated hematite.

As is true in other complex systems, changes intended for the improvement of one aspect of the system may inadvertently impact another aspect negatively. For instance, increasing oxygen vacancies could be an effective strategy to increase carrier concentrations in WO₃ (e.g., Section 3.2.2), but they may also induce surface recombination. In an effort to achieve the positive effect of oxygen vacancies while minimizing its negative impacts, Zhang *et al.* reported a synthesis procedure combining H₂ annealing and O₃ treatment, in which case H₂ annealing was

shown to increase oxygen vacancies in the bulk of WO₃ while the subsequent O₃ treatment decreased oxygen vacancies on the surface (Figure 9c-e).⁷² The Mott-Schottky analysis supported the increase of donor densities after H₂ treatments, which remained after O₃ treatment. The lowest peak intensities in photoluminescence spectra for H₂/O₃ treated samples indicated effective suppression of surface charge recombination, supporting the effect of reducing surface oxygen vacancies. As a result, the H₂/O₃ treated photoelectrode showed a cathodic shift of turn-on potential (0.15 V) and increased photocurrent densities at 1.23 V in comparison to the samples that were just treated by H₂.

Compared with depositing passivation layer to reduce surface recombination, surface reconstruction avoids the formation of additional interface, lowering the risk of generating more interfacial defects. However, such a strategy is material-specific and the knowledge obtained from one case study needs to be justified before being transferred to other study platforms.

3.4 Mismatch of energetics

For successful solar-to-chemical conversion reactions, it is of critical importance to match the energetics of the photoelectrode with the desired chemical reactions. In the case of significant mismatches, the photo-generated charges

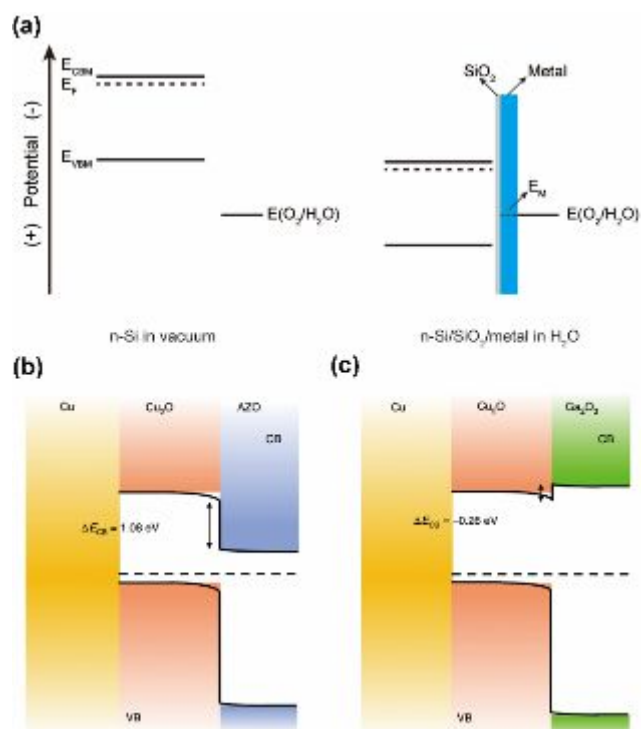


Figure 10 (a) The schematic shows the band edge positions of n-Si in the vacuum before in contact with H₂O (left) and n-Si/SiO₂/metal in contact with H₂O (right). $E(\text{O}_2/\text{H}_2\text{O})$: water oxidation potential; E_{M} : work function of the metal; $E_{\text{CB}}/E_{\text{VB}}$: the conduction band minimum/valence band maximum positions; E_{F} : Fermi level. Equilibrium band-edge diagrams of Cu₂O/AZO (Al doped ZnO) (b) and Cu₂O/Ga₂O₃ (c) heterojunctions with different conduction band edge discontinuity (ΔE_{CB}). (c) and (d) reproduced from ref. 30 with permission from Springer Nature.

collected from the photoelectrode would not be energetic enough to drive the chemistry in the electrolyte. For instance, while CdSe is efficient in absorbing light and separating charges, photo-generated holes in this material would feature electronic energies too negative for H₂O oxidation.⁹⁶ As such, we do not see examples of using this material for H₂O oxidation applications. Instead, sacrificial electron donors are often involved when CdSe is studied in the context of solar fuel synthesis. A more common issue we encounter in the literature that concerns energetic mismatch is the relatively low photovoltages. Si is a good example. In vacuum, the potential of valence band maximum (E_{VB}) of Si would be too negative for H₂O oxidation; yet, due to the existence and/or formation of native oxides on the surface, Si photoanodes have been successfully used for PEC H₂O oxidation, albeit with a low photovoltage as featured by the late turn-on potentials (Figure 10a).⁹⁷ Two general strategies have been tested to address this issue, forming buried junctions or tuning the band edge positions.

3.4.1 Forming buried junctions

The flat-band potential of Cu₂O has been reported at around 0.7 V, which limits the maximum photovoltage when used for H₂O

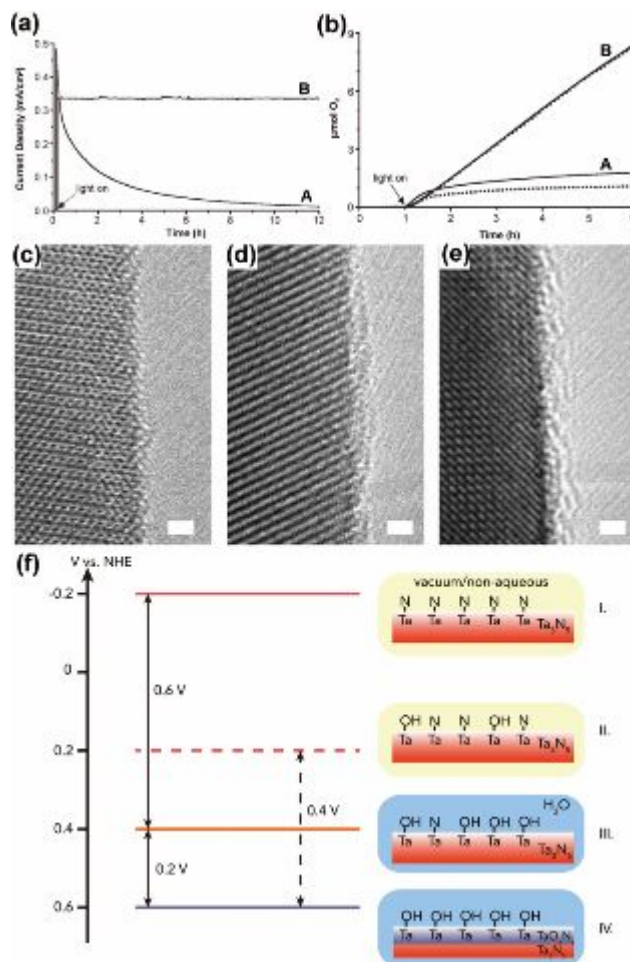


Figure 11 (a) Photocurrent density vs. time curves of bare WO₃ (A) and WO₃ with Co-Pi (B) at 0.8 V vs. Ag/AgCl in 0.1 M phosphate buffer (pH 7) under AM 1.5 G illumination. (b) O₂ amount detected by a fluorescence-based sensor (dotted lines) and calculated from passing charges (solid lines) for bare WO₃ (A) and WO₃ with Co-Pi (B) at 0.8 V vs. Ag/AgCl under 400 mW/cm² light intensity. (c)–(e) are the HRTEM images of as-prepared Ta₃N₅ (c), Ta₃N₅ after 1 CV in 1 M NaOH (d) and Ta₃N₅ after 3 hr of photoelectrolysis at 0 V in 1 M NaOH (e). The scale bar is 1 nm. (f) The schematic shows the evolution of Ta₃N₅ surface energetics in different stages. The horizontal lines represented the Fermi level of Ta₃N₅ in different stages. Stage I: fresh Ta₃N₅ free of H₂O; Stage II: Ta₃N₅ with partial H₂O adsorption after exposed to air; Stage III: Ta₃N₅ in H₂O; Stage IV: Ta₃N₅ with surface oxidation. (a–b) reprinted with permission from ref. 75. Copyright 2011 American Chemical Society. (c–f) reproduced from ref. 69 with permission from Elsevier.

reduction. In order to address this issue, buried p-n junction has been applied to enhance the photovoltage. One example is to replace the Cu₂O/H₂O interface with a Cu₂O/ZnS interface.⁴⁹ Due to the more negative conduction band edge position and the more negative Fermi level of ZnS relative to the HER potential, the strategy increased the band bending within Cu₂O for a turn-on potential of 0.72 V; by comparison, Cu₂O without ZnS showed a V_{on} of only 0.6 V in 0.2 M KH₂PO₄ at pH 7. The increased photovoltage was confirmed by the light open-circuit potential measurements under various light intensities. Another example is reported by Li *et al.*, in which the authors deposited a thin layer of Ga₂O₃ buffer between Cu₂O and TiO₂ (as a protection layer) by ALD.⁴⁵ The idea was to maximize band bending within Cu₂O by introducing Ga₂O₃. Through photoelectron spectroscopy measurements, they found the

conduction band offset between Cu_2O and Ga_2O_3 was in the range of -0.37 to $+0.01$ eV, suggesting that in addition to a large degree of band bending, electron transfer across the Ga_2O_3 layer should be facilitated. A stark comparison could be made between Ga_2O_3 and ZnO , which would also serve the purpose of increasing band bending when integrated with Cu_2O . But ZnO features a significant mismatch with Cu_2O in terms of potential of conduction band minimum (E_{CB}), which would impede electron transfer from Cu_2O to ZnO . As such, ZnO is much less desired for the same purpose (Figure 10b and 10c). Indeed, a turn-on potential of 1.02 V was achieved for the integrated $\text{Cu}_2\text{O}|\text{Ga}_2\text{O}_3|\text{TiO}_2$ photoelectrode in 0.5 M Na_2SO_4 buffered at pH 4.26. Pan *et al.* further advanced this strategy by integrating nanowire nanostructuring, a Ga_2O_3 buffer layer, a TiO_2 protection layer and RuO_x as HER catalysts.³⁰ Together, a turn-on potential >1 V and a photocurrent density of -10 mA/cm² at 0 V, as well as stability over 100 h were obtained at pH 5.

Using a similar strategy on a different material, Digdaya *et al.* improved the performance of amorphous SiC .⁶³ They deposited a thin layer (25 nm) of $n\text{-TiO}_2$ on $a\text{-SiC}$ (100 nm) by ALD, replacing the original semiconductor/liquid electrolyte interface with a $p\text{-i-n}$ solid junction. Under illumination, photo-generated holes would drift to the p -type amorphous SiC layer and electrons to the n -type TiO_2 . Due to the formation of a buried junction, the photovoltage was increased by 300 mV. After the electrodeposition of active HER catalysts, Ni-Mo , the integrated thin-film photocathode achieved a turn-on potential of 0.8 V and a photocurrent density of -8.3 mA/cm² at 0 V in pH 4 phosphate buffer. In addition to forming a buried junction, the TiO_2 layer also enhanced the adhesion of the catalysts to the surface, leading to stable HER operation for 12 h.

In addition to aforementioned examples, forming buried junction has been applied in various semiconductor materials such as Si , III-V compounds, etc., which has been shown as an effective way to improve the photovoltage output. However, some challenges still need to be addressed in this process, such as how to create defect-free interface and how to achieve uniformly deposition on high-aspect-ratio substrates, etc.

3.4.2 Tuning band edge positions

Although Si features high photocurrent density as photoelectrodes, its photovoltage has been limited. When it was used as a photocathode, the photovoltage has been limited to 400 mV without additional buried junctions. As a photoanode, theoretically it cannot oxidize water due to the negative position of the E_{VB} . The issue has been shown to be partially addressable by strategies such as forming a metal-insulator-semiconductor interface (e.g., $\text{Ni-SiO}_2\text{-Si}$), where high photocurrent density was measured. But the turn-on potential was still relatively positive (1 V), representing a photovoltage of only 0.23 V.⁹⁸ To further address this problem, amorphous silicon has been developed. Hydrogenated amorphous silicon has a continuously random bonding network, resulting in a relatively large band gap (1.7 eV) and more positive E_{VB} for improved photovoltage and better alignment with water oxidation energy levels. Additionally, $a\text{-Si}$ has been shown to be a much more efficient light absorber due to the direct nature of the band gap. Importantly, knowledge of semiconductor thin

film growth makes it facile to control the doping type and level of $a\text{-Si}$ with ease, making it possible to utilize it for both oxidation and reduction reactions readily. To this end, Lin *et al.* reported $a\text{-Si}$ with a buried $p\text{-i-n}$ structure.¹⁶ Using a glass substrate decorated with 1.8 μm thick pyramidally textured ZnO , 250 nm intrinsic $a\text{-Si}$ (active light absorber) were sandwiched between thin layers of p -type and n -type nanocrystalline silicon via plasma-enhanced CVD. After further decoration of a TiO_2 protection layer and Pt HER catalysts, the photocathode showed a turn-on potential of 0.93 V and a photocurrent density of 11.6 mA/cm² at 0 V in pH 4 phosphate buffer under 1 sun illumination. The reported turn-on potential was even more positive than what was obtained on $n^+p\text{-Si}$ (usually limited to 0.54 V).

Compared with forming buried junctions, tuning the band edge positions of semiconductors to solve the mismatch of energetics can avoid the risk of forming interfacial defects between different layers. However, only a handful of materials can be modified using such a method, which limits its applications.

3.5 Instability

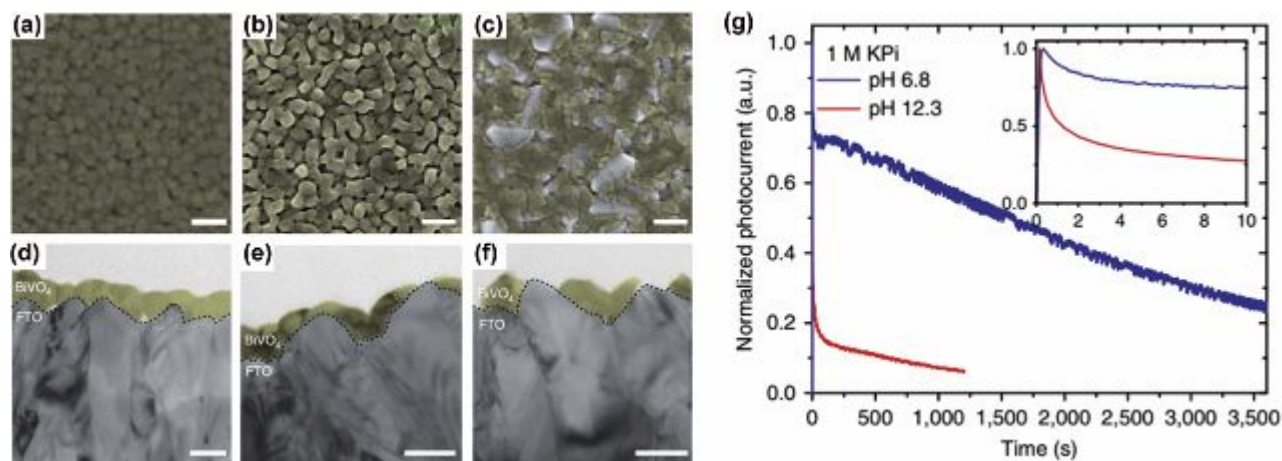


Figure 12 The SEM images (a-c, scale bar 500 nm) and cross-sectional TEM images (d-f, scale bar 100 nm) of BiVO_4 thin films on FTO. (a, d) Pristine BiVO_4 ; (b, e) BiVO_4 degraded at pH 6.8 electrolyte; (c, f) BiVO_4 degraded at pH 12.3 electrolyte. (g) The photocurrent profile of BiVO_4 in phosphate buffer at pH 6.8 and pH 12.3 at 1.23 V. (a-g) reproduced from ref. 101 with permission from Springer Nature.

Among the issues discussed in this section, instability of photoelectrodes is arguably the most unique to photoelectrochemical applications. Concerns such as narrow light absorption, bulk and surface recombination and charge transport are shared by other semiconductor-based applications. But instability defines photoelectrochemical systems because only for this application does one need to subject a semiconductor material to harsh conditions – intense illumination plus extreme pH environments with high salt concentrations. Broadly speaking, we refer to instability as the rapid degradation of the photoelectrode performance. The phenomenon may be attributed to at least three distinctly different causes: 1. The deactivation of the active sites by mechanisms such as accumulation of by-products; here little change to the photoelectrode itself occurs; 2. The deactivation of the photoelectrode due to the loss of photovoltages, where the photoelectrode loses or gains little in a physical sense; 3. Significant changes to the photoelectrode due to corrosion during the chemical and/or photoelectrochemical reactions.

3.5.1 The accumulation of byproducts due to parasitic chemical reactions

It has been shown that the formation and accumulation of peroxy species on WO_3 surfaces during water oxidation may lead to the loss of photoactivities.⁹⁹ The mechanism is to be differentiated from corrosion, which is well known for WO_3 at higher pH (e.g., >4) due to the loosely bound $\text{WO}_3(\text{H}_2\text{O})_x$ species on the surface.¹⁰⁰ How to suppress the side reaction will be the key to reactivate the photoelectrode. Seabold *et al.* reported that the deposition of Co-Pi on WO_3 improved the photocurrent to O_2 conversion efficiency from 61% to 100%.⁷⁵ At the same time, the WO_3 was shown to be stable under water oxidation condition for 12 h after the deposition of Co-Pi in pH 7 phosphate buffer, while the bare one lost 63% of its initial photocurrent density within 1 h (Figure 11a and b). Other than introducing OER catalysts, Ma *et al.* used a solution-based reducing reagent, LEDA (lithium dissolved in ethylenediamine), to create an amorphous overlayer on mesoporous WO_3 photoanode.²³ Consisted of both oxygen vacancies and tungsten vacancies, such an amorphous layer improved charge

transfer efficiency, reducing the formation of peroxide species due to hole accumulation. As a result, both the photocurrent density/turn-on potential and the stability were improved. In a different approach, Wang *et al.* tailored the orientation of exposed facets during the hydrothermal growth of WO_3 .⁷⁴ With increased (002) facets as opposed to (200) facets in WO_3 , the photocurrent density at 1.23 V was improved from 2.1 mA/cm^2 to 3.1 mA/cm^2 , with the stability also enhanced. Such a result was attributed to the reduced electron-hole recombination and inhibited peroxy-species on (002) facets.

3.5.2 Deactivation of the photoelectrode due to loss of photovoltages

It has been commonly observed that the performance of Ta₃N₅ quickly decayed during water oxidation, which was generally attributed to the oxidation of nitrides. Indeed, nitride oxidation was observed after water oxidation, confirming the formation of oxides. However, it was unclear how the surface oxidation was related to the performance decay. Another puzzle about Ta₃N₅ is the positive turn-on potentials for water oxidation (>0.6 V), which is significantly higher than what one would expect from the material based on measurements of the band edge positions and Fermi levels in vacuum. He et al. reported a detailed study on the detailed changes on the surface of Ta₃N₅ during water oxidation using a combination of photoelectrochemical methods, high-resolution electron microscopy and X-ray core-level spectroscopy (Figure 11c-f).⁶⁹ It was found that the oxidation of Ta₃N₅ nanotubes to tantalum oxide was self-limited on the surface during water oxidation, leading to the formation of a relatively thin amorphous oxide layer (~ 3 nm). The surface oxidation process not only introduced increased charge transfer resistance, but also shifted the Fermi level positively by 200 mV, leading to significant Fermi-level pinning that greatly limits the measurable photovoltages. Moreover, chemisorption of H₂O onto Ta₃N₅ alone was found to introduce an additional positive shift of the flat-band potential by nearly 600 mV. This shift explains why most reports on Ta₃N₅ only observed highly positive turn-on potentials when characterizing the material in water. By comparison, a much less positive potential could be measured in nonaqueous systems, such as acetonitrile. The results imply that even though surface oxidation is relatively mild when measured by thickness, the reaction could suppress the achievable performance of nitrides by a large margin.

3.5.3 Corrosion

BiVO₄ in near-neutral and alkaline solution is known to be susceptible to chemical and photochemical corrosion, although thermodynamically it is expected to be stable. Toma *et al.* studied the instability of polycrystalline BiVO₄ using various methods, including SEM, TEM, Rutherford backscattering spectrometry (RBS), *in-situ* electrochemical AFM, ICP-MS and computational prediction.¹⁰¹ It was found that the V in BiVO₄ dissolved in the electrolyte. Thermodynamically, a self-passivation process should take place via the formation of a chemically stable bismuth oxide on BiVO₄ surface. However, such a process is kinetically hindered at room temperature in aqueous solutions, leading to the formation of defective and unstable bismuth oxide or hydroxide. As a result, bulk dissolution of BiVO₄ occurs, which would be accelerated by illumination, increased pH and/or applied bias. It was hypothesized that the photo-induced chemical instability may be a result of the accumulation of holes on the surface and the formation of reactive oxygen species, which could oxidize Bi³⁺ to Bi⁵⁺ or oxidize O²⁻ to O[·]. To address the instability issue, one common strategy was to protection layer to avoid the contact between BiVO₄ and H₂O, and introduce the OER catalyst to guide the hole transfer for water oxidation instead of self-oxidation. Another class of materials that have been intensely studied for their corrosion problems are high-efficiency phosphides and/or arsenides.

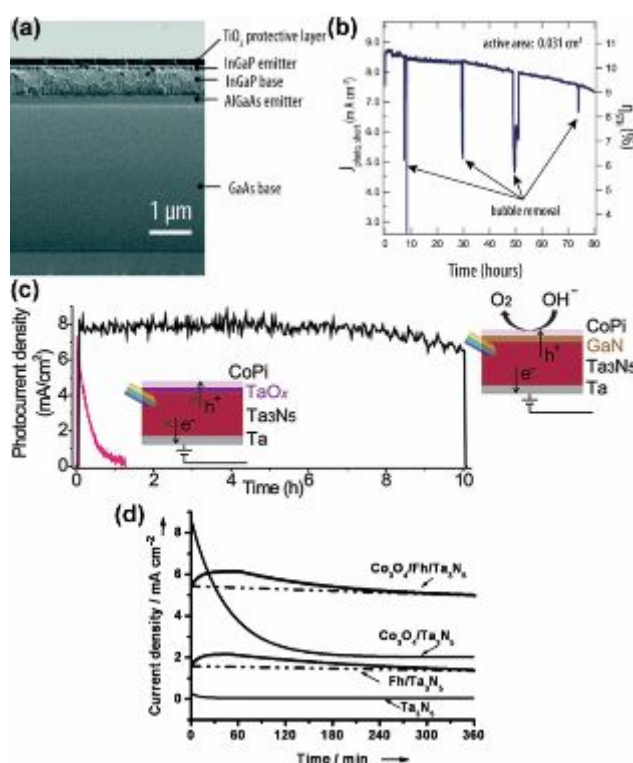


Figure 13 (a) Cross-sectional SEM image of a GaAs/InGaP/TiO₂/Ni photoelectrode. (b) The short-circuit photocurrent density ($J_{\text{photo, short}}$) and the corresponding solar-to-hydrogen conversion efficiency (η_{STH}) vs. the testing time when the photoelectrode shown in (a) was in connect with a Ni-Mo cathode in 1.0 M KOH electrolyte under 1 sun illumination. (c) The photocurrent density vs. time curves for Ta₃N₅ coated with CoPi (pink) and Ta₃N₅ coated with GaN and CoPi (black) at 1.2 V in 0.5 M KPI electrolyte (pH 13) under AM 1.5G illumination. (d) The photocurrent density vs. time curves for bare Ta₃N₅, Ta₃N₅ coated with ferrihydrite (Fh) layers (Fh/Ta₃N₅), Ta₃N₅ coated with Co₃O₄ nanoparticles (Co₃O₄/Ta₃N₅) and Ta₃N₅ coated with both Fh layers and Co₃O₄ nanoparticles (Co₃O₄/Fh/Ta₃N₅) in 1 M NaOH at 1.23 V under AM 1.5G illumination. (a-b) reproduced from Ref. 54 with permission from the Royal Society of Chemistry. (c) reproduced from ref. 8 with permission from John Wiley & Sons. (d) reproduced from ref. 25 with permission from John Wiley & Sons.

More details will be discussed next in the strategies on how to protect them.

3.5.4 Protection strategies

One common strategy to protect unstable materials is to conceal the reactive surface altogether by one or multiple protection layers. Stable oxide materials (e.g., TiO₂) have been used to serve this purpose. The key here is to achieve uniform and compact deposition of protective materials with appropriate thicknesses, so that the contact between the electrolyte and the semiconductor can be separated to prevent corrosion, yet efficient charge transfer across the protection is ensured. Due to the lack of inherent catalytic activities on such protection layers, catalysts are often required. In addition, one should manage light absorption so that the protection layer does not compete with the active material in absorbing in the visible range. For the ease of discussions, we summarize materials studied for the purpose of protection based on their types below.

Catalytically-inactive oxide/nitride materials

Metal oxides with wide band gaps have been studied extensively as a protection layer for both photocathodes and photoanodes. TiO_2 is one of the most representative examples for this purpose, which has been applied to various photoelectrode materials including Si,^{10, 16, 97} III-V semiconductors,^{54, 56, 57, 97} unstable metal oxides (Cu_2O ,^{19, 30, 44, 46} BiVO_4 ,²⁰ etc.) and metal chalcogenides (CZTS,²⁴ etc.). For instance, TiO_2 has been reported to serve as a protective material on various photocathodes. Gu *et al.* reported a bilayer protection of GaInP_2 photocathode by amorphous TiO_x and MoS_x ,⁵⁷ which were deposited by ALD and electrochemical deposition, respectively. Further annealing in Ar atmosphere at 450 °C improved the crystallinity of MoS_2 and TiO_2 , as well as forming a hybrid interface between MoS_2 and TiO_2 in the form of $\text{MoS}_x/\text{MoO}_y\text{O}_z/\text{MoO}_x/\text{TiO}_2$. Compared with the as-deposited photoelectrode, the annealed one showed not only better fill factors but also enhanced stability. After 20 h photoelectrolysis at 0 V in 0.5 M H_2SO_4 , the photocurrent density of the as-deposited one decreased from 10 mA/cm^2 to 5 mA/cm^2 , while the annealed one only decreased by less than 20%. In terms of using TiO_2 to protect photoanodes, Verlage *et al.* synthesized III-V tandem cells using MOCVD on n⁺-GaAs (100).⁵⁴ The tandem light absorber consisted of an InGaP top cell ($E_g=1.84$ eV, 550 nm) and a GaAs bottom cell ($E_g=1.42$ eV, 3200 nm), connected by an AlGaAs/GaAs tunnel junction (40 nm). An amorphous, hole-conducting TiO_2 layer (62.5 nm) was deposited on the light absorber surface by ALD to prevent photocorrosion as well as serving as an anti-reflection coating, with additional 2 nm Ni as the OER catalysts (Figure 13a). When connected to a Ni-Mo cathode in 1 M KOH electrolyte, the device was shown to split water without external bias at a current density of 8.5 mA/cm^2 under 1 sun illumination, which decreased to 7.3 mA/cm^2 after 80 h operations (Figure 13b). Similar protection layer/catalyst combinations have been shown effective in protecting photoanodes of a variety compositions, including Si, GaP, GaAs and BiVO_4 .⁹⁷

Oxide materials as a protection layer face limitations when directly applied to nitride semiconductors (e.g., Ta_3N_5), which are often sensitive to oxidative conditions. To address this issue, Zhong *et al.* reported a GaN-protected Ta_3N_5 photoanode.⁸ In this study, GaN (50 nm) was synthesized by e-beam evaporation and subsequent nitridation. With Co-Pi as the OER catalysts, the protected photoanode showed a turn-on potential of 0.65 V and a photocurrent density of 8 mA/cm^2 at 1.23 V in 0.5 M phosphate buffer (pH 13). Importantly, it achieved stable water oxidation at 1.2 V for 10 h (Figure 13c). Control samples of Ta_3N_5 without GaN quickly decayed within 1 h, due to the formation of surface oxides (also see Section 3.5.2).

Catalytically-active materials

Another strategy to protect the photoactive material is to minimize parasitic chemical reactions such as corrosion by speeding up the desired chemical reactions. That is, using catalysts to facilitate charge transfer for desired solar fuel synthesis may be regarded as a good strategy for protection purposes. For water oxidation, transition metal oxide/hydroxides (e.g., CoO_x ,^{25, 62} $\text{Co}(\text{OH})_2$,^{26, 70} $\text{Ni}(\text{OH})_2$,^{21, 68, 102}

NiFe-LDH ,²⁷ etc.) have been commonly used. For water reduction, precious metal catalysts (e.g., Pt^{19, 47, 103}) or non-noble-metal catalysts (e.g., MoS_2 ^{57, 104}) are usually applied. For example, efficient electrocatalysts such as Pt and MoS_2 have been shown to stabilize high-performance photocathodes. MoS_2 has been used to protect GaInP_2 , as reported by Britto *et al.*¹⁰⁴ Thin-film GaInP_2 (~200 nm) was coated by a thin layer (3.6 nm) of Mo metal, which was partially converted to MoS_2 through sulfurization. In a sulfuric acid electrolyte (cc. 3 M), bare GaInP_2 showed quick performance decay (within minutes) and complete failure after several hours due to dissolution. In stark contrast, GaInP_2 coated with Mo/ MoS_2 showed enhanced turn-on potentials during the initial test (presumably due to more exposed edge sites of MoS_2) and stable HER performance for 60 h. Along this line, Kumagai *et al.* reported that the performance of CIGS photocathode could be improved significantly by adding a thin layer of Ti/Mo between CIGS/CdS and Pt.⁷ The authors attributed the phenomenon to better electron transfer from CIGS/CdS to Pt. The stability of the integrated photocathode was improved to 10 days.

It is important to note that the protection effect by similar materials is apparent as long as efficient charge extraction from the semiconductors is achieved. For instance, Liu *et al.* reported a hydrothermally-deposited ferrihydrite layer on Ta_3N_5 , when coupled with Co_3O_4 OER catalysts, could significantly improve the stability of the latter to up to 6 h (Figure 13d and 13e).²⁵ As a comparison, Ta_3N_5 with only Co_3O_4 showed 70% of decay within 2 h. The role of the ferrihydrite was revealed as a storage layer for photogenerated holes in the form of positively charge states. Besides the ferrihydrite, the combination of $\text{Ni}(\text{OH})_x$ and MoO_3 was shown to work well as a hole storage layer for the protection of Ta_3N_5 .¹⁰² When used alone on Ta_3N_5 , the $\text{Ni}(\text{OH})_x/\text{MoO}_3$ layer featured low charge injection efficiency (<15%) and, therefore, is an inefficient OER catalyst.

Overall, protective layers have become a critical component for high-efficiency but unstable semiconductor materials. Numerous research efforts have been devoted to this research direction, and various types of protective materials have been reported, providing a rich knowledge base for its applications in different study platforms.

Other strategies

In addition to depositing protection materials, modifying the photoelectrode|electrolyte interface by strategies such as changing the structures of the semiconductors or altering the compositions of the electrolyte has been reported as effective in addressing the instability issues. To this end, Kuang *et al.* reported that the crystallinity of BiVO_4 nanoparticles was enhanced after a two-step high temperature annealing treatment (800°C-ball milling-700°C).⁴¹ These nanoparticles exhibited inherently better stability against photocorrosion in comparison to nanoworm BiVO_4 , which was obtained by annealing at 450°C. With the introduction of self-generation and regeneration of NiFe-based OER catalysts, the stability was further extended to >1000 h. In terms of surface modifications, by tuning the exposed surface of single crystalline GaN to be N-terminated, Kibria *et al.* found that MBE-grown GaN showed better photostability than the ones grown by conventional

MOCVD, whose Ga-terminated surfaces could be easily oxidized to Ga₂O₃ in the presence of oxygen/H₂O and dissolved in the electrolyte, leading to the photocorrosion as well as Fermi level pinning.⁷⁹ Moreover, since the loss of V⁵⁺ was involved in the photocorrosion of BiVO₄, Lee *et al.* introduced a V⁵⁺-saturated 1 M borate buffer (pH 9.3) for water oxidation test.³⁹ Based on the Le Châtelier principle, the dissolution of V⁵⁺ was hindered. As a result, the stability of the BiVO₄ photoelectrode was improved. With additional decorations of FeOOH/NiOOH OER catalysts, the stability of BiVO₄ in the V⁵⁺-saturated electrolyte was extended to 500 h.

Compared with the deposition of protective layers, the aforementioned strategies reduced the decoration materials on semiconductors, simplifying the photoelectrode configurations. However, the broad applications of these strategies beyond the case studies remain to be seen.

3.6 Other issues

3.6.1 High fabrication cost

In addition to materials cost, the fabrication process itself could incur significant cost. In general, the cost concern limits the scale of implementation for many high-performance materials, especially III-V semiconductors (e.g., GaAs, InGaP, etc.). Many strategies developed to reduce costs of solar cells are expected to be transferrable to solar fuel synthesis, as well. For example, while effective in synthesizing high quality semiconductor thin films, MOCVD tends to be an expensive process. An even more expensive part, however, comes from the usage of single-crystalline III-V substrates for epitaxial growth of solar cell-grade materials. To address this problem, researchers have optimized the synthesis so that the expensive substrates may be recycled for repeated growths. Moreover, other less expensive synthesis methods have been explored to replace the MOCVD, which has been reviewed elsewhere¹⁰⁵. Similar arguments are equally applicable to MBE processes.¹⁰⁶

As an example of transferring knowledge learned in research on photovoltaics to solar fuel applications, Kang *et al.* fabricated

GaAs/Al_xGa_{1-x}As based photocathodes and photoanodes using epitaxial lift-off and printing-based assemblies (Figure 14).¹¹ During the synthesis, a p-on-n or n-on-p epitaxial GaAs solar cells were first grown on a GaAs wafer, which were later lifted off and printed on glass substrates. Pt and IrO_x • nH₂O was deposited to serve as the water reduction and oxidation catalysts, respectively. Such a design allows the reuse of expensive growth wafer, offering a significant reduction of material costs. Similarly, Young *et al.* reported the synthesis of inverted metamorphic multi-junctions for water splitting.⁵⁵ The growth substrate (GaAs) was ca. 100 times thicker than the active light absorbers, which would be a significant waste of expensive materials. A selective chemical etching process was introduced to remove the GaAs substrate after the device was bonded to a flat, rigid Si wafer as a handle. As a result, the expensive GaAs substrate could be reused for the next growth.

3.6.2 Charge recombination at semiconductor/substrate interface

As discussed in Sections 3.2 and 3.3, charge recombination in the bulk or near the surface can lead to decreased charge collection efficiency. In another case, charge recombination can take place at the semiconductor/substrate interface. For example, the formation of a “dead layer” at the hematite-substrate interface, especially in ultrathin film (with thickness < 50 nm), was believed as the result of lattice strains between hematite and the substrate (usually FTO), which would lead to imperfect crystal structures near the interface and induce charge recombination.¹⁰⁷ Hisatomi *et al.* reported a thin layer of Ga₂O₃ (2 nm) between the FTO substrate and hematite can serve as an isomorphic structure template for the growth of ultrathin hematite (27 nm) due to their similar crystal structures. After the FTO substrate was modified with Ga₂O₃, the crystallinity of hematite was improved based on the increased peak intensity observed in XRD. As a consequence, the turn-on potential was cathodically shifted by 200 mV and the photocurrent density at 1.23 V was improved by 15 times.⁹⁵ Zandi *et al.* used ALD to synthesize Ti-doped hematite by tuning the numbers of Ti precursor (titanium isopropoxide) pulses and Fe precursor (ferrocene) pulses during the ALD process.¹⁰⁸ Although Ti⁴⁺ has been reported to serve as the dopant to improve the donor density in hematite, the introduction of Ti in this study showed no effect on carrier concentration. Instead, the bulk properties were improved with hole mobility and/or the hole lifetime enhanced after the introduction of Ti, which was due to the elimination of dead layer. In addition, EIS analysis indicated a higher density of active sites for water oxidation was achieved after the Ti doping.

4 Thin film protection layer

Thin-film protection materials for photoelectrodes have been recently reviewed in detail.^{4,5} Here we briefly summarize those thin-film protection materials based on their method of protection. One method protects the semiconductor by isolating the unstable surface from the aqueous electrolyte, which inhibits the photoelectrochemical or chemical dissolution of the semiconductor. We refer to this protection method as a physical barrier layer. The other method inhibits

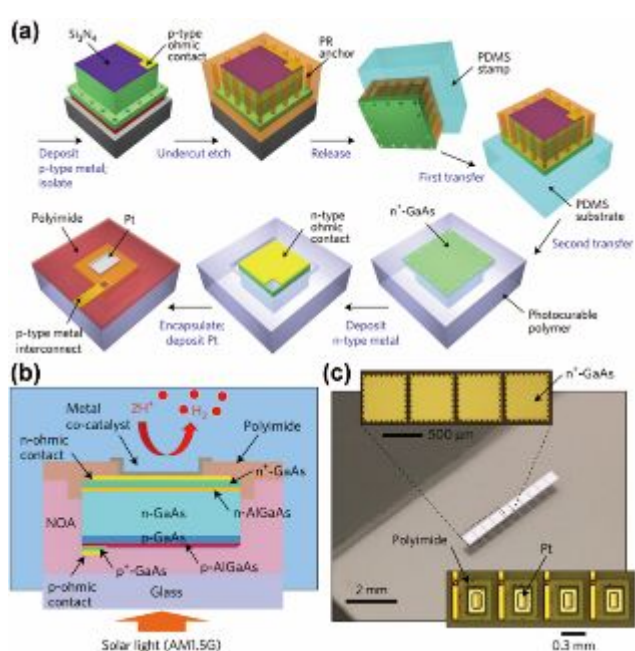


Figure 14 (a) The schematic shows the fabrication process for integrated GaAs photocathodes printed on a glass substrate. (b) The schematic shows the cross-sectional view of the integrated GaAs photocathode, where the photocurable polymer (NOA) was used as the transparent printing medium. (c) The photograph showed the exposed n⁺-GaAs after the printing-based assemblies. The insets showed the magnified view of photoelectrode surfaces. (a-c) reproduced from ref. 11 with permission from Springer Nature.

photocorrosion of semiconductors by selectively tuning the pathway of photogenerated charge carriers to the desired chemical reactions opposed to the corrosion. Since this method of protection relies on optimizing relative rates of reactions, we refer to it as a kinetic protection layer. Some examples of thin-film protection layers have been discussed in section 3.5.4.

4.1 Physical barrier protection layer

In order to fully isolate the unstable semiconductors from the aqueous electrolyte, the protection layers are required to be ion-impermeable and pin-hole free. Therefore, deposition techniques that feature uniform coating of dense material, such as PVD and CVD, are usually applied to deposit the films. On the other hand, since this type of materials is catalytic non-active, it's important to control its thickness to be thin and conductive so that the photo-generated charge carriers can be transferred to the catalyst/electrolyte.

Metal thin films such as Ti¹⁰⁹ or Pd¹¹⁰, have been demonstrated to protect crystalline Si photocathodes and photoanodes. The metals can form Schottky-junctions with semiconductors and serve as conductive layers, and the photogenerated electrons or holes can be separated and transferred to solution. One limitation of using metal protection layers is the competition of light absorption with the semiconductor underneath. One way to overcome this drawback is to illuminate from the back side of photoelectrode instead of the electrolyte side. For example, Bae *et al.* reported that by thinning the p-Si photocathode from 350 μm to 30 μm by wet etching, increased photocurrent density was observed by illuminating the Si from the back side.¹¹¹ In this configuration, the protection was achieved by depositing Ti/TiO₂ (5/100 nm) on the surface. Kang *et al.* changed the catalytic side of photoelectrode from the semiconductor/electrolyte junction to the ohmic contact/electrolyte interface using printing-based material assemblies.¹¹ In this case, the "thick" layer of metal contact (AuGe/Ni/Au: 100 nm/30 nm/150 nm) was used to separate the GaAs photocathode from an aqueous electrolyte, realizing 8 hours stable HER. The unprotected one showed quick performance decay with 2 hours.

As discussed in section 3.5.4, stable metal oxides and nitrides have been developed as protection layers. For example, amorphous TiO₂ has been deposited on BiVO₄ photoanode by ALD, followed by sputtering of Ni on the surface as the OER catalyst.²⁰ With the thickness around 1 nm, this amorphous protection layer achieved stable water oxidation in pH 13 electrolyte for 120 min, while the bare BiVO₄ showed quick decay of performance within 20 min due to the chemical and photoelectrochemical dissolution. On the photocathode side, it has been reported that Cu₂O photocathodes can be stabilized via the deposition of ZnO (20 nm) and TiO₂ (10 nm) by ALD.⁴⁶ It should be noted here that the deposition of TiO₂ alone didn't stabilize the photocathode, which was attributed to the formation of pin-holes between the Cu₂O / TiO₂ interface due to non-uniform growth even using ALD. The insertion of ZnO between Cu₂O and TiO₂ might provide a more uniform hydroxylated surface for TiO₂ to achieve conformal deposition. This demonstrates the important synthetic challenge of

depositing pin-hole free protection layers to achieve long-term stability.

In addition, some carbon-based materials, such as graphene, have also been used to protect photoelectrodes like macroporous silicon wafers.¹¹² Zhang *et al.* reported carbon-protected Cu₂O nanowire arrays that showed improved stability with a carbon layer compared with the bare nanowires.¹¹³ The thin, uniform layer of carbon (20 nm) was deposited via the decomposition of a glucose solution on Cu₂O at 550 °C in an N₂ atmosphere. The carbon-protected Cu₂O also showed photocurrent enhancement from -2.28 mA/cm² to -3.95 mA/cm² at 0 V, and the photocurrent decay was inhibited from 87.4% to 19.3% over a 20 min stability test.

4.2 Kinetic protection layer

As discussed above, catalysts are usually necessary to improve water oxidation and reduction performance no matter which semiconductors are studied as the photoelectrodes. Since the nature of photocorrosion is usually the reaction between semiconductors and photo-generated carriers in the presence of H₂O, it should be effective to protect the material by transferring the photo-generated carriers from the semiconductor to the desired chemical reaction. Indeed, various OER and HER catalysts have been demonstrated to reduce the degree of photocorrosion (some examples have been discussed in section 3.5.4).

For example, ultrathin Ni metal (2 nm) films have been demonstrated to protect planar n-Si photoanodes.⁹⁸ The role of Ni was shown to form semiconductor-insulator-metal (Si-SiO₂-Ni) junction to improve the charge separation of Si, as well as forming OER catalyst species on the surface. Combined with a potassium borate and lithium borate electrolyte, the integrated photoanode was shown to be stable against photocorrosion for 3 days. It was suspected that the Li⁺ helped eliminate the formation of α -phase Ni(OH)₂, thus avoiding large volume expansion of Ni layers during the oxidation process and enhancing the stability.

One important factor limiting the protection ability of thin-film catalysts is the chemical instability of catalysts under operating conditions. To address this issue, Kuang *et al.* recently reported an *in-situ* regeneration method to deposit a NiFe-based OER catalyst on BiVO₄ to extend its stability.⁴¹ With Ni as the substrate, the BiVO₄ photoanode showed gradual performance enhancement during the stability test in a borate buffer (pH 9). This was attributed to the formation of an amorphous NiFe-based catalyst (~ 5 nm), where the Ni²⁺ comes from dissolution of the NiO and Ni(OH)₂ layers on the Ni substrate and the Fe^{x+} species comes from impurities in the electrolyte. Long-term stability of over 1000 hours has been achieved, due to the regeneration of NiFe-based catalyst on BiVO₄ sites where the catalyst has been exfoliated or dissolved. Low concentration of Ni²⁺ (< 1 μM) and the borate electrolyte are key factors for this strategy. Higher concentration of Ni²⁺ caused overloading of the catalyst to increase surface charge recombination, while the choice of other electrolytes, such as phosphate, accelerated the catalyst dissolution.

The application of catalysts as protection layers has its own limitations. First, the relatively slow kinetics of water oxidation and water reduction makes it difficult to fully inhibit the photocorrosion via kinetic control. Second, the stability of catalysts can be an issue. The stability includes both the structural stability of catalysts and their attachment to the substrate. Third, there are more and more reports indicating that porosity and ion-permeability is critical to achieve high-performance OER catalyst and form a favorable interface with semiconductors, such as the transition-metal-based (oxy)hydroxide. As a result, the contact between unstable semiconductors and water may not be completely avoided. Therefore, the combination of both types of protection layer may ultimately be the winning strategy to achieve optimized stability and performance of photoelectrodes.

5 Thin film catalysts

The performance of thin film catalysts on photoelectrodes is not only affected by the electrocatalytic activity of the catalyst, but also by the interface between catalyst and semiconductor. Understanding along this direction is critical to design efficient photoelectrode systems. In addition, the problems introduced by the catalysts, such as the parasitic light absorption, need to be carefully considered in order to optimize the overall performance.

5.1 The role of catalysts on photoelectrodes

It has become widely recognized that catalysts are critical components in photoelectrode configurations in order to achieve high performance for both OER and HER. For OER, various catalysts including precious metal (e.g. Ir^{52, 53, 114, 115}) and transition metal (e.g. Co, Ni and Fe) oxides^{12, 62, 67} and (oxy)hydroxides^{22, 27, 70, 116} have been studied extensively and shown promising results. For HER, precious metal (e.g. Pt^{19, 47, 103}) and transition metal based catalysts (e.g. MoS₂^{57, 104} CoP,¹⁰³ etc.) have been employed. Many examples have been discussed in section 3. Despite the critical importance of the semiconductor-catalyst junction and the large number of studies investigating the behavior, the mechanism(s) concerning how the catalysts affect the performance remains a topic of current debate. One of the complications is that different synthetic methods of a given semiconductor can influence the behavior with a given catalyst, coupled with many different semiconductor materials and catalyst compositions that have been investigated using different methods. Below we summarize selected examples and unify the interpretations to present a general picture of the semiconductor / catalyst junction.

Typically, when semiconductors are coated with catalysts, either the turn-on potential or photocurrent density or both can

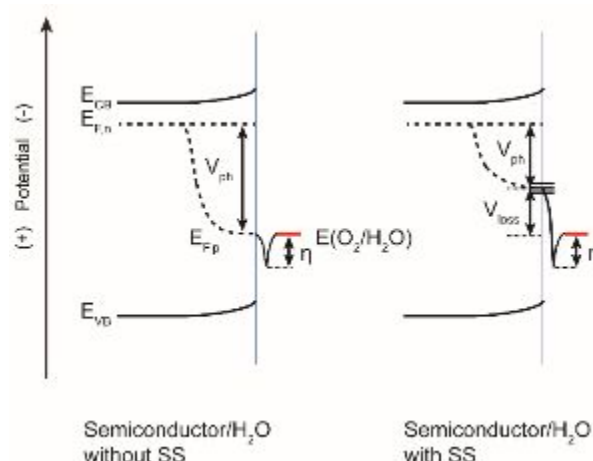


Figure 15 The schematic shows that how the hole quasi Fermi level ($E_{F,p}$) affected the performance of photoelectrodes. When there are no surface states (SS) on the semiconductor/liquid interface, the overpotential is mainly the kinetic overpotential (η); when there are SS, recombination decreased the photovoltage, leading to increased overpotential (V_{loss}). $E_{F,n}$: the electron quasi Fermi level.

be improved. From a fundamental perspective, the photocurrent density can be described by the following two equations (using a photoanode as the example).¹¹⁷

$$\frac{P_s}{P_s^0} = \exp\left(-\frac{q\Phi}{kT}\right) = \exp\left[-\frac{q(E_{app} + V_{ph} - E_{FB})}{kT}\right] \quad (5.1)$$

$$i_p = i_p^0 \left\{ \frac{P_s}{P_s^0} \exp\left(\frac{q\alpha_p \eta}{kT}\right) - \exp\left[-\frac{q(1-\alpha_p)\eta}{kT}\right] \right\} \quad (5.2)$$

In equation (5.1), P_s is the concentration of surface holes; P_s^0 is the equilibrium concentration of surface holes; q is the charge of electrons; k is the Boltzmann constant; T is the temperature; Φ is the magnitude of band bending, which is determined by the combination of applied potential (E_{app}), photovoltage (V_{ph} , defined as the difference of Fermi level under dark and light conditions) and the flat-band potential (E_{FB}). The equation (5.2) is derived from the Butler-Volmer equation assuming that charge transfer kinetics is dependent on the surface hole concentration. In equation (5.2), i_p is the photocurrent of holes under light; i_p^0 is the exchange current under dark; α_p is the hole transfer coefficient; η is the overpotential to drive the water oxidation reaction.

From those two equations, it is clear that the photocurrent generated from photoanodes is determined by a convolution of thermodynamic and kinetic factors (Figure 15). The extent of band bending at the semiconductor/electrolyte interface is determined by the band edge positions and photovoltage which controls the surface electron and hole concentrations. In addition, reduced hole/electron recombination on the surface can also increase the surface hole concentration. The photovoltage determines the position of the hole quasi-Fermi level, which must ultimately be sufficiently positive of the water oxidation formal potential to drive the reaction.

Similarly, the turn-on potential, another important parameter to describe the photoelectrode performance, is affected by both thermodynamic and kinetic factors. Since the photovoltage determines position of the hole quasi-Fermi level, it also limits V_{on} . Therefore, reducing the overpotential of the reaction can further shift the V_{on} to its theoretical value. As a result, the “catalysts” on photoelectrodes can either serve the true catalyst to reduce the kinetic overpotential, as the conventionally defined, or tuning the surface energetics at the semiconductor/electrolyte interface, or both.

In order to understand the role of catalysts on semiconductor surfaces, various techniques have been applied, including transient absorption spectroscopy (TAS)^{118, 119}, photoelectrochemical impedance spectroscopy (PEIS)^{114, 120-122}, intensity modulated photocurrent spectroscopy (IMPS)^{68, 103, 114, 123, 124}, dual-working-electrode (DWE) technique¹²⁵⁻¹²⁸ and more recently potential-sensing electrochemical atomic force microscopy (PS-EC-AFM)¹²⁹. With more and more evidence being discovered, the roles of catalysts on the semiconductor surface become gradually clear. Here we reviewed thin-film semiconductor/catalyst systems that studied by different techniques, and corresponding conclusions to reveal the role of catalysts.

5.1.1 Transient absorption spectroscopy

Barroso *et al.* reported a TAS study on hematite photoanodes with different material added to modify the surface (Figure 16).¹¹⁹ In one system, CoO_x was added to serve as the co-catalysts, while a Ga_2O_3 overlayer was added in another system, which is electrocatalytically inert. Interestingly, a negative shift of V_{on} was observed in both cases. The TAS study under applied bias showed that both treatments increased the absorption signals attributed to long-lived holes, and the shift of signal amplitude was consistent with the negative shift of V_{on} observed in J - V curves (Figure 16). From this, the authors concluded that both CoO_x and Ga_2O_3 treatments likely passivate surface states thereby reducing electron/hole recombination and increasing the yield of long-lived holes at the electrode surface.

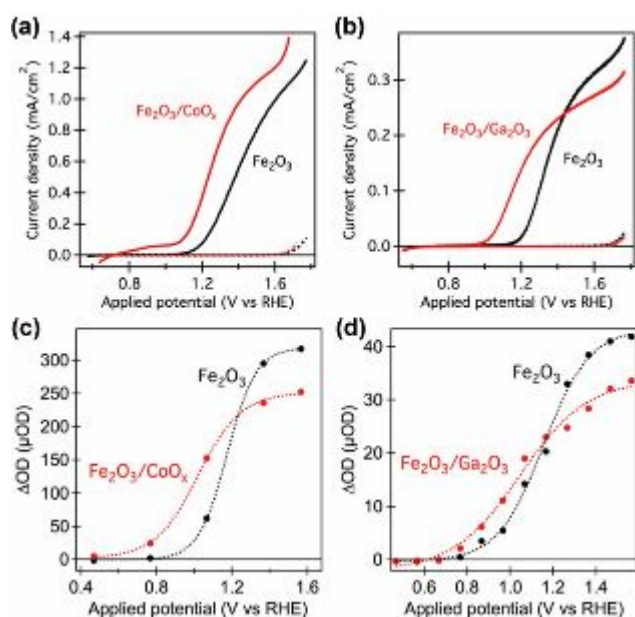


Figure 16 (a) The J - V curves of bare hematite grown by APCVD method and hematite coated with CoO_x overlayers. (b) The J - V curves of ultrathin hematite grown by Ultrasonic spray pyrolysis (USP) method and hematite coated with Ga_2O_3 overlayers. Electrolyte: 0.1 M NaOH (pH 12.6); Light source: 1 sun, AM 1.5G. The amplitude of 700-nm transient absorption measured at 50 ms after laser excitation as a function of applied bias was shown in (c,d). (a-d) reproduced from ref. 119 with permission from the National Academy of Science.

Similarly, Barroso *et al.* studied the role of Co-Pi, another widely used OER catalyst, on the surface of hematite photoanodes.¹¹⁸ The electrodeposited Co-Pi on mesoporous hematite thin-film photoanodes also shifted the V_{on} to more negative values and increased the J_{ph} at 1.4 V by 0.1 mA/cm². The TAS results in the absence of applied bias indicated the addition of Co-Pi significantly increased the lifetime of the transient signal by more than 3 orders of magnitude, with the half-life ($t_{1/2}$) increased from ~ 15 μs to ~ 30 ms. The authors interpreted this behavior as retarded charge recombination in hematite due to the formation of Schottky-type heterojunction between hematite and Co-Pi.

5.1.2 Photoelectrochemical impedance spectroscopy

PEIS has been widely used to measure the charge transfer processes of photoelectrodes. The key of PEIS lies in constructing meaningful equivalent circuit models that accurately describe the relevant charge-transfer processes which ultimately control the J - V behavior. The development of appropriate equivalent circuit for photoelectrodes has been extensively investigated by Bisquert *et al.* during the past decade.^{120, 130-133} By studying the PEIS results for the bare photoelectrodes and the one with catalyst on the surface, the role of catalysts can be clarified.

Klahr *et al.* studied hematite thin-film photoanodes grown via ALD with different thicknesses of cobalt phosphate (Co-Pi) as an OER catalyst (Figure 17).¹²⁰ To overcome complications in interpretation due to heterogeneity of mesoporous photoelectrodes and competitive light absorption by the catalysts, light was illuminated from the back side of FTO-glass substrates. It was found that the photocurrent and turn-on potential of hematite was improved when the thickness of Co-Pi increased. After fitting analysis in the corresponded equivalent circuit for Co-Pi decorated hematite, it was found that the capacitance for Co-Pi ($C_{\text{Co-Pi}}$) increased and the charge transfer resistance from the Co-Pi layer ($R_{\text{ct, Co-Pi}}$) decreased as the increased thickness of Co-Pi layer. Together with the transient photocurrent measurement and chopped light measurement, it was concluded that Co-Pi improved the performance of water oxidation by efficiently collecting and storing photogenerated holes from hematite. The increased charge separation was invoked to explain the improved performance as it led to reduced charge recombination at the semiconductor/electrolyte interface.

Riha *et al.* studied the effect of sub-monolayer $\text{Co}(\text{OH})_2/\text{Co}_3\text{O}_4$ catalyst on the performance inverse-opal scaffolded hematite photoanode.¹²¹ Deposition of only 1 ALD cycle, the sub-

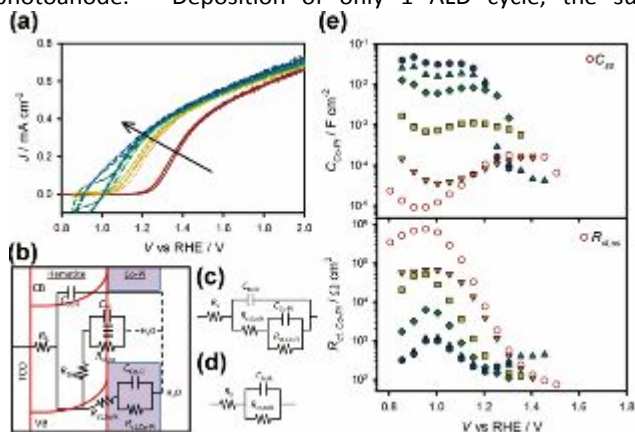


Figure 17 (a) The J-V curves of a bare hematite (red solid line) and the same electrode coated with 1 (orange dotted line), 2 (yellow short dashed line), 15 (green dashed double dotted line), 45 (teal long dashed line) and 90 (blue dashed single dotted line) mC/cm^2 Co-Pi in a pH 6.9 buffer solution under 1 sun illumination. The equivalent circuits used for PEIS interpretation were shown as the full one (b), simplified one for Co-Pi coated hematite (c) and Randles' circuit used when only one semicircle is visible (d). (e) The $C_{\text{Co-Pi}}$ and $R_{\text{ct, Co-Pi}}$ values fit from PEIS data of hematite with 1 (orange triangle pointing down), 2 (yellow squares), 15 (green diamonds), 45 (teal triangles pointing up) and 90 (blue hexagons) mC/cm^2 Co-Pi on the surface. The C_{ss} and $R_{\text{ct, ss}}$ values were shown for comparison (red open circles). (a-e) reprinted with permission from ref. 132. Copyright 2012 American Chemical Society.

monolayer Co-based catalyst shifted the V_{on} by 200 mV and increased J_{ph} from 1.4 to 2.1 mA/cm^2 at 1.53 V. By performing the PEIS measurement on planar thin-film hematite photoanode and assuming the charge transfer occurred through the surface states, it was found the capacitance of surface states decreased after ALD modification when water oxidation occurred, indicating faster hole transfer resulting lower steady-state hole concentration. In addition, the charge transfer resistance from the surface states was much lower compared with the un-modified hematite. Together, these results were interpreted as the Co-based catalyst accelerating the hole transfer kinetics, thereby acting as the water oxidation catalyst in the conventional sense.

5.1.3 Intensity modulated photocurrent spectroscopy

The IMPS technique was developed by Peter *et al.* in late 1980s, which measures the phase shift in photocurrent in relation to a sinusoidal modulation of light intensity.¹³⁴⁻¹³⁷ Several assumptions need to be satisfied in order to obtain meaningful IMPS data: (i) the surface hole concentration changes linearly with the light intensity; (ii) the light intensity modulation is sufficiently low so that only the surface hole concentration is

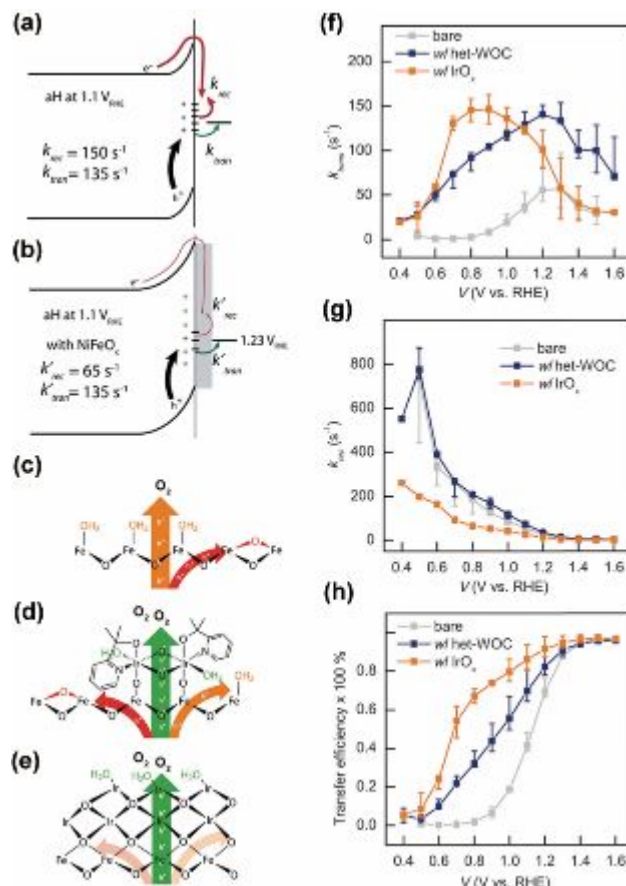


Figure 18 Schematic of bare hematite/electrolyte interface (a) and hematite/ NiFeO_x /electrolyte interface (b) showed the deposition of NiFeO_x on hematite mainly decreased the k_{rec} , suppressing the charge recombination. (c-d) The schematic showed different hole transfer pathways in bare hematite (c), the one with heterogenized molecular Ir catalyst (het-WOC) (d) and the one with IrO_x thin films (e). The values of k_{tran} , k_{rec} and transfer efficiency for three hematite samples obtained from IMPS data were shown in (f-h), respectively. (a-b) reproduced from Ref. 123 with permission from the Royal Society of Chemistry. (c-h) reproduced from Ref. 114 with permission from the Royal Society of Chemistry.

altered instead of the degree of band bending; (iii) the reaction process is dominated by a single step kinetically and the surface hole concentration falls into the first-order reaction region. By analyzing the complex photocurrent as a function of light modulation frequency, the surface charge transfer rate constant (k_{tran}) and surface charge recombination rate constant (k_{rec}) can be derived, using which the charge transfer efficiency (TE, $\text{TE} = k_{\text{tran}} / (k_{\text{tran}} + k_{\text{rec}})$) can be obtained. The rate constants describe the charge transfer process on photoelectrode/electrolyte interface thermodynamically (k_{rec}) and kinetically (k_{tran}).

Du *et al.* found that decoration of a hematite surface with NiFeO_x via a photochemical decomposition method could shift

the V_{on} negatively by 400 mV.¹¹⁶ Measurements of the photovoltage by comparing the open circuit potential in the dark and under illumination revealed that NiFeO_x increased the photovoltage by reducing Fermi level pinning, which was caused by the hematite surface states. With the help of IMPS measurements, detailed kinetics parameters were extracted for the NiFeO_x/hematite system.¹²³ By comparing the bare hematite and the one with NiFeO_x, it was found that k_{tran} remained the same for both photoanodes at 1.1 V for water oxidation, but the one with NiFeO_x showed lower k_{rec} compared with the bare one (Figure 18a and 18b).¹²³ The result indicated that NiFeO_x improved the water oxidation performance by reducing the surface charge recombination.

Li *et al.* studied the effect of two different Ir-based catalysts on the performance of hematite photoanode.¹¹⁴ It was found the addition of either IrO_x or a heterogenized molecular Ir catalyst on the hematite surface led to a negative shift of V_{on} and increased J_{ph} in 0.1 M KNO₃ (pH 1.01). While the IrO_x was deposited on hematite as a dense thin film, the Ir molecular catalyst was anchored on the surface via the direct binding with Ir centers, with the molecular identity remained (Figure 18c-e). IMPS study revealed that compared with the bare hematite, the IrO_x-decorated one showed increased k_{tran} and decreased k_{rec} , while the one with the heterogenized molecular Ir catalyst showed only increased k_{tran} but similar k_{rec} as the bare one (Figure 18f-h). By increasing the loading amount of these two catalysts, it was found that only k_{rec} increased for Ir molecular catalyst, while both k_{tran} and k_{rec} were improved for IrO_x. As a result, it was concluded that the application of Ir molecular catalyst provided additional hole transfer pathway while the surface recombination still occurs via surface states at the hematite/H₂O interface. As a comparison, the IrO_x dense thin film replaced the original hematite/H₂O interface to reduce the charge recombination and increased the hole transfer at the same time.

In addition to hematite, IMPS studies have also been applied to other semiconductor/catalyst systems. For example, Zachäus *et al.* studied the influence of Co-Pi on the charge transfer processes on BiVO₄ photoanodes.¹²⁴ It was found that the performance of BiVO₄ was mainly limited by the surface charge recombination instead of water oxidation kinetics. By comparing the k_{tran} and k_{rec} of bare BiVO₄ and the one with Co-Pi, it was found that the addition of Co-Pi decreased the k_{rec} by a factor of 10-20 over the entire potential range (0.6-1.5 V), while the k_{tran} remained unchanged when the potential was less than 1 V. Furthermore, the addition of the efficient RuO_x OER electrocatalyst decreased the performance because it failed to passivate the surface states on BiVO₄. Moreover, Liu *et al.* reported the decoration ferrihydrite and Ni(OH)_x as "hole-storage" layer on Ta₃N₅ photoanode significantly increased its performance.⁶⁸ IMPS study revealed that the charge carrier lifetime was prolonged by 2 to 6 times after the hole-storage layer deposition. Meanwhile, the k_{rec} decreased dramatically while k_{tran} was not improved, indicating reducing surface recombination rather than enhancing surface hole transfer was the main function of such a hole-storage layer.

In addition to OER catalysts, the effect of HER catalysts on photocathodes has been studied via IMPS.¹⁰³ Using a Si photocathode with GaN nanowires grown on it, different HER catalysts were deposited including Pt, Ag and cobalt phosphide (CoP). It was found that under all three cases the V_{on} and J_{ph} was improved and Pt was the most effective one, followed by CoP and Ag. The IMPS results revealed that adding Ag or Pt reduced k_{rec} by one order of magnitude over a wide range of potential window (even before V_{on}), while adding CoP only reduced the k_{rec} after the turn-on potential. This indicated that CoP functioned as a HER catalyst quite differently from the metals on the semiconductor. For CoP, it couldn't accept the charge from the photocathode at low applied potential, leading to

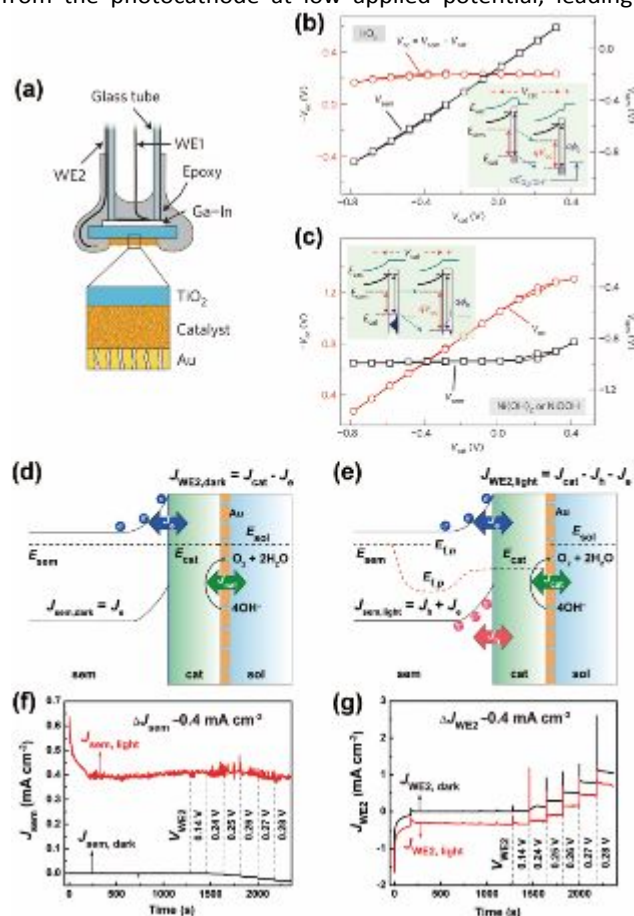


Figure 19 (a) The schematic showed DWE device configuration, in which TiO₂ was the first working electrode and the porous gold layer on the catalyst was the second working electrode. The measured open-circuit potentials of the semiconductor (V_{sem}) and calculated open-circuit potential across the semiconductor/electrocatalyst (SC/EC) junction (V_{oc}) as the function of applied potential on the electrocatalysts (V_{cat}) were shown for IrO_x-coated TiO₂ (b) and Ni(OH)₂-coated TiO₂. The inset band diagrams showed how the V_{oc} changed with V_{cat} in these two systems. (d) and (e) illustrated the band bending schematic at the interface of hematite and NiFeO_x catalysts under dark and light conditions. (f) Current densities of hematite (J_{sem}) when the applied potential on hematite (V_{sem}) was fixed at 0 V vs. E (O₂/OH⁻) while the potential of catalysts (V_{WE2}) were controlled in a chronoamperometry experiment. (g) Current densities measured from catalysts (J_{WE2}) under different V_{WE2} vs. E (O₂/OH⁻), while V_{sem} was fixed at 0 V vs. E (O₂/OH⁻). (a-c) reproduced from Ref. 125 with permission from Springer Nature. (d-g) reprinted with permission from Ref. 127. Copyright 2017 American Chemical Society.

severe charge recombination and limited photovoltage. On the

other hand, the metals (Pt or Ag) can extract the charge through the formation of Schottky junctions and reduce charge recombination. With further enhanced charge transfer kinetics, such as with Pt, the highest performance was achieved.

5.1.4 Dual-working-electrode technique

In 2007 Peter employed a second evaporated Ti working electrode to sense the potential of TiO₂ nanoparticles away from the conductive substrate to establish working model of such electrodes used in dye-sensitized solar cells.¹³⁸ A similar dual working electrode (DWE) technique was used by Lin *et al.* for dense IrO_x and ion-permeable Ni(OH)_x OER catalysts integrated on TiO₂ photoanodes.¹²⁵ By depositing a thin layer of porous Au on the surface of the catalyst, without forming direct contact with the semiconductor, they were able to simultaneously sense and control the current and potential of both the TiO₂ semiconductor and the catalyst under working conditions (Figure 19a). Unlike TA, EIS, IMPS methods which are indirect and model-dependent for results interpretation, the DWE offers a direct measure of the catalyst and the interpretation is less ambiguous.

It was found that the dense, ion-impermeable IrO_x formed a Schottky-type buried junction with TiO₂, leading the constant photovoltage of only 0.2 V, which explains the relatively poor performance of this system despite IrO_x as one of the best OER catalysts (Figure 19b). However, since the Ni(OH)_x catalyst is ion-permeable, it can store charge via redox reactions of the Ni ions. Since oxidation of the Ni ions lowers to catalyst potential, the photovoltage of the junction with TiO₂ increases and this is therefore termed an “adaptive junction” (Figure 19c). Since the catalyst potential was measured directly, as well as the current at the catalyst which matched the current at TiO₂, it was concluded that hole transfer was efficient from TiO₂ to Ni(OH)_x and the OER occurred primarily via the catalyst. As a result, improved turn-on potential and fill factor was observed for the TiO₂/Ni(OH)_x system.

Qiu *et al.* later reported the application of DWE technique on hematite photoanodes coated with the Ni_{0.8}Fe_{0.2}O_x catalyst where a thin layer of porous Au was deposited on the surface of Ni_{0.8}Fe_{0.2}O_x to form the second working electrode (Figure 19d and 19e).¹²⁷ It was found that the conductivity of catalyst increased sharply after oxidation of the Ni species, no matter the catalyst was on conductive substrate (ITO) or hematite photoanode. By monitoring the photocurrent of hematite and the current of catalyst at the same time over a wide range of applied bias, it was found that hole transfer from hematite to the catalyst occurs with an efficiency up to 95% (Figure 19f and 19g). This result indicates that the Ni_{0.8}Fe_{0.2}O_x not only serves as a hole-collecting contact but also as the catalyst to drive water oxidation. In addition, the authors found that the heterogeneity of the catalyst could affect the hole collection from semiconductor to the catalyst, which may explain the difference between various reported results for the role of catalyst.

Qiu *et al.* later reported the effect of semiconductor morphology and catalyst conductivity on the photoelectrode performance via the DWE technique.¹²⁸ Two types of hematite with different morphologies and two types of NiFeO_xH_y with different conductivities (as well as OER activity) were combined

to illustrate the effect. Electrodeposited (ED) hematite on FTO substrates featured a porous morphology while the ALD electrode forms a compact, dense thin film. Ni_{0.8}Fe_{0.2}O_xH_y has better conductivity and OER activity compared with Ni_{0.2}Fe_{0.8}O_xH_y. However, the Ni_{0.2}Fe_{0.8}O_xH_y decorated ED hematite showed much worse performance than the one with Ni_{0.8}Fe_{0.2}O_xH_y, while the ALD hematite showed good performance after the deposition of both catalysts. By measuring the potential of the catalyst as a function of semiconductor potential, it was found that charge recombination due to the direct contact between the conductive catalyst and FTO substrate occurred which inhibited the performance. To avoid this shunting, photo-assisted electrodeposition of catalyst on ED hematite was carried to avoid the direct contact between FTO and catalyst, which shown much better performance compared with one deposited via photochemical decomposition. The study pointed out the importance to avoid shunting using porous semiconductors with catalysts, which could be achieved by photo-assisted electrodeposition method, or preventing the direct contact between catalyst and conductive substrate by inserting insulating layer or electronically insulating catalyst between them.

5.1.5 Potential-sensing electrochemical atomic force microscopy

Although the DWE technique can reveal the electrochemical information of catalyst layers during the reaction, its application is generally limited to planar photoelectrodes. High-aspect-ratio substrates can lead to the non-uniform coverage of second working electrode layer, resulting in direct electrical shorting to the semiconductor. To overcome this problem, Nellist *et al* developed a method to use an electrochemical AFM to sense the local potential of catalysts on different morphologies of photoanodes.¹²⁹ In this configuration, an electrically insulated AFM cantilever was modified with a conductive nanotip of Pt. As a result, the tip-substrate interaction could be controlled by

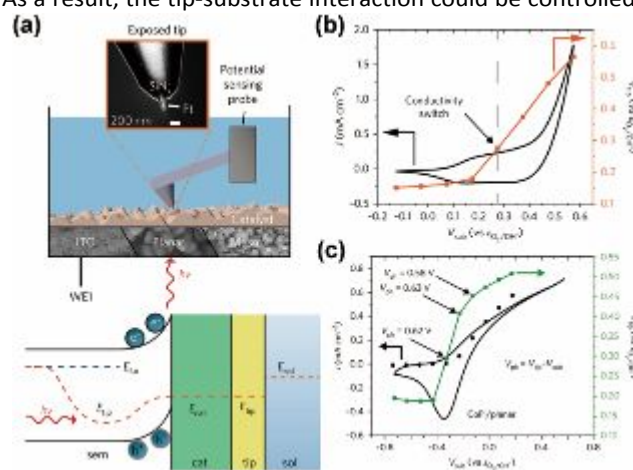


Figure 20 (a) The schematic shows the electrochemical AFM set up to measure the catalyst potential during (photo)electrochemical water oxidation. The inset is a TEM image of the AFM tip. The band diagram shows the equilibrium of tip potential (E_{tip}) with the catalyst potential (E_{cat}) during the PEC measurement. (b) The J-V curve of Co-Pi coated ITO electrode in 0.1 M phosphate buffer (pH 6.9) and the corresponding tip potentials. (c) The J-V curve of Co-Pi coated planar hematite photoelectrode in the same electrolyte and the corresponded tip potentials. Light source: 405 nm light with 27 mW/cm². A clear switching of tip potential was observed in both (b) and (c). (a-c) reproduced from ref. 129 with permission from Springer Nature.

force feedback through cantilever deflection, so that the potential of substrate (the catalyst layer) could be detected without damaging the catalyst layer (Figure 20a).

The PS-EC-AFM was used to study the effect of Co-Pi on both planar and nanostructured hematite photoanodes. The tip potential didn't track the increase of substrate potential until the Co^{2+} ions were oxidized and the catalyst layer became conductive (Figure 20c). It was observed that similar tip potentials were achieved for both Co-Pi coated ITO substrate under dark and Co-Pi coated hematite photoanode under light when the current density was the same, indicating the photogenerated holes were transferred from hematite to Co-Pi layer to drive the water oxidation reaction (Figure 20b). Study for other semiconductor/catalyst systems based on this technique can be promising to further reveal the role of catalysts on the semiconductors.

5.2 The effect of catalysts on the light absorption

The loading amount of catalysts has a great impact on the water oxidation/reduction performance. In order to achieve the optimized performance, the catalyst loading is considerably high, which introduced another problem in photoelectrodes. That is, the usually opaque electrocatalysts compete with the underneath semiconductors in terms of light absorption. To avoid this competition, mainly two strategies have been employed in the literature: (i) decoupling the reaction sites with light absorption sites; (ii) synthesis of catalysts with high intrinsic activity to reduce the loading amount, which will be transparent for the incident light.

5.2.1 Decoupling reaction sites and light absorption sites

The most convenient method to overcome competitive light absorption by the catalyst layer is to illuminate the photoelectrode from the back side (the ohmic contact side) instead of front side (the catalyst side). Such a method requires the deposition of semiconductor thin films on the transparent and conductive substrate, such as the conductive oxide coated glass (e.g., FTO and ITO). In addition, the thickness of semiconductors needs to be controlled so that the photo-generated carriers can reach the surface before recombination. For example, Du *et al.* synthesized the amorphous NiFeO_x layer on the surface of ALD grown hematite (25 nm) via a photochemical decomposition method.¹¹⁶ Due to the brown color of NiFeO_x , it competed with the light absorption of hematite. With illumination from the back side of photoelectrode, the J_{ph} at 1.23 V was enhanced by almost 70%. Similarly, Klahr *et al.* reported that Co-Pi decorated hematite thin film photoanode.¹²⁰ Since Co-Pi broadly absorbed visible light, back illumination was used so that the performance of hematite could be optimized by controlling the thickness of Co-Pi thin films.

Another method to achieve this goal is to selectively deposit the catalyst instead of a uniform deposition on the surface of photoelectrodes so that only a small portion of incident light will be blocked by the catalysts even under the front illumination. Such a strategy often requires the synthesis of high-aspect-ratio semiconductors. For example, Shaner *et al.* reported a Si microwire design consisting of Si microwire arrays

with the height of 100 μm , 5-10 μm of Ni-Mo HER catalyst on the bottom of microwire, with additional 1-3 μm of light-scattering TiO_2 particles.¹³⁹ The light absorption was enabled by the exposed Si microwires, while the photo-generated carriers were transferred to Ni-Mo HER catalyst on the bottom of microwires. The addition TiO_2 further enhanced the light absorption by light-scattering. In addition, Vijselaar *et al.* reported the selective deposition of Ni-Mo HER catalysts on the top of Si microwires.¹⁴⁰ The Si surface was first conformally covered with SiO_2 , followed by addition of a photoresist layer, which was etched in O_2 plasma to expose the top of wires. Then the exposed SiO_2 was etched away so that only the top of Si could be electrodeposited with Ni-Mo HER catalyst (Figure 21a and 21b). Through the selective deposition, it was found the light absorption by Ni-Mo was inhibited compared with the one with fully exposed Si surface after the same catalyst deposition time. As a result, the J_{ph} was improved by over 6 times.

In addition, the decoupling of light absorption with photocatalytic activity can be achieved by changing the assembly method of semiconductors. For example, Kang *et al.* reported an epitaxial lift-off and printing-based assemblies to prepare the GaAs-based photocathode.¹¹ After removing from the growth substrate of GaAs wafers, the photocathode was sealed into transparent, photocurable polymer, which was further assembled onto glass substrate. As a result, the back ohmic contact layer was facing the electrolyte side, with Pt HER catalysts on it (Figure 14b). In this bifacial configuration, the light penetrated from the glass side while the electrons were collected on the backside to electrolyte.

5.2.2 Synthesis of transparent catalysts

There are limitations of using geometrical approaches to reduce the effect of light absorption by catalysts. For example, in conventional tandem cell configurations, it is critical to allow the light absorption by the smaller band gap photo absorber underneath the top absorber. Thus, light must pass through the top catalyst layer before reaching the bottom cell. Therefore, a more ideal approach is to synthesize a transparent catalyst layer with high activity.

For instance, Morales-Guio *et al.* reported the synthesis of semi-transparent FeNiO_x catalysts on hematite photoanodes via photo-assisted electrodeposition.⁴⁹ It was found that the oxidative deposition of NiO_x in pH 5.3 was much slower due to

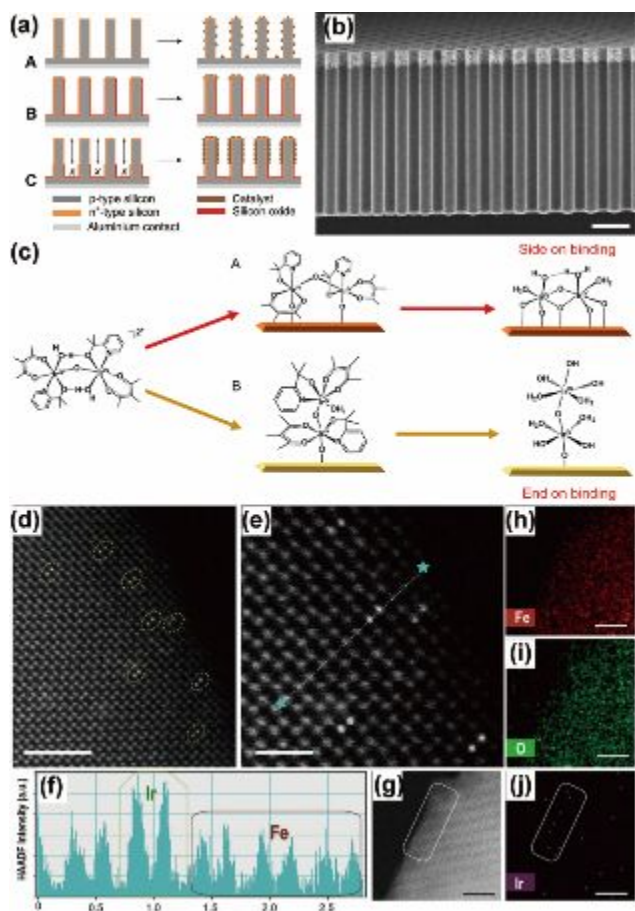


Figure 21 (a) The schematic shows the fabrication process for three types of Si microwires: fully exposed (A), with top exposed (B) and with defined exposed areas (C). (b) The SEM image of Si microwires with Ni-Mo HER catalysts deposited on the top. Scale bar: 10 μm . (c) The schematic shows synthesis processed for side-on (A, on $\alpha\text{-Fe}_2\text{O}_3$) and end-on (B, on WO_3) bound Ir DHCs, which involves the adsorption of molecular dinuclear precursors and the removal of organic ligands by photochemical processes. (d-e) The high-angle annular dark-field scanning TEM (HAADF-STEM) images of Ir FHCs on $\alpha\text{-Fe}_2\text{O}_3$. The circled bright pairs were Ir DHCs. (f) The HAADF intensity of the dotted line in (e). (g-h) The elemental mapping for Fe, O and Ir species. Scale bar: 2 nm in (d), 1 nm in (e), 4 nm in (g-h). (a-b) reproduced from ref. 140 with permission from Springer Nature. (c) reprinted with permission from ref. 115. Copyright 2018 American Chemical Society. (d-j) reproduced from ref. 53 with permission from the National Academy of Science.

faster corrosion of NiO_x films, with Fe incorporation further accelerating the corrosion process. As a result, the loading amount of FeNiO_x was low (4-7 nm in thickness), leading to low light absorption by the catalyst layer. In addition, the as-deposited FeNiO_x featured a high turnover frequency (TOF) of 1.1 s⁻¹ with an overpotential of 0.35 V, which was almost 10 times of that for NiO_x at the similar loading amount. The FeNiO_x decorated hematite achieved higher J_{ph} and better V_{on} compared with the bare or NiO_x-decorated hematite.

Another approach that has also been reported recently is to reduce the size of the catalyst to the atomic scale, which can result in improved intrinsic activity of the catalyst with high

atomic efficiency and negligible light absorption. Zhao *et al.* recently reported the synthesis single-atom catalysts (SACs) and dinuclear heterogeneous catalysts (DHCs) of Ir on hematite photoanodes (Figure 21d-j).⁵³ The DHCs were synthesized via the photochemical decomposition of the organic ligands in Ir homodimers, consisting of two Ir atoms per catalytic site in the form of Ir-O-Ir arrangement. The Ir DHCs decorated hematite showed the best V_{on} (0.55 V) and highest J_{ph} compared with Ir SACs and Ir nanoparticles in pH 6 electrolyte. The measured TOF for Ir DHCs is 2.6 and 5 times higher than the corresponding Ir SACs and nanoparticles. DFT calculation indicated that the energy required after the second proton-coupled electron transfer (PCET) process was much lower in DHCs compared with the Ir SACs. Similarly, DHCs of Ir was synthesized on WO_3 photoanode, but with different bonding configuration compared with the one on $\alpha\text{-Fe}_2\text{O}_3$ surfaces.¹¹⁵ It was found that only one Ir atom was anchored on the WO_3 surface with second Ir atom on top of the first Ir (end on bonding), while two Ir atoms were anchored on the $\alpha\text{-Fe}_2\text{O}_3$ surfaces (Figure 21c). The difference comes from the density and distance of binding sites on different surfaces. In addition, the WO_3 photoanode coated with DHCs of Ir showed higher product selectivity for O_2 instead of peroxide species compared with bare WO_3 and the one coated with SACs of Ir, which was explained as more favorable water oxidation pathways having a second Ir site.

In addition to OER catalysts, synthesis of semi-transparent HER catalysts have also been explored. For instance, Roger *et al.* reported a hydrothermal synthesis method to deposit $Co_2Mo_3S_{26}$ thin films on FTO-coated glass from aqueous solution of cobalt sulfate, ammonia heptamolybdate and thiourea at 180 °C for 72 hours.¹⁴¹ With a thickness of 300 nm, such a thin film showed a translucent nature, but it still delivered current densities of 10 mA/cm² at 260 mV overpotential in 0.5 M H_2SO_4 . Furthermore, Ding *et al.* deposited amorphous MoS_xCl_y catalysts on n⁺⁺-Si micropylamid photocathodes through a low temperature CVD method.¹⁴² With a thickness between 40 and 60 nm, the MoS_xCl_y catalysts showed little light absorption in the 500 to 1200 nm wavelength region where Si absorbs strongly. As a result, the integrated photocathode showed V_{on} of 0.41 V and J_{ph} of 43.0 mA/cm² at 0 V in 0.5 M H_2SO_4 .

6 Applications

6.1 Study platform for fundamental properties of semiconductors and chemical reactions

Water oxidation mechanisms have been studied extensively on different materials. However, it still remains as a question that whether the current knowledge, which is usually studied in homogenous molecular catalysts, is transferrable to other water oxidation systems such as the heterogeneous systems. Photoelectrodes provide a unique study platform for water oxidation mechanism by constructing a semiconductor/liquid interface, with illumination and applied bias to control the hole concentrations on the surface. Indeed, mechanistic studies on photoelectrodes recently have shown promising results to identify the water oxidation intermediates and pathways. The

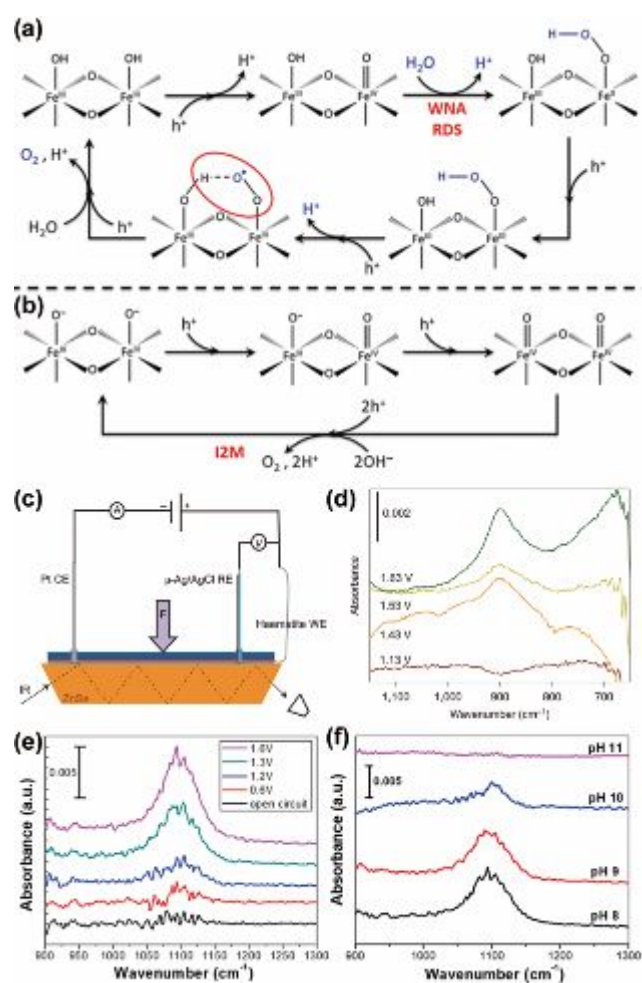


Figure 22 (a-b) The schematic shows two water oxidation mechanisms involving O-O bond formation as the rate determining step (RDS) on hematite photoanode: (a) Water nucleophilic attack (WNA) to a metal-oxo-species. (b) Intermolecular coupling mechanism (I2M) of coupling two metal-oxo or oxyl radical species. (c) The schematic shows the experimental set-up for operando ATR-FTIR measurement during PEC water oxidation. There was a thin layer of electrolyte between the hematite electrode and ATR crystal (ZnSe). (d) Infrared spectra of hematite scanned at different applied potentials under LED ($\lambda = 395$ nm) illumination. The V_{on} of hematite in the testing electrolyte (D_2O containing 0.2 M KCl) is 1.25 V. (e) Infrared spectra of hematite photoanode in 0.5 M $NaClO_4$ (pH 8) under AM 1.5G illumination at different applied potentials. The V_{on} of hematite photoanode was above 1.2 V. (f) Infrared spectra of hematite photoanode in the electrolyte with different pH under AM 1.5G illumination. (a-b) and (e-f) reprinted with permission from ref. 146. Copyright 2018 American Chemical Society. (c-d) reproduced from ref. 145 with permission from Springer Nature.

results can not only increase the understandings of water oxidation pathways, but also shed light on the future optimization of PEC devices. In those studies, the thin film photoelectrodes played an important role, which enabled the application of various techniques. Here we use hematite thin-film photoanodes as the example system for understanding water oxidation mechanisms on thin film photoelectrodes. For instance, Klahr *et al.* studied the photoelectrochemical properties of thin-film hematite for water oxidation by impedance spectroscopy.¹³² The equivalent circuit analysis of impedance result showed a correlation between the appearance of peak for surface states capacitance (C_{trap}) with

the valley of charge transfer resistance from surface states ($R_{ct,trap}$) and the turn-on potential of hematite for water oxidation. This led to a proposed mechanism where the transfer of photogenerated holes took place from the surface states on hematite/electrolyte interface instead of a direct transfer of holes from the valence band of hematite. Such a correlation could be explained as the photogenerated valence band holes oxidizing surface bound hydroxide to form a water oxidation intermediate species; formation of the intermediate presents itself as storing a hole in a surface state. The intermediate species builds up during the reaction suggesting subsequent steps in the overall water oxidation are rate limiting.

Le Formal *et al.* reported the rate law analysis of the order of water oxidation as a function of surface hole density on a hematite photoanode by photo-induced absorption spectroscopy.¹⁴³ It was found that under low light intensity (low surface hole concentration) the reaction order was close to 1, while under high light intensity (one sun, high surface hole concentration) the reaction order was close to 3, which corresponded to water oxidation to oxygen. The result provided convincing evidence that surface hole accumulation was required in the four electron water oxidation reaction. This study indicated the possibility of a concerted multi-hole water oxidation reaction on the hematite surface.

In addition, Zhang *et al.* studied the role of proton transfer during water oxidation on a hematite photoanode.¹⁴⁴ By comparing the photocurrent and turn-on potential of hematite in electrolytes with different pH, it was found that water molecule is the dominant reaction species for oxidation at low pH (<12) and high potentials (1.2 V), corresponding to a large kinetic isotope effect (KIE) when the hematite was tested in H₂O and D₂O electrolytes. This result indicates that the cleavage of the O-H bonds of water molecule was involved in the rate determining step (RDS) of water oxidation, which was a concerted proton-electron transfer (CPET) pathway. At higher pH or at low potential, much lower KIE values were observed, which indicating the electron transfer was the dominant pathway. The results indicated that the performance of hematite was limited kinetically by the proton transfer under near-neutral conditions.

More recently, the chemical nature of water oxidation intermediates on hematite surface has been revealed by operando attenuated total reflectance infrared spectroscopy (ATR-FTIR), which provide direct evidence for the proposed water oxidation mechanism (Figure 22a and 22b). Zandi *et al.* reported a potential- and light-dependent absorption peak at 898 cm⁻¹ on hematite surface during water oxidation reaction (Figure 22c and 22d).¹⁴⁵ The peak intensity increased with the increased applied potential and light illumination, indicating that it corresponded to a water oxidation intermediate on hematite surface. Through isotope labelling, the chemical nature of this peak was assigned to iron-oxo (Fe^{IV}=O) groups. Water oxidation mechanism was proposed that Fe^{IV}=O was formed after the first oxidation reaction of Fe^{III}-OH on hematite surface by valence-band holes.

Zhang *et al.* reported the detection of water oxidation intermediate by operando infrared spectroscopy in the electrolyte with different pHs.¹⁴⁶ Impedance spectroscopy revealed that a first-order dependence of photocurrent with the density of surface trapped holes under near-neutral (pH 10), while a third-order dependence was found at high pH (13.6). Furthermore, operando PEC ATR-IR measurements showed a peak evolution at 1100 cm⁻¹ with pH ranging from 8 to 10 under water oxidation condition (Figure 22e). Isotope labelling identified the peak assignment to a surface superoxide species that hydrogen bonded to an adjacent hydroxyl group. No peroxide or superoxide species were detected on the surface under water oxidation conditions when the electrolyte pH was higher than 11 (Figure 22f). The combination of rate law analysis and ATR-IR results indicated a water oxidation mechanism change from near-neutral pH to highly alkaline conditions. Under near-neutral pH, nucleophilic attack of water/OH⁻ to a metal-oxo species was proposed, while the coupling of neighboring metal-oxo species was proposed under alkaline condition.

6.2 Constructing the tandem cell configuration

The unique properties of thin-film photoelectrode make the tandem cell configuration possible, moving the field forward to more practical water splitting devices. Among the configurations, thin-film metal oxide photoanodes deposited on transparent substrates (e.g., FTO glass) have been used to couple with smaller band-gap photocathode or photovoltaic to construct the tandem cell PEC devices. Promising solar-to-hydrogen efficiencies (η_{STH}) have been achieved for various materials combinations, and the value has improved gradually due to more optimized photoelectrode component performances and cell designs. On the other hand, the high-efficiency III-V semiconductors have been optimized for integration, which further boosted the η_{STH} .

Brillet *et al.* reported a thin-film hematite or WO₃ photoanode stacked on a dye-sensitized solar cell (DSSC).¹⁴⁷ Light was incident on the photoanode before the underlying photovoltaic cell. Under one sun illumination, effective photocurrent densities of 0.95 mA/cm² and 2.52 mA/cm² were obtained from the hematite/DSSC and WO₃/DSSC devices, corresponding to a η_{STH} of 1.17% and 3.1%. Performance remained at 80% of the original value after 8 hours test, which was mainly attributed to the instability of DSSC.

Jang *et al.* reported the combination of hematite photoanode with amorphous Si photocathode to form a tandem device.²² Through the re-growth synthesis method and addition of NiFeO_x catalyst on hematite, a low V_{on} of 0.45 V was achieved for the hematite photoanode. Together with the amorphous Si photocathode which was decorated with TiO₂/Pt, η_{STH} of 0.91% was achieved in 0.5 M phosphate buffer (pH 11.8) for 10 hours. In addition, by replacing the NiFeO_x with an acid-stable IrO_x OER catalyst, the unassisted water splitting by hematite and amorphous Si was achieved in 0.1 M KNO₃ (pH 1.01), with η_{STH} of 0.44%.⁵²

Morales-Guio *et al.* reported the coupling of hematite photoanode and TiO₂/CH₃NH₃PbI₃ perovskite solar cell.⁴⁹ The

light was illuminated from the hematite side, and due to the deposition of an optically transparent FeNiO_x catalyst on the hematite surface, the parasitic light absorption by the catalyst was largely avoided. After connecting the integrated photoelectrodes with a Ni-Mo cathode, photocurrent density of 1.54 mA/cm^2 was achieved, corresponding to a η_{STH} of 1.9%. The tandem cell maintained 70% of the original performance after 8 hours test, which was due to filtering of the solution through encapsulating layer with time, leading to the quick dissolution of the perovskite cell.

In addition to hematite and WO_3 , the application of BiVO_4 photoanodes in tandem devices can significantly improve the efficiency due to its early turn-on potential for water oxidation. Abdi *et al.* reported a tandem cell device combining BiVO_4 photoanode and double- or single-junction amorphous Si solar cell.⁴³ The performance of BiVO_4 was optimized through a gradient W doping to enhance the band bending and deposition of Co-Pi catalyst to improve the water oxidation activity. After coupling with a double-junction amorphous solar cell, J_{ph} of 4 mA/cm^2 was achieved for unassisted solar water splitting by shining light from BiVO_4 side to the Si, correspond to a η_{STH} of 4.9%. Stable production of H_2 and O_2 was achieved for 1 hour without performance degradation in a pH 7 phosphate buffer.

Shi *et al.* reported the application of a distributed Bragg reflector (DBR) layer to improve the performance of a tandem cell device consisting of $\text{BiVO}_4/\text{WO}_3$ photoanode and DSSC (Figure 23a and 23b).⁸³ The DBR layer was placed on the back side of FTO glass for $\text{BiVO}_4/\text{WO}_3$ photoanode and served as the conductive counter electrode for the DSSC. The DBR layer consisting of multiple layers of materials with high- and low-refractive indices can reflect the short-wavelength photons ($\lambda < 500 \text{ nm}$) while being transparent for the long-wavelength photons, leading the photo recycling in the BiVO_4 photoanode. A η_{STH} of 7.1% was achieved, corresponding to a J_{ph} of 5.75 mA/cm^2 , which was 1.1 mA/cm^2 higher than the one without DBR layers.

Kim *et al.* reported "hetero-type dual photoelectrode (HDP)" as the photoanode in the tandem device.¹⁴⁸ By placing the hematite photoanode on the back of BiVO_4 photoanode along the incident light direction, better utilization of solar spectrum was achieved compared with the case with either BiVO_4 or hematite alone. The photocurrent density of the HDP achieved 7 mA/cm^2 at 1.23 V in 0.1 M KHCO_3 with pH 9.2, which was higher than BiVO_4 (5 mA/cm^2) and Fe_2O_3 (4 mA/cm^2) at the same applied potential. Combined with two series-connected crystalline Si solar cells, a η_{STH} of 7.7% was achieved.

Compared with the tandem cell device based on metal oxide photoanodes, the monolithically integrated devices based on III-V semiconductors have shown higher η_{STH} .

For example, Verlage *et al.* reported a monolithically integrated device based on the InGaP top cell ($E_{\text{g}}=1.84 \text{ eV}$) and GaAs bottom cell ($E_{\text{g}}=1.42 \text{ eV}$), which were electrically connected via tunnel junction in between.⁵⁴ The integrated photoanode was protected by an amorphous TiO_2 layer and sputtered Ni as OER catalyst. After the photoanode was connected to a Ni-Mo cathode, unassisted water splitting was achieved under one sun illumination in 1 M KOH electrolyte with J_{ph} of 8.5 mA/cm^2 ,

corresponding to a η_{STH} of 10.5%. Although the performance gradually decayed after 80 hours of operation, the device maintained $\eta_{\text{STH}} > 10\%$ for the initial 40 hours test. Furthermore, it can be integrated into a wireless device to achieve a η_{STH} of 8.6%.

Young *et al.* reported a detailed design of III-V semiconductor top cell and bottom cell in the tandem device to optimize the efficiency (Figure 23c-e).⁵⁵ In order to further improve the η_{STH} of III-V tandem device (theoretical maximum η_{STH} of 15% for GaInP/GaAs tandem with 1.8/1.4 eV band gaps), GaInP/GaInAs

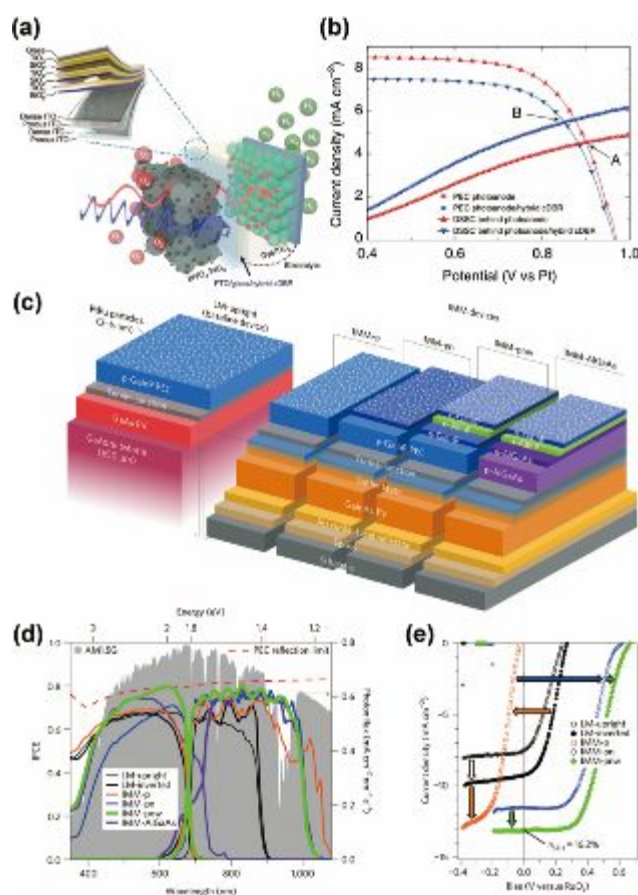


Figure 23 (a) The schematic shows the configuration of a tandem device, consisting of the $\text{BiVO}_4/\text{WO}_3$ hybrid photoanode, the DBR layer and the DSSC. (b) The J-V curves of DSSC and the hybrid photoanode in a two-electrode system with and without the DBR layers. Increased operating J_{ph} can be observed after the introduction of the DBR layer. (c) The schematic shows five tandem devices based on GaAs and GaInP. IMM: inverted metamorphic multi-junction. (d) The IPCE data of different tandem devices overlaid on the AM 1.5G reference spectrum (grey) and PEC reflection limit (red dashed line). (e) The J-V curves of different tandem devices. (a-b) reproduced from ref. 83 with permission from Springer Nature. (c-e) reproduced from ref. 55 with permission from Springer Nature.

tandem cell with 1.8/1.2 eV band gaps and AlGaAs/GaInAs tandem cell with 1.7/1.2 eV band gaps can achieve theoretical maximum η_{STH} of 24% and 21%. The long-term pursuit of an ideal device with 1.7/1.05 eV band gaps can achieve theoretical maximum η_{STH} of 27%. Based on this, the most critical challenge is to synthesize high-quality III-V semiconductors with tunable band gaps. The author used a compositionally graded buffer (CGB) layer to allow the bandgap combinations that are not constrained by the lattice constant of growth substrates. In

addition, the inverted metamorphic growth technique was applied to first grow the top cell with wider band gap, which improved the quality of top cells to provide sufficient photovoltage. Furthermore, a thin layer (25 nm) of n-GaInP was deposited on the surface of p-InGaP top cell to form buried p-n junction, enhancing the charge separation. Another thin layer (20 nm) of n-AlInP was deposited to block the hole transfer and a 10-nm n-GaInP layer was used to protect the unstable n-AlInP from the aqueous electrolyte. With PtRu as the HER catalyst, the integrated tandem cell with the thickness of effective material less than 5 μm , achieved the η_{STH} of 16.2% under AM1.5G light illumination. The limitation of this tandem cell was the long-term stability, in which 85% of initial performance was maintained after 1 hour's test.

7 Conclusion

Storing solar energy to overcome the intermittent nature of this abundant resource is of paramount importance to a future society that is primarily powered by renewable sources. PEC water splitting provides a promising route to solving this problem, but the solar hydrogen production technology, using PEC or other methods, is still far from being ready for commercialization. The critical issue lies in the development of photoelectrodes for harvesting solar energy and carrying out the desired chemical reactions efficiently and stably. Among them, thin-film photoelectrodes are unique thanks to features such as serving as a good model platform for fundamental understanding of important processes and the rich knowledge on thin-film materials. In this review, we summarized the strategies developed for thin-film materials with the purpose of overcoming challenges for efficient and inexpensive solar fuel synthesis.

A variety of synthetic methods have been applied to produce thin-film components of photoelectrodes including semiconductors, protection layers and catalysts. Those approaches can be categorized into physical vapor depositions, chemical depositions and (photo)electrochemical depositions, with corresponding advantages and caveats for each of them. How to balance the cost and material qualities would be a critical criterion to consider in choosing the suitable synthesis methods.

As the key component in thin-film photoelectrodes, the light absorbers have been explored using various semiconductors with different compositions, structures and morphologies. However, it is extremely difficult to find a single material that can meet all the needs. Common issues that limit the performance of a given material include light absorption, bulk/surface recombination, mismatch of energetics, instabilities and other issues such as fabrication cost. Representative strategies to address those issues on prototypical materials are summarized. (1) To address the light absorption problems, two common strategies are usually applied, either to narrow down the band gaps by tuning the compositions, or to reduce the optical loss due to reflection. (2) To reduce the bulk recombination, nanostructuring is usually applied to overcome the short diffusion lengths, and doping is

applied to decrease the minority carrier concentrations and improve the transport of the majority carriers. (3) The charge recombination on the surface can be addressed by depositing passivation layers or change the crystal structures at the surface. (4) To deal with the mismatch of energetics, buried junctions can be constructed or the band edge positions can be tuned, resulting larger photovoltage extractions. (5) The instability issue need to be considered from its origins, including the accumulation of by-products, the deactivation due to loss of photovoltages and corrosions. Different protection strategies corresponding to the origin of instabilities need to be applied. Among them, the deposition thin-film protection layers is the most widely used one, divided into physical barrier protection layers and kinetic protection layers.

Thin-film catalysts have been widely used to improve the performance of photoelectrodes. For better design and development of catalysts, a better understanding on their roles is critical but still missing. From a fundamental perspective, the catalysts should help to enhance the performance by either reducing the kinetic overpotentials or tuning the surface energetics at the semiconductor/electrolyte interfaces or both. A number of techniques have been developed that can be used to discern the various roles, including transient absorption spectroscopy (TAS), photoelectrochemical impedance spectroscopy (PEIS), intensity modulated photocurrent spectroscopy (IMPS), dual-working-electrode (DWE) technique and potential-sensing electrochemical atomic force microscopy (PS-EC-AFM). In addition, to deal with the effect of catalysts on light absorption, two common strategies have been applied: (1) decoupling reaction sites and light absorption sites; (2) synthesis of transparent catalysts.

The applications of thin-film photoelectrodes have been divided into two aspects. On the one hand, they can serve as study platforms for fundamental properties of semiconductors and chemical reactions. To this end, thin-film hematite photoanodes are a good example for the understanding of water oxidation mechanisms. On the other hand, prototypes of unassisted water splitting devices have been constructed based on thin-film photoelectrodes of different materials with promising solar-to-hydrogen efficiencies.

We envision that further development of research on solar fuel synthesis will continue to demand and benefit from detailed understanding of the photoelectrode materials. New device engineering on using PEC for practical solar fuel synthesis will likely be needed, as well. Both aspects will require studies on model material systems that are thin-films in form factors. Such efforts will progress hand in hand with efforts aimed at understanding the catalysis, as well as new concepts of creative light utilization. Together, these efforts will see a convergence, where practical solutions to the grand challenge of artificial photosynthesis become possible.

Conflicts of interest

There are no conflicts to declare.

Acknowledgements

We acknowledge financial support by NSF (CBET 1703662, CBET 1703655), and MassCEC (to Y.H. and D.W.), DOE (DE-E0008086) (to Y.H., D.W. and T.H.), and NSF (CHE-1664823) (to T.H.).

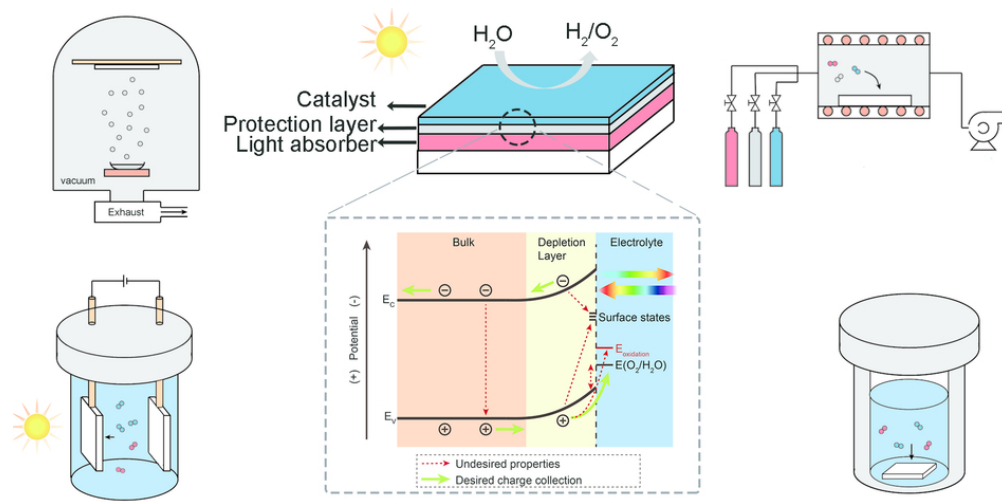
Notes and references

- S. C. Warren and E. Thimsen, *Energy Environ. Sci.*, 2012, **5**, 5133-5146.
- P. Zhang, T. Wang and J. Gong, *Adv. Mater.*, 2015, **27**, 5328-5342.
- X. Li, J. Zhu and B. Wei, *Chem. Soc. Rev.*, 2016, **45**, 3145-3187.
- S. Hu, N. S. Lewis, J. W. Ager, J. Yang, J. R. McKone and N. C. Strandwitz, *J. Phys. Chem. C*, 2015, **119**, 24201-24228.
- D. Bae, B. Seger, P. C. K. Vesborg, O. Hansen and I. Chorkendorff, *Chem. Soc. Rev.*, 2017, **46**, 1933-1954.
- M. G. Mali, H. Yoon, B. N. Joshi, H. Park, S. S. Al-Deyab, D. C. Lim, S. Ahn, C. Nervi and S. S. Yoon, *ACS Appl. Mater. Interfaces*, 2015, **7**, 21619-21625.
- H. Kumagai, T. Minegishi, N. Sato, T. Yamada, J. Kubota and K. Domen, *J. Mater. Chem. A*, 2015, **3**, 8300-8307.
- M. Zhong, T. Hisatomi, Y. Sasaki, S. Suzuki, K. Teshima, M. Nakabayashi, N. Shibata, H. Nishiyama, M. Katayama, T. Yamada and K. Domen, *Angew. Chem. Int. Ed.*, 2017, **56**, 4739-4743.
- B. AlOtaibi, H. P. T. Nguyen, S. Zhao, M. G. Kibria, S. Fan and Z. Mi, *Nano Lett.*, 2013, **13**, 4356-4361.
- D. Bae, T. Pedersen, B. Seger, B. Iandolo, O. Hansen, P. C. K. Vesborg and I. Chorkendorff, *Catal. Today*, 2017, **290**, 59-64.
- D. Kang, J. L. Young, H. Lim, W. E. Klein, H. Chen, Y. Xi, B. Gai, T. G. Deutsch and J. Yoon, *Nat. Energy*, 2017, **2**, 17043.
- H.-P. Wang, K. Sun, S. Y. Noh, A. Kargar, M.-L. Tsai, M.-Y. Huang, D. Wang and J.-H. He, *Nano Lett.*, 2015, **15**, 2817-2824.
- A. Kay, I. Cesar and M. Grätzel, *J. Am. Chem. Soc.*, 2006, **128**, 15714-15721.
- J. Yoon, S. Jo, I. S. Chun, I. Jung, H.-S. Kim, M. Meitl, E. Menard, X. Li, J. J. Coleman, U. Paik and J. A. Rogers, *Nature*, 2010, **465**, 329-333.
- D. Kang, S. Arab, S. B. Cronin, X. Li, J. A. Rogers and J. Yoon, *Appl. Phys. Lett.*, 2013, **102**, 253902.
- Y. Lin, C. Battaglia, M. Boccard, M. Hettick, Z. Yu, C. Ballif, J. W. Ager and A. Javey, *Nano Lett.*, 2013, **13**, 5615-5618.
- Y. Lin, S. Zhou, S. W. Sheehan and D. Wang, *J. Am. Chem. Soc.*, 2011, **133**, 2398-2401.
- M. T. Mayer, C. Du and D. Wang, *J. Am. Chem. Soc.*, 2012, **134**, 12406-12409.
- P. Dai, W. Li, J. Xie, Y. He, J. Thorne, G. McMahon, J. Zhan and D. Wang, *Angew. Chem. Int. Ed.*, 2014, **53**, 13493-13497.
- M. T. McDowell, M. F. Lichtenman, J. M. Spurgeon, S. Hu, I. D. Sharp, B. S. Brunschwig and N. S. Lewis, *J. Phys. Chem. C*, 2014, **118**, 19618-19624.
- M. Zhong, T. Hisatomi, Y. Kuang, J. Zhao, M. Liu, A. Iwase, Q. Jia, H. Nishiyama, T. Minegishi, M. Nakabayashi, N. Shibata, R. Niishiro, C. Katayama, H. Shibano, M. Katayama, A. Kudo, T. Yamada and K. Domen, *J. Am. Chem. Soc.*, 2015, **137**, 5053-5060.
- J.-W. Jang, C. Du, Y. Ye, Y. Lin, X. Yao, J. Thorne, E. Liu, G. McMahon, J. Zhu, A. Javey, J. Guo and D. Wang, *Nat. Commun.*, 2015, **6**, 7447.
- M. Ma, K. Zhang, P. Li, M. S. Jung, M. J. Jeong and J. H. Park, *Angew. Chem. Int. Ed.*, 2016, **55**, 11819-11823.
- W. Yang, Y. Oh, J. Kim, M. J. Jeong, J. H. Park and J. Moon, *ACS Energy Lett.*, 2016, **1**, 1127-1136.
- G. Liu, J. Shi, F. Zhang, Z. Chen, J. Han, C. Ding, S. Chen, Z. Wang, H. Han and C. Li, *Angew. Chem. Int. Ed.*, 2014, **53**, 7295-7299.
- L. Wang, F. Dionigi, N. T. Nguyen, R. Kirchgeorg, M. Gliuch, S. Grigorescu, P. Strasser and P. Schmuki, *Chem. Mater.*, 2015, **27**, 2360-2366.
- L. Cai, J. Zhao, H. Li, J. Park, I. S. Cho, H. S. Han and X. Zheng, *ACS Energy Lett.*, 2016, **1**, 624-632.
- D. Kang, T. W. Kim, S. R. Kubota, A. C. Cardiel, H. G. Cha and K.-S. Choi, *Chem. Rev.*, 2015, **115**, 12839-12887.
- I. A. Digdaya, P. P. Rodriguez, M. Ma, G. W. P. Adhyaksa, E. C. Garnett, A. H. M. Smets and W. A. Smith, *J. Mater. Chem. A*, 2016, **4**, 6842-6852.
- L. Pan, J. H. Kim, M. T. Mayer, M.-K. Son, A. Ummadisingu, J. S. Lee, A. Hagfeldt, J. Luo and M. Grätzel, *Nat. Catal.*, 2018, **1**, 412-420.
- W. Liu, H. Liu, L. Dang, H. Zhang, X. Wu, B. Yang, Z. Li, X. Zhang, L. Lei and S. Jin, *Adv. Funct. Mater.*, 2017, **27**.
- T. W. Kim and K.-S. Choi, *Science*, 2014, **343**, 990-994.
- T. Hisatomi, J. Kubota and K. Domen, *Chem. Soc. Rev.*, 2014, **43**, 7520-7535.
- A. Kudo and Y. Miseki, *Chem. Soc. Rev.*, 2009, **38**, 253-278.
- X. Chen, S. Shen, L. Guo and S. S. Mao, *Chem. Rev.*, 2010, **110**, 6503-6570.
- J. R. Bolton, S. J. Strickler and J. S. Connolly, *Nature*, 1985, **316**, 495-500.
- X. Chen, L. Liu and F. Huang, *Chem. Soc. Rev.*, 2015, **44**, 1861-1885.
- C. Yang, Z. Wang, T. Lin, H. Yin, X. Lü, D. Wan, T. Xu, C. Zheng, J. Lin, F. Huang, X. Xie and M. Jiang, *J. Am. Chem. Soc.*, 2013, **135**, 17831-17838.
- D. K. Lee and K.-S. Choi, *Nat. Energy*, 2018, **3**, 53-60.
- Y. Qiu, W. Liu, W. Chen, W. Chen, G. Zhou, P.-C. Hsu, R. Zhang, Z. Liang, S. Fan, Y. Zhang and Y. Cui, *Sci. Adv.*, 2016, **2**, e1501764.
- Y. Kuang, Q. Jia, G. Ma, T. Hisatomi, T. Minegishi, H. Nishiyama, M. Nakabayashi, N. Shibata, T. Yamada, A. Kudo and K. Domen, *Nat. Energy*, 2016, **2**, 16191.
- S. P. Berglund, A. J. E. Rettie, S. Hoang and C. B. Mullins, *Phys. Chem. Chem. Phys.*, 2012, **14**, 7065-7075.
- F. F. Abdi, L. Han, A. H. M. Smets, M. Zeman, B. Dam and R. van de Krol, *Nat. Commun.*, 2013, **4**, 2195.
- J. Luo, L. Steier, M.-K. Son, M. Schreier, M. T. Mayer and M. Grätzel, *Nano Lett.*, 2016, **16**, 1848-1857.
- C. Li, T. Hisatomi, O. Watanabe, M. Nakabayashi, N. Shibata, K. Domen and J.-J. Delaunay, *Energy Environ. Sci.*, 2015, **8**, 1493-1500.
- A. Paracchino, V. Laporte, K. Sivula, M. Grätzel and E. Thimsen, *Nat. Mater.*, 2011, **10**, 456-461.
- Y. F. Tay, H. Kaneko, S. Y. Chiam, S. Lie, Q. Zheng, B. Wu, S. S. Hadke, Z. Su, P. S. Bassi, D. Bishop, T. C. Sum, T. Minegishi, J. Barber, K. Domen and L. H. Wong, *Joule*, 2018, **2**, 537-548.
- M. Li, J. Deng, A. Pu, P. Zhang, H. Zhang, J. Gao, Y. Hao, J. Zhong and X. Sun, *J. Mater. Chem. A*, 2014, **2**, 6727-6733.

49. C. G. Morales-Guio, M. T. Mayer, A. Yella, S. D. Tilley, M. Grätzel and X. Hu, *J. Am. Chem. Soc.*, 2015, **137**, 9927-9936.
50. T. H. Jeon, G.-h. Moon, H. Park and W. Choi, *Nano Energy*, 2017, **39**, 211-218.
51. J. Y. Kim, G. Magesh, D. H. Youn, J.-W. Jang, J. Kubota, K. Domen and J. S. Lee, *Sci. Rep.*, 2013, **3**, 2681.
52. W. Li, S. W. Sheehan, D. He, Y. He, X. Yao, R. L. Grimm, G. W. Brudvig and D. Wang, *Angew. Chem. Int. Ed.*, 2015, **54**, 11428-11432.
53. Y. Zhao, K. R. Yang, Z. Wang, X. Yan, S. Cao, Y. Ye, Q. Dong, X. Zhang, J. E. Thorne, L. Jin, K. L. Materna, A. Trimpalis, H. Bai, S. C. Fakra, X. Zhong, P. Wang, X. Pan, J. Guo, M. Flytzani-Stephanopoulos, G. W. Brudvig, V. S. Batista and D. Wang, *Proc. Natl. Acad. Sci. U.S.A.*, 2018, **115**, 2902-2907.
54. E. Verlage, S. Hu, R. Liu, R. J. R. Jones, K. Sun, C. Xiang, N. S. Lewis and H. A. Atwater, *Energy Environ. Sci.*, 2015, **8**, 3166-3172.
55. J. L. Young, M. A. Steiner, H. Döscher, R. M. France, J. A. Turner and Todd G. Deutsch, *Nat. Energy*, 2017, **2**, 17028.
56. J. Gu, Y. Yan, J. L. Young, K. X. Steirer, N. R. Neale and J. A. Turner, *Nat. Mater.*, 2016, **15**, 456-460.
57. J. Gu, J. A. Aguiar, S. Ferrere, K. X. Steirer, Y. Yan, C. Xiao, James L. Young, M. Al-Jassim, N. R. Neale and J. A. Turner, *Nat. Energy*, 2017, **2**, 16192.
58. J. Kamimura, P. Bogdanoff, F. Abdi, J. Lähnemann, R. van de Krol, H. Riechert and L. Geelhaar, *J. Phys. Chem. C*, 2017.
59. Y. J. Hwang, A. Boukai and P. Yang, *Nano Lett.*, 2008, **9**, 410-415.
60. I. Narkeviciute, P. Chakhranont, A. J. M. Mackus, C. Hahn, B. A. Pinaud, S. F. Bent and T. F. Jaramillo, *Nano Lett.*, 2016, **16**, 7565-7572.
61. S. Fan, B. AlOtaibi, S. Y. Woo, Y. Wang, G. A. Botton and Z. Mi, *Nano Lett.*, 2015, **15**, 2721-2726.
62. W. Qin, N. Wang, T. Yao, S. Wang, H. Wang, Y. Cao, S. Liu and C. Li, *ChemSusChem*, 2015, **8**, 3987-3991.
63. I. A. Digdaya, L. Han, T. W. F. Buijs, M. Zeman, B. Dam, A. H. M. Smets and W. A. Smith, *Energy Environ. Sci.*, 2015, **8**, 1585-1593.
64. L. Han, I. A. Digdaya, T. W. F. Buijs, F. F. Abdi, Z. Huang, R. Liu, B. Dam, M. Zeman, W. A. Smith and A. H. M. Smets, *J. Mater. Chem. A*, 2015, **3**, 4155-4162.
65. H. Hajibabaei, O. Zandi and T. W. Hamann, *Chem. Sci.*, 2016, **7**, 6760-6767.
66. Y. Li, L. Zhang, A. Torres-Pardo, J. M. González-Calbet, Y. Ma, P. Oleynikov, O. Terasaki, S. Asahina, M. Shima, D. Cha, L. Zhao, K. Takanabe, J. Kubota and K. Domen, *Nat. Commun.*, 2013, **4**, 2566.
67. J. Seo, T. Takata, M. Nakabayashi, T. Hisatomi, N. Shibata, T. Minegishi and K. Domen, *J. Am. Chem. Soc.*, 2015, **137**, 12780-12783.
68. G. Liu, S. Ye, P. Yan, F.-Q. Xiong, P. Fu, Z. Wang, Z. Chen, J. Shi and C. Li, *Energy Environ. Sci.*, 2016, **9**, 1327-1334.
69. Y. He, J. E. Thorne, C. H. Wu, P. Ma, C. Du, Q. Dong, J. Guo and D. Wang, *Chem*, 2016, **1**, 640-655.
70. Y. He, P. Ma, S. Zhu, M. Liu, Q. Dong, J. Espano, X. Yao and D. Wang, *Joule*, 2017, **1**, 831-842.
71. Y. Li, R. Wang, H. Li, X. Wei, J. Feng, K. Liu, Y. Dang and A. Zhou, *J. Phys. Chem. C*, 2015, **119**, 20283-20292.
72. J. Zhang, X. Chang, C. Li, A. Li, S. Liu, T. Wang and J. Gong, *J. Mater. Chem. A*, 2018, **6**, 3350-3354.
73. R. Liu, Y. Lin, L.-Y. Chou, S. W. Sheehan, W. He, F. Zhang, H. J. M. Hou and D. Wang, *Angew. Chem. Int. Ed.*, 2011, **50**, 499-502.
74. S. Wang, H. Chen, G. Gao, T. Butburee, M. Lyu, S. Thaweesak, J.-H. Yun, A. Du, G. Liu and L. Wang, *Nano Energy*, 2016, **24**, 94-102.
75. J. A. Seabold and K.-S. Choi, *Chem. Mater.*, 2011, **23**, 1105-1112.
76. S. L. Liew, Z. Zhang, T. W. G. Goh, G. S. Subramanian, H. L. D. Seng, T. S. A. Hor, H. K. Luo and D. Z. Chi, *Int. J. Hydrogen*, 2014, **39**, 4291-4298.
77. M. G. Kibria and Z. Mi, *J. Mater. Chem. A*, 2016, **4**, 2801-2820.
78. A. Theuwis, K. Strubbe, L. M. Depestel and W. P. Gomes, *J. Electrochem. Soc.*, 2002, **149**, E173-E178.
79. M. G. Kibria, R. Qiao, W. Yang, I. Boukahil, X. Kong, F. A. Chowdhury, M. L. Trudeau, W. Ji, H. Guo, F. J. Himpel, L. Vayssieres and Z. Mi, *Adv. Mater.*, 2016, **28**, 8388-8397.
80. E. Garnett and P. Yang, *Nano Lett.*, 2010, **10**, 1082-1087.
81. J. R. Maiolo, B. M. Kayes, M. A. Filler, M. C. Putnam, M. D. Kelzenberg, H. A. Atwater and N. S. Lewis, *J. Am. Chem. Soc.*, 2007, **129**, 12346-12347.
82. P. Dai, J. Xie, M. T. Mayer, X. Yang, J. Zhan and D. Wang, *Angew. Chem. Int. Ed.*, 2013, **52**, 11119-11123.
83. X. Shi, H. Jeong, S. J. Oh, M. Ma, K. Zhang, J. Kwon, I. T. Choi, I. Y. Choi, H. K. Kim, J. K. Kim and J. H. Park, *Nat. Commun.*, 2016, **7**, 11943.
84. I. Cesar, K. Sivula, A. Kay, R. Zboril and M. Grätzel, *J. Phys. Chem. C*, 2009, **113**, 772-782.
85. J. H. Kennedy and K. W. Frese, *J. Electrochem. Soc.*, 1978, **125**, 709-714.
86. P. E. de Jongh, D. Vanmaekelbergh and J. J. Kelly, *Chem. Mater.*, 1999, **11**, 3512-3517.
87. C. J. Engel, T. A. Polson, J. R. Spado, J. M. Bell and A. Fillinger, *J. Electrochem. Soc.*, 2008, **155**, F37-F42.
88. Y. Li, T. Takata, D. Cha, K. Takanabe, T. Minegishi, J. Kubota and K. Domen, *Adv. Mater.*, 2013, **25**, 125-131.
89. A. Ziani, E. Nurlaela, D. S. Dhawale, D. A. Silva, E. Alarousu, O. F. Mohammed and K. Takanabe, *Phys. Chem. Chem. Phys.*, 2015, **17**, 2670-2677.
90. M. de Respini, M. Fravventura, F. F. Abdi, H. Schreuders, T. J. Savenije, W. A. Smith, B. Dam and R. van de Krol, *Chem. Mater.*, 2015, **27**, 7091-7099.
91. W. Li, P. Da, Y. Zhang, Y. Wang, X. Lin, X. Gong and G. Zheng, *ACS Nano*, 2014, **8**, 11770-11777.
92. H. Dotan, K. Sivula, M. Grätzel, A. Rothschild and S. C. Warren, *Energy Environ. Sci.*, 2011, **4**, 958-964.
93. D. K. Zhong, S. Choi and D. R. Gamelin, *J. Am. Chem. Soc.*, 2011, **133**, 18370-18377.
94. Y. Gao and T. W. Hamann, *Chem. Commun.*, 2017, **53**, 1285-1288.
95. T. Hisatomi, J. Brilliet, M. Cornuz, F. Le Formal, N. Tetreault, K. Sivula and M. Grätzel, *Faraday Discussions*, 2012, **155**, 223-232.
96. M. Grätzel, *Nature*, 2001, **414**, 338-344.
97. S. Hu, M. R. Shaner, J. A. Beardslee, M. Lichterman, B. S. Brunschwig and N. S. Lewis, *Science*, 2014, **344**, 1005-1009.
98. M. J. Kenney, M. Gong, Y. Li, J. Z. Wu, J. Feng, M. Lanza and H. Dai, *Science*, 2013, **342**, 836-840.
99. J. Augustynski, R. Solarzka, H. Hagemann and C. Santato, *Proc. SPIE*, 2006, **6340**, 63400J.

100. R. S. Lillard, G. S. Kanner and D. P. Butt, *J. Electrochem. Soc.*, 1998, **145**, 2718-2725.
101. F. M. Toma, J. K. Cooper, V. Kunzelmann, M. T. McDowell, J. Yu, D. M. Larson, N. J. Borys, C. Abelyan, J. W. Beeman, K. M. Yu, J. Yang, L. Chen, M. R. Shaner, J. Spurgeon, F. A. Houle, K. A. Persson and I. D. Sharp, *Nat. Commun.*, 2016, **7**, 12012.
102. G. Liu, P. Fu, L. Zhou, P. Yan, C. Ding, J. Shi and C. Li, *Chem. Eur. J.*, 2015, **21**, 9624-9628.
103. J. E. Thorne, Y. Zhao, D. He, S. Fan, S. Vanka, Z. Mi and D. Wang, *Phys. Chem. Chem. Phys.*, 2017, **19**, 29653-29659.
104. R. J. Britto, J. D. Benck, J. L. Young, C. Hahn, T. G. Deutsch and T. F. Jaramillo, *J. Phys. Chem. Lett.*, 2016, **7**, 2044-2049.
105. A. L. Greenaway, J. W. Boucher, S. Z. Oener, C. J. Funch and S. W. Boettcher, *ACS Energy Lett.*, 2017, **2**, 2270-2282.
106. J. S. Ward, T. Remo, K. Horowitz, M. Woodhouse, B. Sopori, K. VanSant and P. Basore, *Prog. Photovolt. Res. Appl.*, 2016, **24**, 1284-1292.
107. F. L. Formal, M. Grätzel and K. Sivula, *Adv. Funct. Mater.*, 2010, **20**, 1099-1107.
108. O. Zandi, B. M. Klahr and T. W. Hamann, *Energy Environ. Sci.*, 2013, **6**, 634-642.
109. Y.-H. Lai, H. S. Park, J. Z. Zhang, P. D. Matthews, D. S. Wright and E. Reisner, *Chem. Eur. J.*, 2015, **21**, 3919-3923.
110. R. C. Kainthla, B. Zelenay and J. O. M. Bockris, *J. Electrochem. Soc.*, 1986, **133**, 248-253.
111. D. Bae, T. Pedersen, B. Seger, M. Malizia, A. Kuznetsov, O. Hansen, I. Chorkendorff and P. C. K. Vesborg, *Energy Environ. Sci.*, 2015, **8**, 650-660.
112. H. Yu, S. Chen, X. Fan, X. Quan, H. Zhao, X. Li and Y. Zhang, *Angew. Chem. Int. Ed.*, 2010, **49**, 5106-5109.
113. Z. Zhang, R. Dua, L. Zhang, H. Zhu, H. Zhang and P. Wang, *ACS Nano*, 2013, **7**, 1709-1717.
114. W. Li, D. He, S. W. Sheehan, Y. He, J. E. Thorne, X. Yao, G. W. Brudvig and D. Wang, *Energy Environ. Sci.*, 2016, **9**, 1794-1802.
115. Y. Zhao, X. Yan, K. R. Yang, S. Cao, Q. Dong, J. E. Thorne, K. L. Materna, S. Zhu, X. Pan, M. Flytzani-Stephanopoulos, G. W. Brudvig, V. S. Batista and D. Wang, *ACS Cent. Sci.*, 2018, **4**, 1166-1172.
116. C. Du, X. Yang, M. T. Mayer, H. Hoyt, J. Xie, G. McMahon, G. Bischooping and D. Wang, *Angew. Chem. Int. Ed.*, 2013, **52**, 12692-12695.
117. J. E. Thorne, S. Li, C. Du, G. Qin and D. Wang, *J. Phys. Chem. Lett.*, 2015, **6**, 4083-4088.
118. M. Barroso, A. J. Cowan, S. R. Pendlebury, M. Grätzel, D. R. Klug and J. R. Durrant, *J. Am. Chem. Soc.*, 2011, **133**, 14868-14871.
119. M. Barroso, C. A. Mesa, S. R. Pendlebury, A. J. Cowan, T. Hisatomi, K. Sivula, M. Grätzel, D. R. Klug and J. R. Durrant, *Proc. Natl. Acad. Sci. U.S.A.*, 2012, **109**, 15640-15645.
120. B. Klahr, S. Gimenez, F. Fabregat-Santiago, J. Bisquert and T. W. Hamann, *J. Am. Chem. Soc.*, 2012, **134**, 16693-16700.
121. S. C. Riha, B. M. Klahr, E. C. Tyo, S. Seifert, S. Vajda, M. J. Pellin, T. W. Hamann and A. B. F. Martinson, *ACS Nano*, 2013, **7**, 2396-2405.
122. G. M. Carroll and D. R. Gamelin, *J. Mater. Chem. A*, 2016, **4**, 2986-2994.
123. J. E. Thorne, J.-W. Jang, E. Y. Liu and D. Wang, *Chem. Sci.*, 2016, **7**, 3347-3354.
124. C. Zachaus, F. F. Abdi, L. M. Peter and R. van de Krol, *Chem. Sci.*, 2017, **8**, 3712-3719.
125. F. Lin and S. W. Boettcher, *Nat. Mater.*, 2014, **13**, 81-86.
126. M. R. Nellist, F. A. L. Laskowski, F. Lin, T. J. Mills and S. W. Boettcher, *Acc. Chem. Res.*, 2016, **49**, 733-740.
127. J. Qiu, H. Hajibabaei, M. R. Nellist, F. A. L. Laskowski, T. W. Hamann and S. W. Boettcher, *ACS Cent. Sci.*, 2017, **3**, 1015-1025.
128. J. Qiu, H. Hajibabaei, M. R. Nellist, F. A. L. Laskowski, S. Z. Oener, T. W. Hamann and S. W. Boettcher, *ACS Energy Lett.*, 2018, **3**, 961-969.
129. M. R. Nellist, F. A. L. Laskowski, J. Qiu, H. Hajibabaei, K. Sivula, T. W. Hamann and S. W. Boettcher, *Nat. Energy*, 2018, **3**, 46-52.
130. L. Bertoluzzi and J. Bisquert, *J. Phys. Chem. Lett.*, 2012, **3**, 2517-2522.
131. B. Klahr, S. Gimenez, F. Fabregat-Santiago, J. Bisquert and T. W. Hamann, *Energy Environ. Sci.*, 2012, **5**, 7626-7636.
132. B. Klahr, S. Gimenez, F. Fabregat-Santiago, T. Hamann and J. Bisquert, *J. Am. Chem. Soc.*, 2012, **134**, 4294-4302.
133. J. Bisquert, L. Bertoluzzi, I. Mora-Sero and G. Garcia-Belmonte, *J. Phys. Chem. C*, 2014, **118**, 18983-18991.
134. L. M. Peter, *Chem. Rev.*, 1990, **90**, 753-769.
135. E. A. Ponomarev and L. M. Peter, *J. Electroanal. Chem.*, 1995, **396**, 219-226.
136. E. A. Ponomarev and L. M. Peter, *J. Electroanal. Chem.*, 1995, **397**, 45-52.
137. L. M. Peter, E. A. Ponomarev and D. J. Fermín, *J. Electroanal. Chem.*, 1997, **427**, 79-96.
138. L. M. Peter, *J. Phys. Chem. C*, 2007, **111**, 6601-6612.
139. M. R. Shaner, J. R. McKone, H. B. Gray and N. S. Lewis, *Energy Environ. Sci.*, 2015, **8**, 2977-2984.
140. W. Vijeelaar, P. Westerik, J. Veerbeek, R. M. Tiggelaar, E. Berenschot, N. R. Tas, H. Gardeniers and J. Huskens, *Nat. Energy*, 2018, **3**, 185-192.
141. I. Roger, R. Moca, H. N. Miras, K. G. Crawford, D. A. J. Moran, A. Y. Ganin and M. D. Symes, *J. Mater. Chem. A*, 2017, **5**, 1472-1480.
142. Q. Ding, J. Zhai, M. Cabán - Acevedo, M. J. Shearer, L. Li, H. C. Chang, M. L. Tsai, D. Ma, X. Zhang, R. J. Hamers, J. H. He and S. Jin, *Adv. Mater.*, 2015, **27**, 6511-6518.
143. F. Le Formal, E. Pastor, S. D. Tilley, C. A. Mesa, S. R. Pendlebury, M. Grätzel and J. R. Durrant, *J. Am. Chem. Soc.*, 2015, **137**, 6629-6637.
144. Y. Zhang, H. Zhang, H. Ji, W. Ma, C. Chen and J. Zhao, *J. Am. Chem. Soc.*, 2016, **138**, 2705-2711.
145. O. Zandi and T. W. Hamann, *Nat. Chem.*, 2016, **8**, 778-783.
146. Y. Zhang, H. Zhang, A. Liu, C. Chen, W. Song and J. Zhao, *J. Am. Chem. Soc.*, 2018, **140**, 3264-3269.
147. J. Brillet, J.-H. Yum, M. Cornuz, T. Hisatomi, R. Solarska, J. Augustynski, M. Graetzel and K. Sivula, *Nat. Photon.*, 2012, **6**, 824-828.
148. J. H. Kim, J.-W. Jang, Y. H. Jo, F. F. Abdi, Y. H. Lee, R. van de Krol and J. S. Lee, *Nat. Commun.*, 2016, **7**, 13380.

This review provides a comprehensive overview for fabrication, development and application of thin-film photoelectrodes.



79x39mm (300 x 300 DPI)